Influence of the growth conditions on the optical properties of $SrTiO_3$

DISSERTATION

zur Erlangung des akademischen Grades
doctor rerum naturalium
(Dr. rer. nat.)

im Fach Chemie
Spezialisierung: Physikalische und theoretische Chemie

eingereicht an der
Mathematisch-Naturwissenschaftlichen Fakultät der
Humboldt-Universität zu Berlin

von

M.Sc. Dirk Johannes Kok

Präsidentin der Humboldt-Universität zu Berlin:
Prof. Dr.-Ing. Dr. Sabine Kunst

Dekan der Mathematisch-Naturwissenschaftlichen Fakultät:
Prof. Dr. Elmar Kulke

Gutachter/innen	1. Dr. habil. Detlef Klimm
	2. Professor Dr.-Ing. Matthias Bickermann
	3. Professor Dr. Nicola Pinna
Tag der mündlichen Prüfung:	31-01-2017

Abstract

Strontium titanate ($SrTiO_3$) is an important heteroepitaxy substrate material which has seen a recent rise in interest as it is an essential component in almost all oxide based two-dimensional free electron gas systems. These systems offer many potential applications, but are very sensitive to dislocations in the substrate crystals and their full potential cannot be reached with the currently commercially available material. To improve crystal quality, alternative growth methods are necessary and to find and to optimize such methods comprehensive knowledge about the temperature dependent material properties is crucial.

For many oxides, high-quality bulk crystals can be produced by application of the widely used Czochralski (Cz) method. For a successful implementation of this method, a sufficiently high heat transport through the growing crystal is highly important. Very low heat transport will lead to unstable growth, which in $SrTiO_3$ often results in spiral or foot formation. Because $SrTiO_3$ has a very high melting point of about 2350 K, radiative heat transport dominates. To understand why the heat transport is so low, IR spectra were measured from room temperature up to 1673 K in a special set up. These spectra show a broad long wavelength absorption without peaks which indicates that free charge carriers cause the low radiative heat transport. UV/VIS spectra from 4 K to 1723 K show that the band gap shifts strongly with temperature, which, together with the formation of ionized vacancies, causes the high free carrier concentration. Since the IR absorption depends strongly on the temperature, growth at lower temperatures should be easier to control. This can be achieved through the top seeded solution growth (TSSG) method. Another route to stable crystal growth is the edge-defined film-fed growth (EFG) method. It operates at very high temperatures (like for growth by the Cz method) but stabilizes the growth interface since the meniscus is pinned at the edge of the die and it allows an easier optimization of the axial and radial thermal gradient of growing crystal.

Many of the crystals produced by the growth methods investigated here show strong differences in their optical properties. Deviations from stoichiometry were also found which are in a similar range to those found for ceramics or thin layers. The dependence of the optical properties on the growth atmosphere and on growth conditions was systematically investigated for crystals grown by the TSSG and laser heated pedestal growth (LHPG) methods. In both cases, an atmosphere with a very low oxygen concentration led to blue/black conducting crystals and an atmosphere with an oxygen concentration that was too high led to brownish crystals. With the correct oxygen concentration, colorless crystals can be grown. The concentrations at which the colors change are different for the two methods, but the spectra are very similar. The brown coloration in nearly stoichiometric top seeded solution grown crystals was found to be caused by light scattering at nanometer sized voids in the crystals. These nano-voids are probably formed by the combination of oppositely charged vacancies.

Kurzzusammenfassung

Strontiumtitanat ($SrTiO_3$) ist ein wichtiges Substratmaterial für die Heteroepitaxie von funktionellen Dünnschichten. Innerhalb der letzten Jahre gab es ein sehr hohes Interesse an diesem Material, da es eine essenzielle Komponente von fast allen bekannten oxidbasierten zweidimensionalen Elektronengassystemen ist. Diese Systeme haben viele interessante Anwendungen, die Leitungsfähigkeit von Devices ist aber sehr anfällig für Versetzungen im Substrat, weswegen das volle Potential mit den kommerziell verfügbaren Kristallen nicht ausgeschöpft werden kann. Um die Kristallqualität zu erhöhen, müssen alternative Züchtungsmethoden gefunden und optimiert werden und dazu ist ein umfassendes Verständnis der temperaturabhängigen Materialeigenschaften unerlässlich.

Für viele Oxide können Volumenkristalle von hoher struktureller Qualität mit der weitverbreiteten Czochralski (Cz) Methode hergestellt werden. Eine erfolgreiche Anwendung dieser Methode erfordert einen ausreichenden Wärmetransport durch den wachsenden Kristall. Ein sehr niedriger Wärmetransport führt zu Wachstumsinstabilitäten, was sich bei $SrTiO_3$ durch Fuß- oder Spiralbildung äußert. Weil $SrTiO_3$ einen sehr hohen Schmelzpunkt von ca. 2350K hat, dominiert der Strahlungswärmetransport. Um die Ursache für den geringen Wärmetransport zu verstehen, wurden IR-Spektren zwischen 300 K und 1673 K in einem speziellen Aufbau gemessen. Diese Spektren zeigen eine breite Absorption, welche mit zunehmender Wellenlänge ansteigt und auf eine Absorption an freien Ladungsträgern hinweist. UV/VIS-Spektren von 4 K bis 1723 K zeigen, dass die Bandkantenabsorption stark temperaturabhängig ist, was zusammen mit ionisierten Defekten zu einer hohen Dichte an freien Ladungsträgern führt.

Da die IR-Absorption stark mit der Temperatur zunimmt, bietet Kristallzüchtung bei niedrigeren Temperaturen mehr Kontrolle. Dies kann mit Schmelzlösungszüchtung (top-seeded solution growth, TSSG-Methode) erreicht werden. Alternativ lässt sich stabiles Wachstum durch einen Formgeber (edge-defined film-fed growth, EFG-Methode) erreichen. Da der Meniskus durch den Rand des Formgebers fixiert werden kann, und eine Optimierung des radialen und axialen Temperaturgradienten des wachsenden Kristalls möglich ist, lässt sich diese Methode, trotz der vergleichsweise hohen Temperaturen, erfolgreich für die Züchtung von hochwertigen Kristallen aus der Schmelze einsetzen.

Kristalle die mit unterschiedlichen Züchtungsmethoden am IKZ gezüchtet wurden zeigen starke Unterschiede in ihren optischen Eigenschaften. Es wurde auch die Existenz einer Phasenbreite festgestellt, die sich mit den Literaturwerten von $SrTiO_3$-Keramiken und Dünnschichten deckt. Die Abhängigkeit der optischen und chemischen Eigenschaften von der Züchtungsatmosphäre und den Züchtungsbedingungen wurde für ausgewählte Züchtungsmethoden („top-seeded solution growth“ und „laser heated pedestal growth“) systematisch untersucht.

Bei beiden Züchtungsmethoden führt eine Atmosphäre mit sehr geringer Sauerstoffkonzentration zu einer schwarz-blauen Verfärbung und zu leitfähigen Kristallen. Eine zu hohe Sauerstoffkonzentration während der Züchtung resultiert in einer gelbbraunen Verfärbung der Kristalle. Mit dem richtigen Sauerstoffpartialdruck ist es möglich farblose Kristalle zu züchten. Die für einen Farbumschlag notwendigen Sauerstoffkonzentrationen sind für die beiden Züchtungsmethoden unterschiedlich. Die braune Verfärbung in nahezu stoichiometrischen TSSG-Kristallen konnte auf Nanometer große Hohlräume in den $SrTiO_3$-Kristallen zurückgeführt werden die zu Mie-Streuung führen. Diese Nanohohlräume entstehen wahrscheinlich durch die

Kombination von gegensätzlich geladenen Punktdefekten während des Kristallwachstums.

Contents

1. Introduction

Strontium titanate ($SrTiO_3$, STO) is a cubic perovskite that was first grown in the 1950's, mainly as a diamond imitation. The naturally occurring mineral version, tausonite, was not known until its discovery in eastern Siberia in 1982. Tausonite is a very rare mineral in nature and occurs only as tiny crystals. Stoichiometric $SrTiO_3$ crystals are colorless, with an indirect band gap of 3.2 eV and a direct band gap of 3.5 eV [1] and a high dielectric constant of 300 at room temperature [2] which rises to about 20000 at 2 K [3]. Stoichiometric crystals are insulating, but by removing oxygen from the crystals or by doping, with, for example, La or Nb, the crystals become n-type semiconductors (with low electron mobility) or even conductors. Since $SrTiO_3$ is insoluble in water and has a high melting point of 2350 K, it has been used in $^{90}_{38}$Sr radioisotope thermal generators [4].

$SrTiO_3$ is widely used as a substrate material for oxide heterostructures such as strain engineered piezoelectric and multiferroic materials [5, 6], high temperature superconductors like yttrium barium copper oxides [7] and two dimensional free electron gases (2DEGs). Oxide based 2DEGs have been observed at the interface between $SrTiO_3$ and various other insulating complex oxides like $LaAlO_3$, $LaVO_3$, $LaGaO_3$ or $GdTiO_3$ [8–15]. Such 2DEG-based devices show carrier mobilities up to 10^5 $cm^2V^{-1}s^{-1}$ [11]. Not only is the $LaAlO_3/SrTiO_3$ interface highly conductive, it also shows emergent properties such as ferromagnetism and superconductivity [16–21]. There are many interesting apllications possible with oxide based 2DEGs, but there is a problem that prevent these systems from reaching their full potential: the interface conductivity can be easily disturbed, for example by edge dislocations which destroy conductivity in a 5 nm radius around them [22]. This is problematic, since the commercially available STO substrates have rather high etch pit densities of $\approx 10^6$ cm^{-2} and almost all oxide based 2DEG systems use $SrTiO_3$ crystals as substrates (a few exceptions including $YTiO_3$ on $CaTiO_3$ [23] and $LaTiO_3$ on $KTaO_3$ [24] have been reported). Attempts have been made to use epitaxial layers of $SrTiO_3$, but the properties of the interfaces were not as good as on STO single crystals [25, 26].

Commercially available $SrTiO_3$ crystals are grown by the Verneuil (flame fusion) method (see section 2.3.1) in which a feed powder is passed into an H_2/O_2 flame, where it melts. The droplets fall onto a translating rod and crystallize. This involves very high temperature gradients and so the quality of the crystals is not very high nor expected to improve. Other growth methods like skull melting (cold crucible), hydrothermal, optical floating zone or flux growth have been tested [27, 28], but so far either the crystal quality or the crystal size was insufficient to provide high quality wafers. That is why this project was launched to investigate possible growth methods, understand the source of the difficulties in the crystal growth of $SrTiO_3$ and investigate the properties of the crystals produced.

1.1. Outline of this work

The purpose of this thesis project was to characterize the crystals grown in the project and to understand the source of the difficulties in the crystal growth. The crystals investigated here were mostly grown by Christo Guguschev (top-seeded solution growth, Czochralski and edge-defined film-fed growth), Zbigniew Galazka (Czochralski growth) and Franz Kamutzki

(Laser heated pedestal growth). Since the work presented here is experimental in nature, the theory and background information given in chapter 2 is kept concise. It should provide enough background information to understand the experimental work presented but for more detailed information references to the literature are provided.

To better understand the improvements to the methods required, high and low temperature spectroscopy were used to study the radiative heat transport through the material. These investigations revealed that heat transport through STO is very low at high temperatures, but is also strongly dependent on temperature. This shows that methods like top-seeded solution growth, which operate at a lower temperature, should allow more controllable growth with lower temperature gradients, leading to higher quality crystals. The high infrared absorption at high temperatures is caused by free carrier absorption so an attempt was made to increase the radiative heat transport by doping to compensate for the formation of oxygen vacancies.

Many crystals grown in this project showed colorations which were not well explained in the literature so far. The optical properties of the material depend on the oxygen concentration of the growth atmosphere, and this dependence was systematically studied. The crystals with blue and brown colorations were investigated with temperature dependent spectroscopy combined with high resolution transmission electron microscopy investigations performed by Toni Markurt, Muton Niu and Robert Schewski. Explanations for blue and brown colorations are proposed.

2. Background and state of the art

2.1. $SrTiO_3$

Strontium titanate ($SrTiO_3$, STO) is a cubic perovskite with a large indirect band gap of 3.2 eV at room temperature [1]. The structure is shown in figure 2.1.1. Ti^{4+} and O^{2-} form octahedra with Sr^{2+} in the octahedral voids. Some properties are listed in table 2.1.1. STO was first synthesized in the 1950's and used as a diamond simulant since it has a high refractive index of 2.3-2.6 in the visible range. However, it was replaced in this role by cubic Zirconia since the refractive index of that material is closer to diamond and its hardness is higher as well (STO only has a Mohs hardness of 6-6.5).

Later, STO was used as an epitaxy substrate, for example for the high temperature superconductor yttrium barium copper oxide, which is sometimes used in superconducting quantum interference devices (SQUIDs) which are very sensitive magnetometers [36]. STO has a phase transition to an orthorombic phase at 105±5 K [37], caused by a slight rotation of the oxygen octahedra. At high temperatures, no phase transition is observed below the melting point of 2350 K.

2.2. Growth instabilities and spiral formation

Some high melting oxides show the tendency to grow in a spiral shape during Czochralski growth (see section 2.3.2) [38]. This is unwanted, since much less of the material is usable. Naumowicz et al. showed through X-ray topography that the spiral formation in gadolinium gallium garnet ($Gd_3Ga_5O_{12}$) was not caused by an anomaly in the crystal growth mechanism [39]. According to Schwabe et al., there are several conditions that can make a system unstable so the spiral growth can be triggered [40]:

- A high melting point so radiative heat transport dominates over conductive heat transport
- Small radial temperature gradient in the melt near the meniscus
- Low optical transmission through the crystal, either caused by impurities or the intrinsic properties of the crystal itself. The absorption around the maximum black body emission is the most important as it hinders the axial heat transport and increases the heat radiation absorbed from the crucible sides. Most heat is radiated sideways from the meniscus and not through the crystal if this is the case
- A non-convex growth interface
- A weight controlled process. The weight control cannot distinguish between a cylindrical crystal and a spiral, but is required to keep a regular increase in crystal weight which is needed to grow a regularly shaped spiral

These conditions do not mean that a spiral will necessarily form. To start spiral growth, the shape of the meniscus has to lose symmetry. When this happens, one side of the meniscus

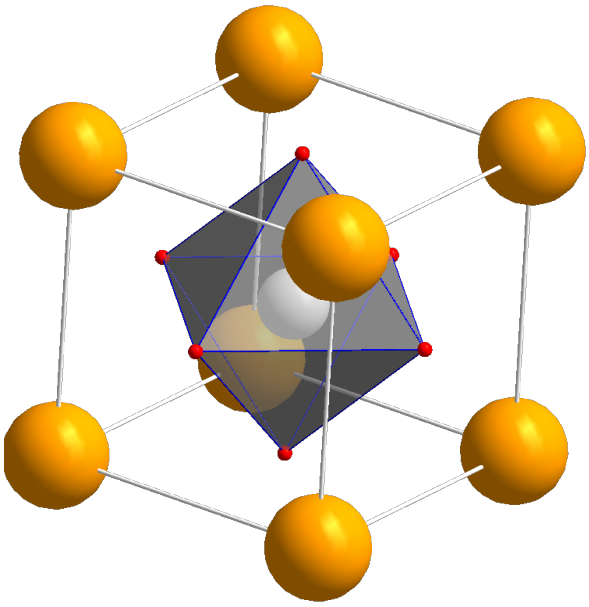

Figure 2.1.1.: Structure of $SrTiO_3$. Orange: Sr^{2+}, White: Ti^{4+} and red O^{2-}.

Table 2.1.1.: Some room temperature properties of $SrTiO_3$.

Property	**Value**	**Reference**
Formula	$SrTiO_3$	
Symmetry	Cubic	
Space group	$Pm\bar{3}m$	[29]
Lattice constant	3.905268 Å	[29]
Density	5.12 g/cm^{-3}	[30]
Melting point	2350 K	[31]
Dielectric constant	300	[32]
Thermal conductivity	12 $Wm^{-1}K^{-1}$	[33]
Coefficient of thermal expansion	5.89 K^{-1}	[30]
Mohs hardness	6-6.5	[34]
Refractive index (at 500 nm)	2.6	[35]
Band gap (indirect)	3.2 eV	[1]
Band gap (direct)	3.7 eV	[1]

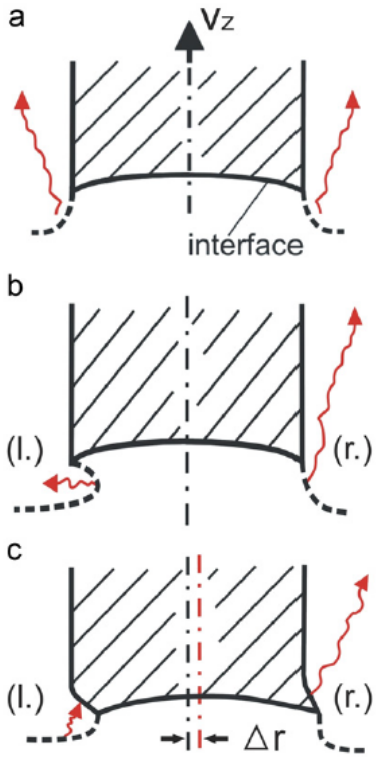

Figure 2.2.1.: Three stages of the beginning spiral formation. (a) Relatively large radiative cooling of the crystal periphery results in an interface which is concave towards the melt and difficult radius control. (b) A small disturbance of the symmetry leads to a "partial necking in" on the left side (l.). This results in loss of weight increase which is compensated by the control unit by power reduction to increase the weight increase again. Because of the necking-in on side (l.) the meniscus and the crystal at (l.) are less cooled than elsewhere and the crystal does not grow here (l.) but at the opposite side (r.). (c) The rotational symmetry of the crystal is broken and a spiral will form, turning in the opposite direction of the crystal rotation. (Taken from Ref. [40])

will cool down much more than the other and the crystal will grow in that direction (see Fig. 2.2.1) and form a so called foot. Once this process has started, the crystal will not return to a cylindrical shape, since one side of the foot will stick out farther from the crystal (or be further removed vertically from the previous turn of the spiral) and so can radiate away much more heat. Schwabe et al. give a list of possible triggers [40]:

- Anisotropic heat conductivity of the crystal
- Non-circular (i.e. faceted) growth of the crystal
- Misorientation of the seed in materials with anisotropic heat conductivity
- Misalignment between the seed and the rotational axis
- Non-axially symmetric temperature field in the crucible (e.g. due to deformation of the crucible or when it is misaligned with respect to the RF coil)
- A crack in the crystal that destroys the symmetry of the heat transport
- Fluctuations in the temperature control
- Hydrodynamic instabilities: the flow regime loses its symmetry or becomes time dependent
- Particles (e.g. Ir) floating on the melt which can disturb the meniscus symmetry when they touch it
- Inhomogeneous deposition of material from the vapor (Pt, for example)
- Very low pulling rates where the meniscus becomes a significant part of the weight increase
- High melt viscosity which goes in parallel with low thermal conductivity of the melt and the crystal
- Decomposition of the melt that changes the surface tension
- Phase separation in the melt
- Mechanical disturbances of the setup

To avoid the spiral growth in $SrTiO_3$, the causes had to be investigated first. Uecker et al. [38] investigated the different tendencies towards spiral growth for $GdScO_3$, $DyScO_3$, $SmScO_3$ and $NdScO_3$. Some key data for these materials is summarized in table 2.2.1. For the scandates, the melting points and band gap energies are similar, but $GdScO_3$ is the only one of these scandates that does not have a significant room temperature NIR absorption, which is given as the reason for the lower spiraling tendency [38]. The trigger for the spiral formation often was hydrodynamic instability which could be remedied by using a conical baffle on top of the crucible, reducing the amount of heat radiation reflected back to the melt. This in turn improved the heat transport and subsequently the Marangoni flow, which results in a higher axial symmetry.

Doped or oxygen deficient $SrTiO_3$ shows free carrier absorption in the NIR, but spiral shaped crystals have been grown that do not show such an absorption at room temperature. Apparently, there is an absorption that only occurs at higher temperatures. This could be caused by impurities that act as deep donors or acceptors and so are not ionized at

Table 2.2.1.: Properties of some materials with a tendency towards spiral growth. (Band gaps of the scandates from [41], melting points, NIR absorption and spiraling tendency from [38]).

Material	**Melting point**	E_g **at 300 K (eV)**	**NIR absorption at 300 K**	**Tendency to spiral**
$GdScO_3$	≈2400 K	5.8	none	low
$DyScO_3$	≈2330 K	5.9	yes	high
$SmScO_3$	≈2400 K	5.6	yes	high
$NdScO_3$	≈2400 K	5.6	yes	high
$SrTiO_3$	2350 K	3.2	none	very high

room temperature. The formation of charged defects or a decrease of the band gap (which already is far smaller than the band gaps of the scandates at room temperature) could also be responsible. This is why the high temperature UV/VIS and NIR absorption of $SrTiO_3$ was investigated in chapter 4.

2.3. Growth methods

Over the years many methods have been used to grow STO. Here the ones relevant to this work are discussed.

2.3.1. Verneuil growth

The Verneuil or flame fusion process was developed by French chemist Auguste Verneuil in 1902 [42], who used it at first to make synthetic ruby. In this crystal growth technique, a very finely ground feed powder is fed into a hydrogen-oxygen flame. There it melts and the droplets fall down onto a seed crystal mounted on a rotating support which is moved downward to maintain a constant distance between the growing crystal and the flame (see Fig. 2.3.1 a and b). In the first stage of the growth, the growth parameters are adjusted to form a single crystalline neck of 5 to 10 mm length. The diameter is then increased, taking care to avoid overflow of the molten cap, and the cylindrical part is grown [43]. The hydrogen oxygen flame can be up to about 3100 K hot at its core, which makes this technique inherently suitable to high melting oxide materials such as Al_2O_3. For $SrTiO_3$, temperatures of about 2900 K where measured 100 mm below the burner [44]. The technique requires very high quality feed powder, since all impurities that do not evaporate will become part of the crystal. The quality of the crystals grown is somewhat limited since very high temperature gradients are involved (400-800 K cm^{-1} [43]).

The Verneuil method was the first technique used to grow STO in the 1950's [46]. It is a logical choice, since $SrTiO_3$ has a melting point of 2080°C. The Verneuil growth of $SrTiO_3$ has been optimized in the decades after. A burner with an additional oxygen inlet was introduced (see Fig. 2.3.1 a) [47], but still all crystals grown by this method are reduced in the as-grown state, as is shown by the blue-black color [48, 49] (see Fig. 2.3.2 a). Annealing of the as-grown crystals produces colorless or yellowish to light brown crystals [48, 49]. Some authors report annealing in oxygen rich atmospheres [49] while others use forming gas [48], which also results in insulating crystals after annealing at $\sim$ 1300 K. Mochizuki et al. used optical absorption spectroscopy to investigate the annealing process of Verneuil grown STO in a 90% Ar 10% H_2 atmosphere. The spectra are show in figure 2.3.2. The spectrum of the as-grown crystal

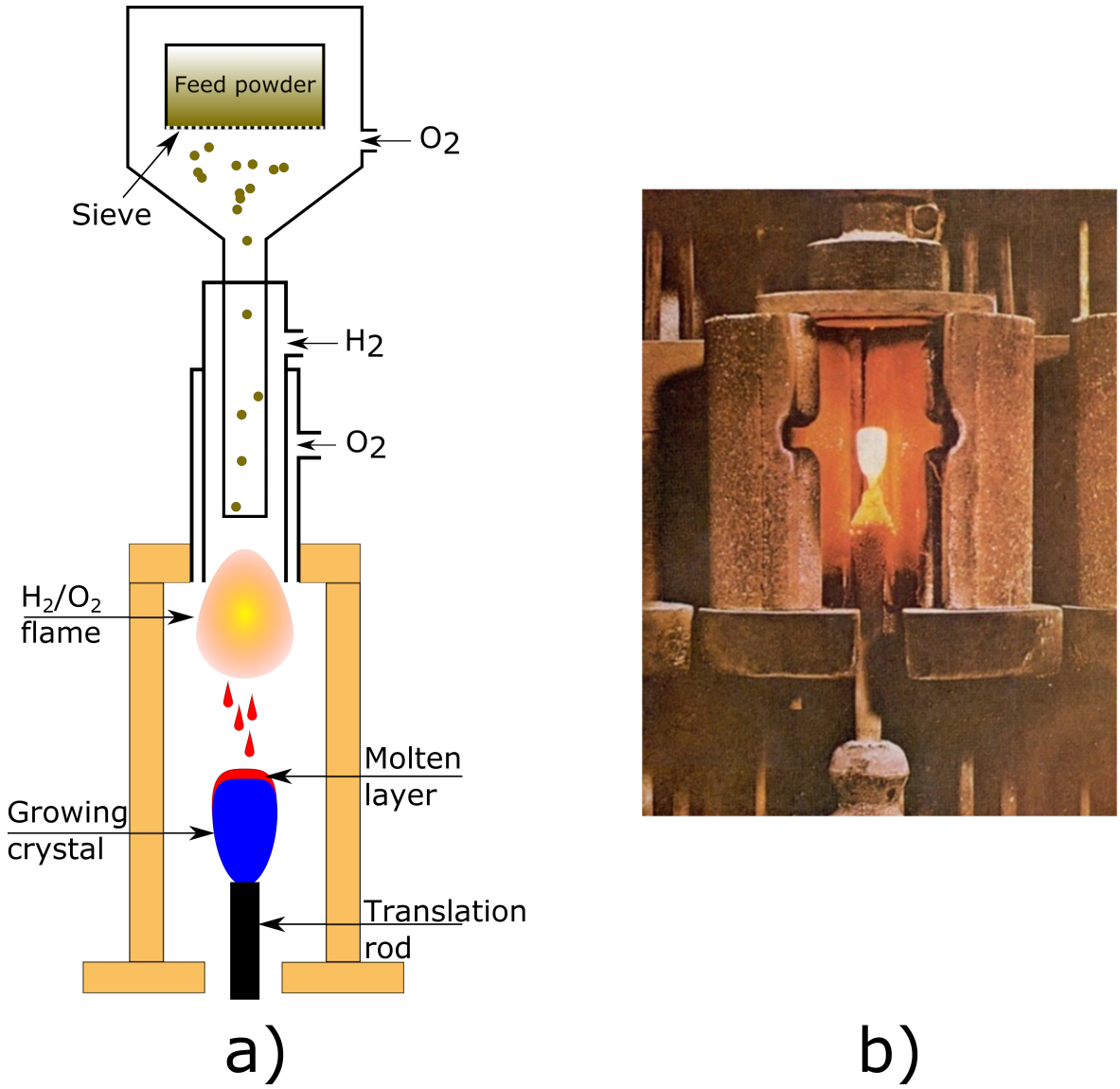

Figure 2.3.1.: Verneuil proces. a) Schematic depiction. b) Verneuil process in operation (from [45]).

shows a broad free carrier absorption which increases to long wavelengths (see section 4.2) and peaks at approximately 2.9, 2.4, 2.2, 2.1, 1.7 and 0.82 eV[48]. The peaks at 2.9 and 2.1 eV were assigned to Fe impurities in the crystals, while the peaks at 2.4 and 1.7 eV were assigned to intrinsic defects in $SrTiO_3$ [48, 50]. The free carrier absorption and the peaks could no longer be observed after 15 min of annealing at 973 K and the spectrum corresponds to that of colorless STO.

The main advantages of the Verneuil growth of $SrTiO_3$ are that there are high growth rates reported to be 20-26 mm/h [51], there is no crucible required, the setup is fairly simple and many dopants can be incorporated into the crystals (see for example Ref [52]). The main drawback is that the quality of the crystals is not very high, with EPD values typically in the $1 - 5 \times 10^6$ cm^{-2} range [51]. This is not expected to improve much further because of the large temperature gradient and difficulties in controlling the growth interface. Because this method is fairly cheap and equipment is relatively simple, almost all commercially available STO is grown this way.

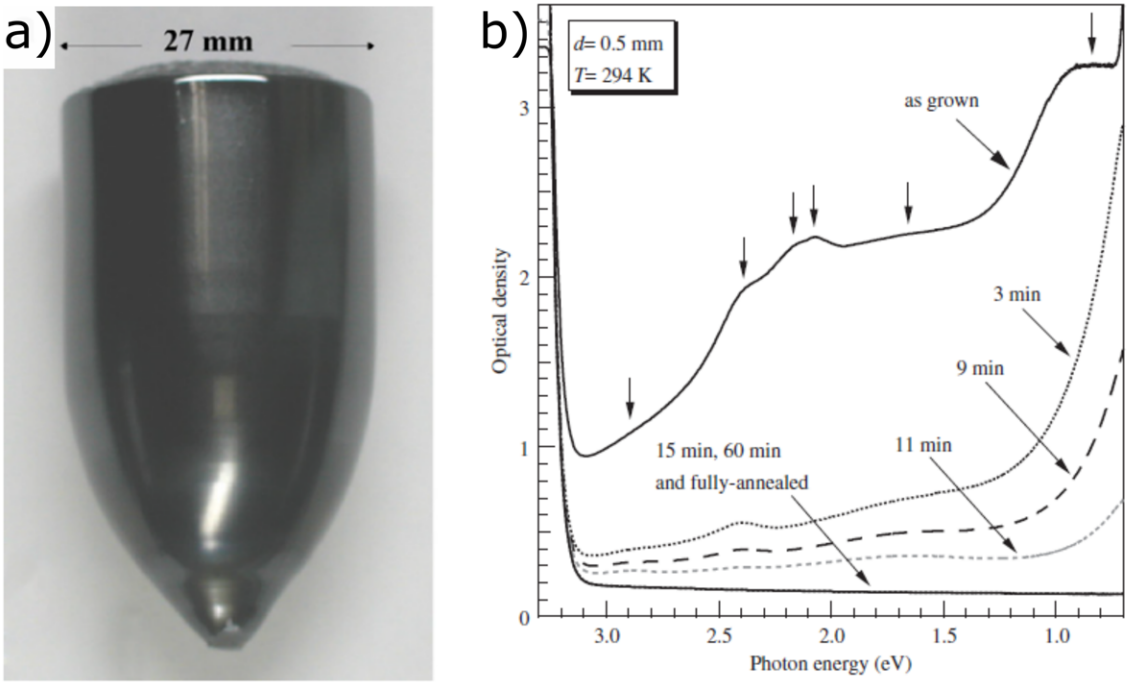

Figure 2.3.2.: a) Verneuil grown $SrTiO_3$ boule in the as-grown state [32] b) Optical absorption spectrum of as-grown and annealed $SrTiO_3$. (Taken from Ref. [48])

2.3.2. Czochralski growth

The Czochralski (Cz) growth technique is based on the method Jan Czochralski discovered in 1916 to measure the crystallization rates of metals [53]. In this technique, a batch of the desired material is melted in a crucible (see Fig. 2.3.3). Then a seed crystal is lowered on a translation rod until it touches the melt and the temperature is adjusted until a meniscus forms between the melt and the seed. The seed is rotated to reduce the effect of thermal inhomogeneities. If the conditions are right, the crystal grows when the seed is pulled upwards and takes the orientation of the seed. Through control of the temperature and the pulling and rotation rates, the shape of the meniscus can be controlled and by that the shape and diameter of the crystal. By first growing a very narrow section of crystal known as a neck, many dislocations can grow out of the crystal [54]. Then the diameter is increased and, when the desired value is reached, the diameter is maintained to grow the cylindrical body of the boule. When the crystal is separated from the melt, it receives a thermal shock which can cause dislocations and cracking. If the material allows it, the impact of this shock is usually reduced or even eliminated by slowly reducing the crystal diameter, forming an end cone. That way, the cylindrical part of the crystal cools down slower and if dislocations are formed that can propagate back into the crystal (as is the case for more plastic materials such as Si), the end cone acts as a buffer layer so the cylindrical part of the boule is not affected [55, 56]. The thermal stress caused by Czochralski growth and especially by the separation from the melt and the resulting damage to the crystal is highly material dependent. It is discussed in depth in references [55, 57, 58], for example.

One constraint on the crystal growth by the Czochralski method is the crucible material. It needs to be stable at the growth temperature and should interact only minimally with the melt or the atmosphere. When a compatible atmosphere and crucible material are available, large crystals of very high quality can be produced. Typical growth rates for oxide crystals are between 1 and 3 mm/h. Because of the good quality of the produced crystals and the high degree of automation possible, it is one of the principal methods for growing crystals industrially.

For STO, Cz growth is difficult, as it has a very high melting point (making Ir crucibles necessary) and poor radiative heat transport (see chapter 4). Because of the low radiative heat transport through the crystal (which dominates at temperatures close to the melting point), it is hard to control the shape of the growing crystal. The meniscus cools more to the sides than to the top, so when its symmetry is slightly disturbed one side will cool faster and hence the crystal will grown to one side, which can cause spiraling or foot formation (see section 2.2 and Fig. 2.3.4 a).

By using manual growth control, it was possible to grow puck shaped STO crystals with the Cz method, which have a large diameter of 30 to 42 mm but a short length of about 15 mm [59] (see Fig. 2.3.4). This required high pulling rates of 4-20 mm/h, a large undercooling and seeds with an orientation close to $\langle 110 \rangle$. The length of about 15 mm appears to be a critical maximum, because after that length the crystal starts melting back [59]. This is due to the poor heat conduction (2.2 W $(\mathrm{m\ K})^{-1}$ at temperatures $>$1700°C [30]) and low radiative heat transport through the crystal (see chapter 4): after a certain length, it is apparently no longer possible to remove the latent heat of crystallization from the interface fast enough for such high growth rates. Because of this, the heating power had to be continuously lowered (manually and similar to the classical Kyropoulos process) during the growth process to achieve a cylindrical crystal shape. Insufficient cooling makes the shape of the interface change from convex to concave, leading to back melting and separation from the melt. But if

the cooling rate is too high, a spontaneous and parasitic nucleation may start away from the growth interface, such as at the crucible bottom and/or on the melt surface away from the crystal periphery [59]. The crystals had EPD values between 4.3×10^5 and 1.4×10^6 cm^{-2}, while FWHM values between 68 and 210" and mosaicities between 274 and 616" were determined from rocking curve measurements [59]. All in all, stable long term growth of STO does not seem to be achievable with the Czochralski method and it is not very likely that the sought after increase in quality will be achieved with this method.

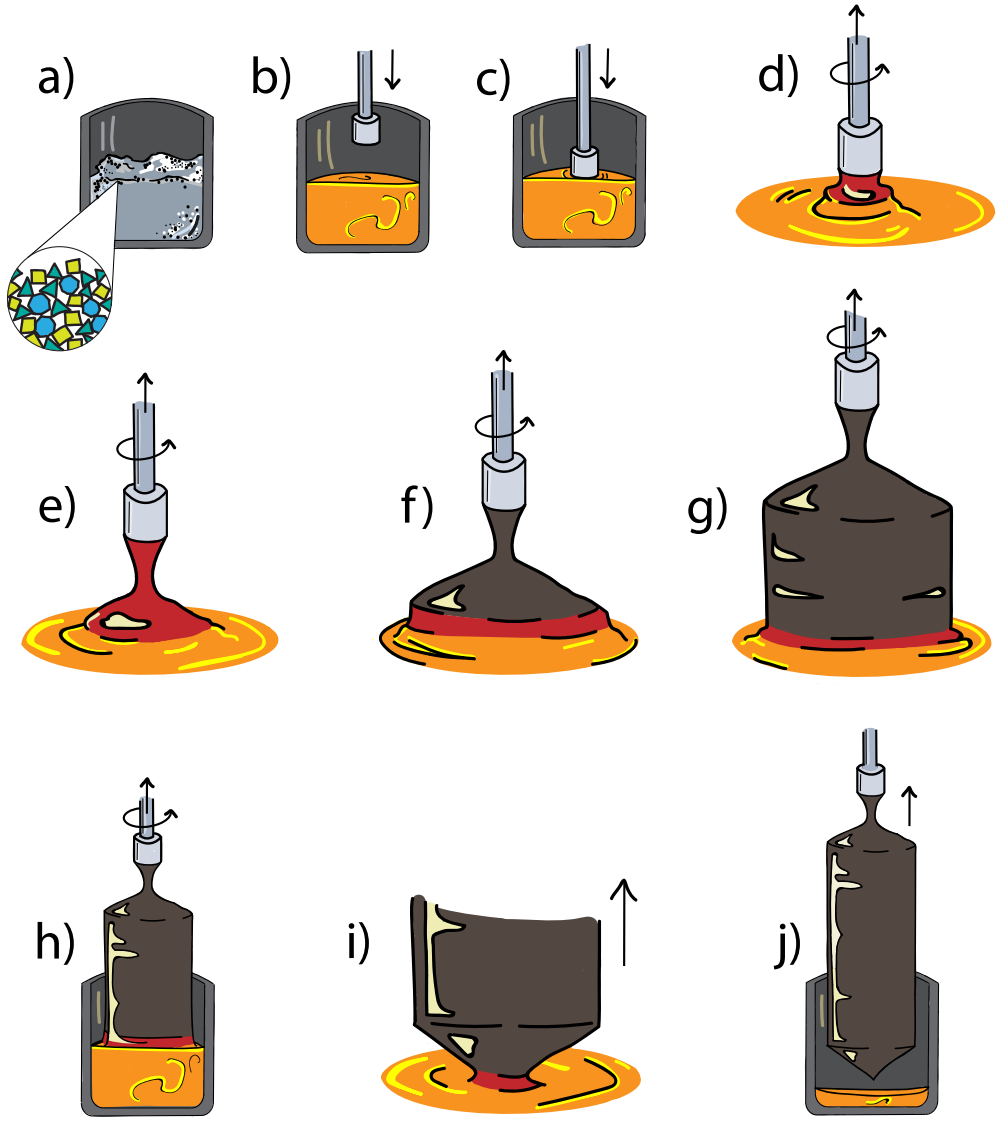

Figure 2.3.3.: Schematic illustration of the different steps of the Cz process. a) The crucible is loaded with the starting material. b) The starting material is melted and c) the seed is brought into contact with the melt. d) The seed is rotated and pulled upward, causing a melt meniscus to form which crystallizes at the top. e) A thin neck is grown to minimize the number of dislocations in the crystal (Dash-necking). f) The crystal diameter is slowly increased until the desired diameter is reached (g). h) When the desired length is reached, the crystal radius is reduced again to form an end cone (i) before separating the crystal from the melt (j) and slowly cooling everything down. (Illustration by Melanie Fuechsel)

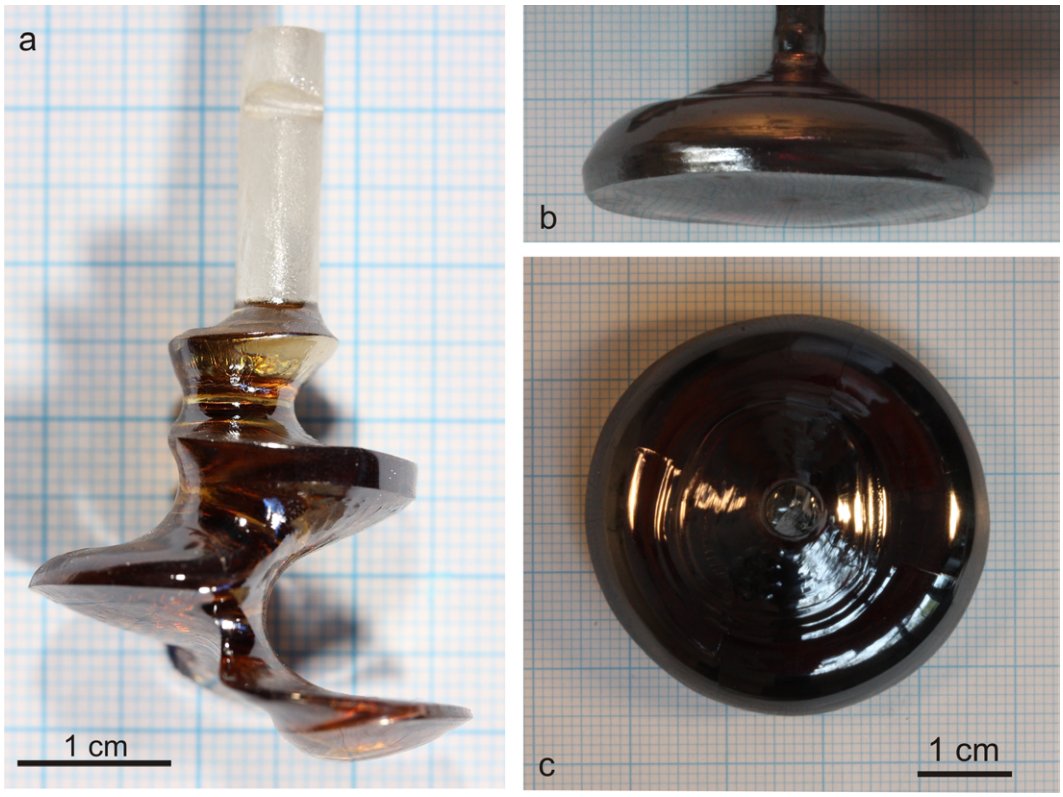

Figure 2.3.4.: $SrTiO_3$ single crystals grown by the Czochralski method. (a) Crystal showing typical spiraling and foot formation. (b) Side and (c) top view of a crystal with the desired convex interface shape b). The crystal shows well-developed ridges at the shoulder part (c). (Taken from [59])

2.3.3. Top-seeded solution growth

Top-seeded Solution Growth (TSSG) is a technique similar to the Czochralski method, except that it does not use a stoichiometric melt but a melt solution. The material for the crystal is mixed with a lower melting material called a flux. The advantage of this technique is that a lower growth temperature is possible, which also gives different options for e.g. different crucible materials and atmospheres. It does require detailed knowledge of the phase diagram in question and the flux has to be selected carefully: it should incorporate into the crystal as little as possible and the thermal expansion coefficient should be as close as possible to that of the desired crystal since this difference will cause strain and can lead to cracking if flux material cools on the crystal. Sometimes it is possible to use one component of the crystal as a flux (self flux growth), which largely solves the contamination problem. Drawbacks of this method include a slow growth rate (since the crystal is grown from a solution and not a stoichiometric melt [60]) and a smaller crystal volume, since only part of the melt can form the desired crystal.

This method was applied to $SrTiO_3$, as it was found that the heat transport through a growing crystal is low and highly temperature dependent (see chapter 4). Using top-seeded solution growth from a self flux, small high quality crystals with volumes between 0.5 and 3 cm^3 with etch pit densities between 10^2 and 10^3 cm^{-2} have been grown by Rytz et al. [61] and Oka and Unoki while Belruss et al. grew crystals with a volume of about 1 cm^3 with etch pit densities below 10^2 cm^{-2} . These growth runs from self flux took about one week. It is also possible to grow STO from borate fluxes, which yields crystals with simillar volumes and very low etch pit densities of $0 - 10^2$ cm^{-2}, but with growth times of about two months [62]. These crystals also tend to have borate inclusions, though inclusion free areas can be found.

To grow larger crystals from self flux, the TiO_2 rich side of the SrO-TiO_2 pseudo-binary phase diagram was investigated (see Fig. 2.4.1)[31]. The eutectic was found to be at 77 mol% TiO_2 and 1725 K. Crystals were first grown from a mixture of 75 mol% TiO_2 and 25 mol% SrO, starting at 1808 K. The temperature is continuously lowered because the ratio of TiO_2 to SrO increases as the crystal grows and the melt composition approaches the eutectic point. The growth rate for these crystals was about 0.2 mm/h and the diameter was up to about 15 mm (see Fig. 2.3.5). Because of the relatively low temperature, the crystals could be grown in air from a platinum crucible. The quality of these crystals was very high, with the EPD for the crystals grown in the $\langle 100 \rangle$ and $\langle 110 \rangle$ directions $1 - 2 \times 10^4$ cm^{-2}, which is up to two orders of magnitude better than Verneuil grown crystals [31].

A crystal was heterogeneously nucleated from a melt with 75% TiO_2. This crystal had a subgrain-free and virtually dislocation-free region, which was used as a seed to grow another crystal from a 75% TiO_2 flux in air [63]. This crystal has a diameter of about 7 mm and a length of 20 mm and showed no mosaicity in rocking curve measurements. It was investigated by defect selective etching which showed that the crystal is virtually dislocation free and the few areas where dislocations were found showed etch pit densities between 5×10^2 and 2.3×10^3 cm^{-2} [63]. The crystal is shown in figure 2.3.5 b.

To increase the yield, the initial mixture was adjusted to 70% TiO_2, which has a liquidus temperature of 2013 K [30]. In this case, the crystals were grown from an iridium crucible in pure or oxygen enriched nitrogen or argon atmospheres, respectively. The growth rates were the same, but the crystal diameters were increased to diameters exceeding one inch and the influence of the atmosphere on the growth stability and coloration was studied (see chapter 6). The growth conditions for the TSSG grown crystals investigated here are summarized in table 2.3.1.

Investigation of the dislocation densities of brownish crystals grown in an oxidizing atmosphere by TSSG below 2013 K has shown that typical EPD values are between 2×10^4 and

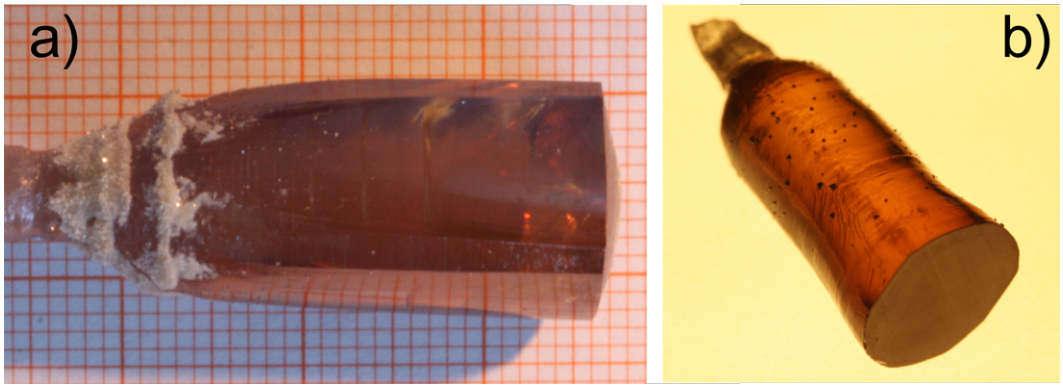

Figure 2.3.5.: Top-seeded solution grown crystal grown beneath 1808 K. a) crystal C2. The white substance on the crystal's shoulder is rutile and STO, grown from the gas phase [64]. b) crystal C3, grown from a dislocation free grain cut out of a crystal nucleated on a Pt tip [63].

2×10^5 cm^{-2} when using crystal seeds with higher EPD values ($4.6 \pm 0.75 \times 10^5$ cm^{-2}). In contrast, for a crystal grown under reducing conditions (as-grown crystal Re3) an etch pit density of $5.08 \pm 0.9 \times 10^5$ cm^{-2} was measured. In summary, the crystal growth conditions applied for crystals Ox1, Ox2, Ox3 and Ox5 were the most suitable conditions in terms of crystal quality, yield and growth stability.

Table 2.3.1.: Crystal growth conditions for the TSSG crystals (taken from Refs. [30, 31, 63]).

Crystal	**Atmosphere**	**After-heater**	**Growth rate (mm h^{-1})**	**Rotation rate (rpm)**	**Seed orientation**	**Initial liquidus temperature (K)**
C1	Air	No	0.2	20	⟨100⟩	1808
C2	Air	Yes	0.2	30	⟨100⟩	1808
C3	Air	Yes	0.2-0.3	20	⟨111⟩	1808
Ox1	Ar, 0.16 vol% O_2	Yes	0.2	3	⟨100⟩	2013
Ox2	Ar+0.16 vol% O_2	Yes	0.15	10	⟨100⟩	2013
Ox3	Ar+0.16 vol% O_2	Yes	0.2	10	⟨100⟩	2013
Ox4	Ar+2.83 vol% O_2	Yes	0.25	5	⟨100⟩	2013
Ox5	Ar+0.16 vol% O_2	Yes	0.2	10	⟨110⟩	2013
Ox6	Ar+0.16 vol% O_2	Yes	0.2	5	⟨110⟩	2073
Ox7	Ar+0.16 vol% O_2	Yes	0.2	10	⟨100⟩	2073
Ne1	5N Ar	Yes	0.2	10	⟨100⟩	2013
Re1	5N N_2	No	0.25	5	⟨100⟩	2013
Re2	5N N_2	Yes	0.33	10	⟨100⟩	2013
Re3	5N N_2	Yes	0.33	5	⟨100⟩	2013

2.3.4. Edge-defined film-fed growth

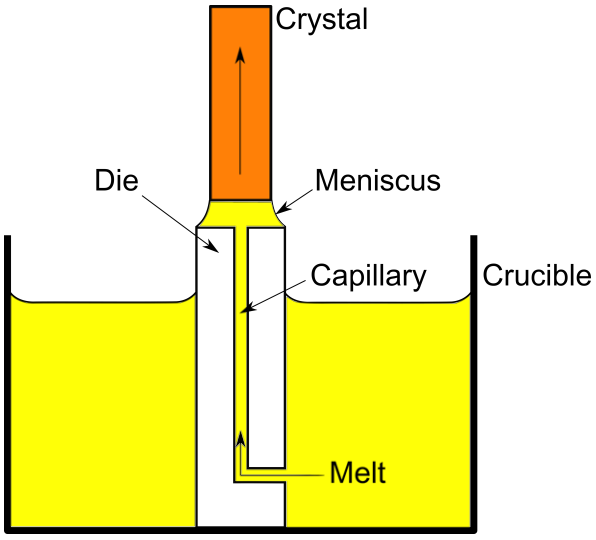

Figure 2.3.6.: Schematic of edge-defined film-fed growth. The melt rises up the capillary and the melt film assumes the shape of the die.

Edge-defined film-fed growth (EFG) was developed to grow Al_2O_3 crystals with specific profile shapes, such as tubes or ribbons [65, 66]. In the EFG method, a die with a capillary is placed in the crucible. This can be a floating die [67] or a die standing on the bottom of the crucible, which was used to grow $SrTiO_3$ [59]. The melt rises up the tube and wets the die at the top. The edges of the die pin the meniscus and determine the profile of the crystal, allowing almost any profile and the shape of the meniscus is stabilized. Since the growth front stays in the same location relative to the growth setup, it is easier to optimize the thermal gradients. Because of the long capillary and the high melt flow rate (around 75 cm/min for a 0.025 cm diameter corundum filament [65]), it is often possible to grow a crystal with a composition that matches the melt composition (partition coefficients near 1). The main prerequisite is a die material that is wetted by the melt and does not contaminate it with impurities.

Crystals with complicated cross sections and wide ribbons often do not have the highest crystal quality since high radial temperature gradients are required to expand the meniscus to the edges of the die, resulting in non-uniform thermal gradients across the crystal.

For the growth of $SrTiO_3$, the main advantage is the stabilized meniscus and the fixed position of the growth interface, which allows for a good control of the thermal conditions of the growing crystal. Since the objective was to grow high quality crystals that could be used as epitaxy substrates, a circular Ir die with a diameter of 15-16 mm was used [59]. A temperature difference of 12 K between the center and the edge of the die was used, which allowed a very gentle diameter enlargement of the crystal. For the cylindrical part, a growth rate of 2 mm/h was used and crystals with lengths of up to 50 mm were grown. Two crystals are shown in figure 2.3.7. The typical etch pit densities for these EFG crystals are between 8.2×10^4 and 2.8×10^5 cm^{-2} and mosaicities between 65 and 155" were determined [59].

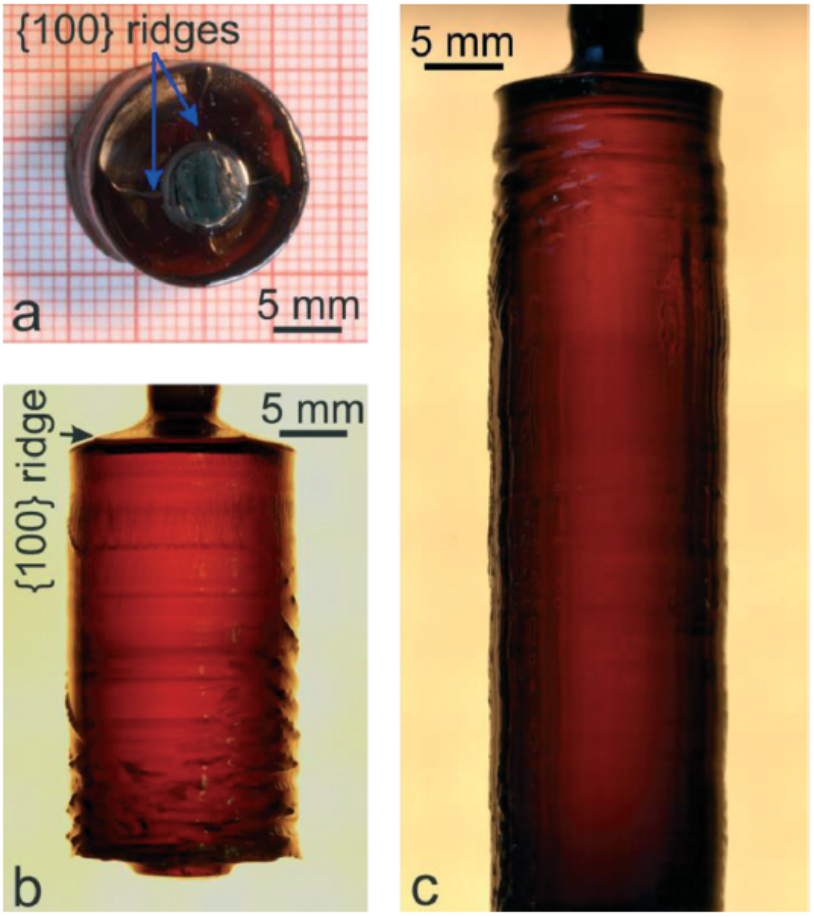

Figure 2.3.7.: $SrTiO_3$ crystals E1 (a), E2 (b) and E3 (c) grown by the EFG method. The crystals show well developed {100} ridges visible in a) and b) at the shoulder parts (taken from Ref. [59]).

2.3.5. Micro pulling down

The micro pulling down (MPD) technique is a growth method that is mostly used to grow single crystal fibers [68]. The material is melted in a crucible with one or more micro capillaries in the bottom, so the melt flows down to a nozzle at the end of the capillary where the surface tension keeps it from flowing out. A seed crystal is then brought into contact with the melt and is pulled downward. The nozzle serves a similar purpose as the die in EFG: the shape of the nozzle determines the shape of the meniscus and this makes it possible to shapes such as ribbons or square sticks [68]. In industry, this method is largely used to make fibers of laser materials, scintillators and other components. it is a very useful method in research applications due to its very high growth rates (up to several mm/min) with small batch sizes (typically $<$1 g), making it ideal for experimenting with new materials or dopants. Because of the fairly long capillary, diffusion back into the main melt reservoir is difficult and the crystal composition will be close to the melt composition. This is an advantage for doping, but makes growth of incongruently growing materials difficult [69].

$SrTiO_3$ was grown with the MPD to produce p-type doped samples. The idea was to attempt to compensate for the electrons released by oxygen vacancies and improve the high temperature infrared transmission (see chapter 5). First, experiments were performed to establish the growth of undoped STO. Shards of Verneuil-grown STO crystals were used as starting material. The high melting point of STO meant that an Ir crucible and afterheater had to be used. The growth chamber was evacuated to $10^{-4} - 10^{-5}$ mbar and then an Ar flow with varying oxygen concentrations was applied. The oxygen was added once the crucible was hot enough to avoid the formation of iridium oxide at lower temperatures [70]. The crystals were grown with growth rates between 0.5 and 1.5 mm/min. Two undoped crystals are shown in figure 2.3.9.

Reported p-type dopants for STO include Sc [71, 72], In [73], and Mg [74]. For these experiments, Sc was chosen as the dopant, since Sc:STO has been studied extensively by X-ray absorption spectroscopy (showing Sc is a deep acceptor) and the melting point of Sc_2O_3 is 2758 K. In_2O_3 has a melting point of only 2183 K and it is known that In species have a high vapor pressure over In_2O_3. MgO has a high melting point, but the p-type conductivity was found for Mg:STO ceramics and it is not entirely clear why this material is p-type since Mg is isoelectric with Sr while In and Sc prefer the 3+ ionization state and so give p-type conductivity when they are on a Ti^{4+} site.

For the Sc:STO fibers, material from a Cz grown STO crystal was used as starting material. The amounts weighed in were 1.585 g STO and 1.1 mg Sc_2O_3, which corresponds to 0.184 at% Sc. The growth chamber was evacuated to 10^{-6} mbar and heated under Ar flow. Near the growth temperature 1% of O_2 was added to the gas flow. So much melt flowed out of the crucible that it wetted the bottom of the crucible rather than the nozzle. The crystal was grown with 0.5 mm/min and had a radius of up to 5.5 mm (see Fig. 2.3.10). Two wafers were cut and polished from this crystal, MPD-Sc-1A and B. The measured Sc concentration in wafer A was 0.105±0.004 at%, much lower than the weighed in amount. This might be due to a segregation coefficient far from 1. The crystal does not appear to have a very high quality, but its unusually large diameter makes it very suitable for spectroscopic investigations.

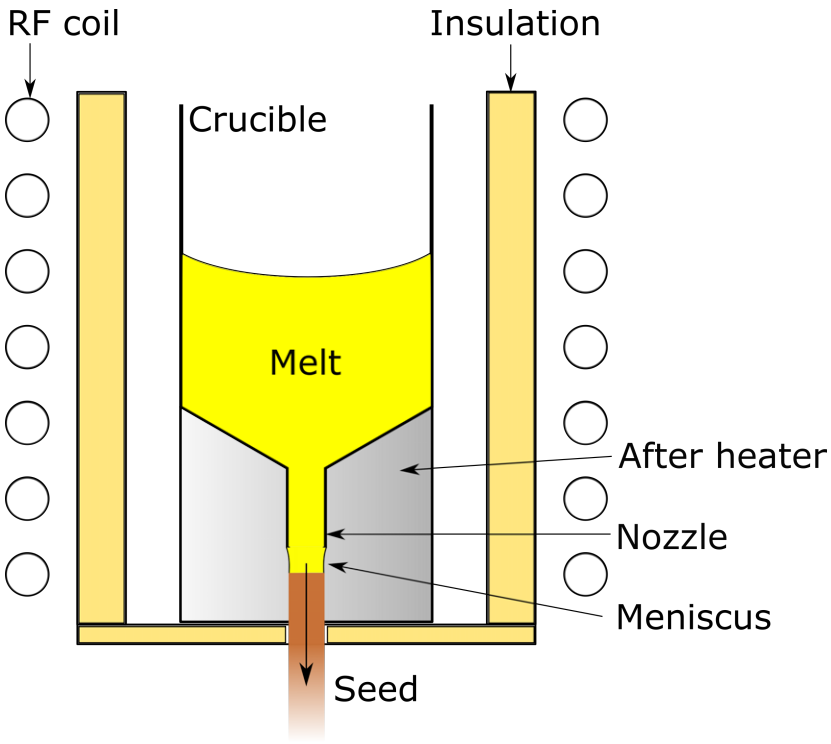

Figure 2.3.8.: Schematic depiction of a micro pulling down setup.

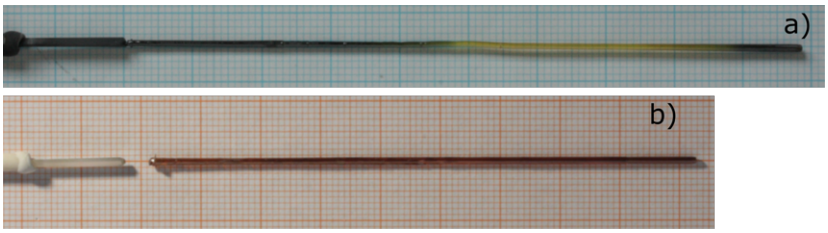

Figure 2.3.9.: MPD grown STO fibers. a) Grown in pure Ar. b) Grown in Ar+0.28% O_2.

Figure 2.3.10.: Crystal MPD-Sc-1.

2.3.6. Optical floating zone and laser heated pedestal growth

Floating zone methods started as a purification technique used mostly for semiconductor crystals. The floating zone methods work by melting a small area of a crystal or ceramic rod and then moving the rod slowly through the hot zone, melting the material at one end of the hot zone and crystallizing it at the other end [75]. If the solubility of the impurities in the melt is higher than in the solid (which is often the case), the impurity concentration in the melt will rise and high purity material is crystallized. The impure material is moved to the end of the rod and this area can be cut off. Different heating systems, such as resistive heating coils, induction heating and optical heating are used. Optical floating zone (OFZ) growth is often used to produce high melting insulators. Here the hot zone is produced by focusing the light from high power halogen or xenon lamps, as shown in figure 2.3.11.

Nabokin et al. used the OFZ method to grow $SrTiO_3$ crystals with a diameter of 15-20 mm and a length of 40-80 mm [28]. By adding a small annealing furnace to the growth setup, they managed to grow crack free crystals with etch pit densities of 1-5$\times 10^5$ cm^{-2} and mosaicities of 1-3'.

Laser heated pedestal growth (LHPG) is basically a miniaturized version of optical floating zone growth. In laser heated pedestal growth, crystal fibers with a diameter of up to a few mm are grown. While this growth method cannot produce crystals that would be usable as substrates, it has high growth rates (6 mm/h used here for STO) and does not involve a crucible or insulation, so almost any atmosphere can be used, while the impurity level is minimized. This makes LHPG a very useful tool to investigate new materials and the influence of different atmospheres on the fibers grown. Here, two series of $SrTiO_3$ fibers grown in atmospheres with different oxygen concentrations were investigated.

The ceramic feed material for the laser heated pedestal growth of STO was prepared from dried and mixed powders of $SrCO_3$ and TiO_2 with purities of 5N and 4N respectively [77]. Those were calcined in a platinum crucible at 1573 K for 48 h inside a $MoSi_2$ muffle furnace (Supertherm, Nabertherm, Germany). The mixture was subsequently crushed in a mortar and 3-way isostatically cold pressed (EPSI, Belgium) with the final run at 2000 bar. The obtained cylindrical bars were sintered at 1623 K for 15 h and cut into quadratic rods with a 3×3 mm square section. This way, two batches of feed ceramics were produced, one stoichiometric and one with 3 at% Sr-excess weighed in [77]. Feed rods with Sr excess were used to compensate the strong Sr evaporation (the equilibrium partial pressure of Sr species is in the mbar range at the melting point of STO, see section 2.4 and Ref. [30]), which is common practice in Verneuil growth [44].

The growth runs were performed using an LHPG setup (Cyberstar, France) similar to that described by Fejer et al. [79] and Feigelson [80]. The infrared radiation was produced by a 400 W duo CO_2 laser (Firestar F400, Synrad) with an output wavelength between 10.20 and 10.65 μm. The laser beam was guided into the growth chamber and focused by several mirrors (see Fig. 2.3.12) into the hot zone. Seed- and feed rod translation were controlled by high precision stepper motors. Two CCD video cameras monitored the growth process. Further, a standalone infrared pyrometer (Modline 5, Ircon, USA) was installed to determine the temperature of the hot zone. For every growth run, a static atmosphere with a well-defined oxygen concentration was used. TSSG-grown single crystals with $\langle 100 \rangle$ orientation and EPD values of 1.16 $\pm 0.36 \times 10^5$ cm^{-2} served as seed material for all experiments [77]. No afterheater and no crystal or feed rotation were applied. A detailed list of the experimental conditions is presented in table 2.3.2.

To start the growth procedure the tip of the feed rod was melted into a small droplet, which was brought into contact with the seed. Ardila et al. [81] reported that feed rods with a quadratic square section should be avoided because the circular shape of the laser spot might

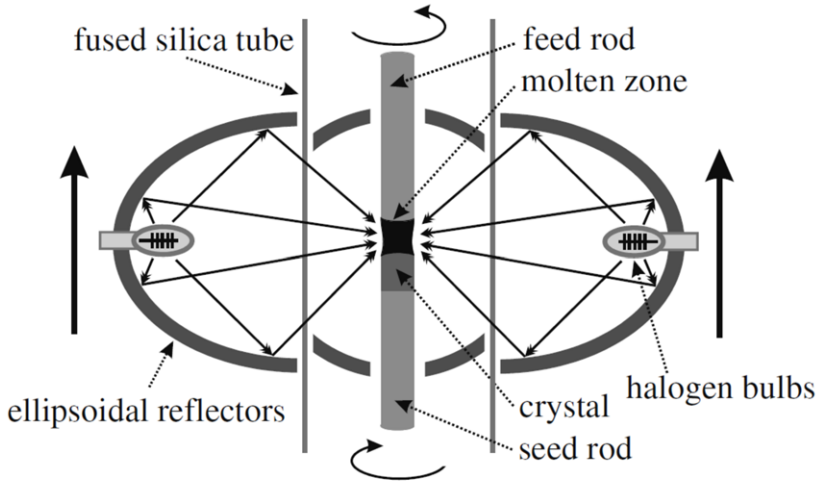

Figure 2.3.11.: General setup of an OFZ growth station. The light from the high powered halogen lamps is focused onto the tips of the feed and seed rod by elipsoidal mirrors, creating a molten zone which is moved along the feed rod to grow the crystal (from Ref. [76]).

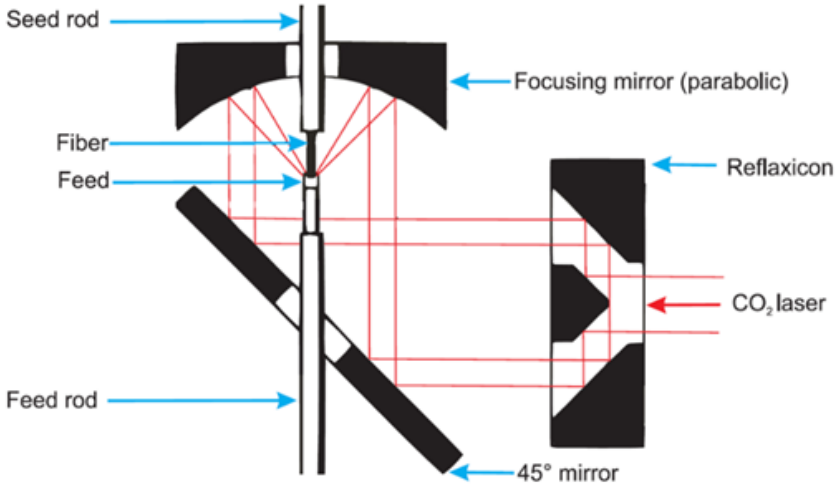

Figure 2.3.12.: Schematic of the LHPG setup. The laser beam is expanded in the reflaxicon to form a symmetrical hot zone between the feed rod and the growing fiber. (Taken from [78])

Table 2.3.2.: Growth conditions for all crystals. The dotted line divides the two growth series. "ST" refers to a stoichiometric feed rod, "SR" to strontium excess in the feed. The numbers refer to the oxygen concentration in the growth chamber. N_2 is used in addition to Ar atmospheres since it is more reducing because of NO_x formation at high temperatures. (Taken from Ref. [77])

Crystal	**Feed**	**Atmosphere**
ST40	Stoichiometric	Ar, 40 vol% O_2
ST20	Stoichiometric	Ar, 20 vol% O_2
ST10	Stoichiometric	Ar, 10 vol% O_2
ST5	Stoichiometric	Ar, 5 vol% O_2
ST1.3	Stoichiometric	Ar, 1.3 vol% O_2
ST0.9	Stoichiometric	Ar, 0.9 vol% O_2
STA	Stoichiometric	Ar
STN	Stoichiometric	N_2
STF	Stoichiometric	N_2, 5 vol% H_2
SR20	Sr excess	Ar, 20 vol% O_2
SR10	Sr excess	Ar, 10 vol% O_2
SR5	Sr excess	Ar, 5 vol% O_2
SR1.2	Sr excess	Ar, 1.2 vol% O_2
SR1.1	Sr excess	Ar, 1.1 vol% O_2
SR0.4	Sr excess	Ar, 0.4 vol% O_2
SRN	Sr excess	N_2

leave the corners of the square solid. This problem was bypassed by expanding the laser spot size manually until its diameter matched the diagonal of the feed rod. Upward movement of the seed remained constant at 6 mm/h for all growth runs. The speed of the feed rod had to be adjusted to the diameter of the growing fiber to ensure sufficient material supply into the hot zone from below (equilibrium was reached at 9 mm/h at maximum diameter of the fiber). The growth procedure was usually ended when the crystal length reached about one centimeter by stopping the feed rod translation. This way, the fiber diameter slowly decreased. An abrupt removing of the crystal would have led to shock cooling and shattering. Ideally, the separation process would end with the fiber leaving the melt in the shape of a very thin tip. The laser power was linearly decreased for 20 minutes until it reached zero. Using this method, single crystalline $SrTiO_3$ fibers with diameters of 2-3 mm and lengths up to 10 mm were grown. The different stages of an ideal growth run are illustrated in figure 2.3.13.

Etch pit densities were measured for 3 cleaved samples from the strontium rich series, two grown in Ar with 20% or 1.2% oxygen and one grown in pure N_2. The highest EPD value among measured fibers was found for the crystal grown under the highest oxygen partial pressure (crystal SR20): 4.4×10^6 cm^{-2}. Samples grown under lower oxygen partial pressures exhibit a lower dislocation density (1.1×10^6 cm^{-2} for SR1.2 and 8.6×10^5 cm^{-2} for SRN). These results show that it is apparently not possible to preserve the increased quality of the TSSG seed crystal (EPD of $1.16 \pm 0.36 \times 10^5$ cm^{-2}) by the standard LHPG method.

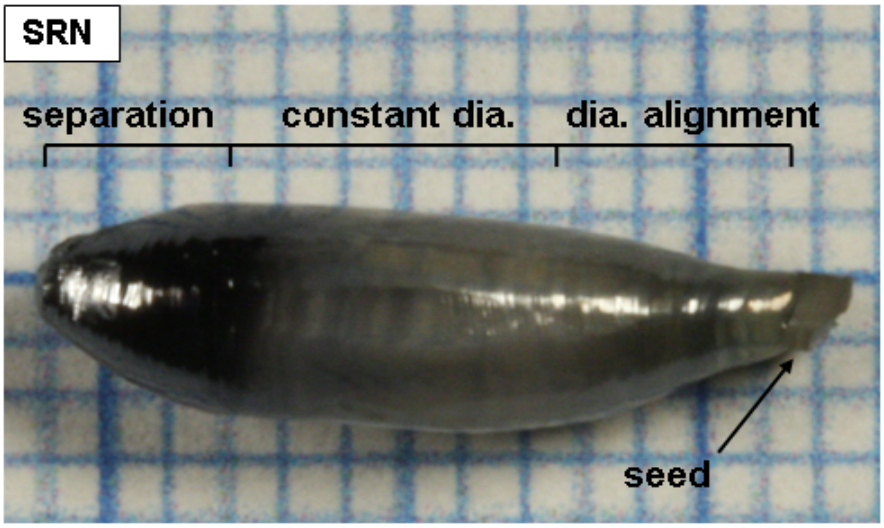

Figure 2.3.13.: Stages of an ideal growth run shown for crystal SRN. The size of the squares is 1×1 mm. Samples for spectral and chemical analysis were prepared from the cylindrical part grown at a constant diameter. (Taken from Ref. [77])

2.3.7. Comparison

The typical best quality, size and growth rates of the methods discussed above are compared in table 2.3.3. This table shows that the highest crystal quality is obtained by growing from a self flux or borate flux with a very low growth rate. But since these crystals have a volume of just 0.5-3 cm^3, they are not relevant for commercial scale substrate production. The most promising approach to large high quality STO crystals appears to be the use of low temperature TSSG with a pulling rate of 0.2 mm/h to grow mosaicity free seeds with low EPD's for EFG growth, which has a growth rate of 2 mm/h for the cylindrical section. This is especially promising if the diameter of the EFG crystals can be increased without a significant loss of quality.

Table 2.3.3.: Comparison of typical best crystal quality produced by the different growth methods. *These values are growth rates, no crystal pulling was reported. †For a crystal grown frown a dislocation free grain of a crystal nucleated on a Pt tip.

Method	**EPD (cm^{-2})**	**FWHM**	**Mosaicity**	**Diameter (mm)**	**Length (mm)**	**Pulling rate (mm/h)**	**References**
Verneuil	$1 - 5 \times 10^6$	0.54-1.22'	300-480"	27	50	20-26	[32, 51, 62, 82]
Czochralski	$3.2 - 5.4 \times 10^5$	68-210"	274-616"	30-42	15	4-20	[59]
TSSG below 1823 K	$10^2 - 10^3$	-	90"	24×24	10	≈ 0.3*	[61, 83]
TSSG below 1808 K	virtually dislocation free, in small areas $5 \times 10^2 - 2.3 \times 10^3$	45"	none†	7	≈20	0.2-0.3	[63]
TSSG below 2013 K	$2 \times 10^4 - 2 \times 10^5$	25"	468"	30	50	0.15-0.33	[30]
TSSG (borate flux)	$0 - 10^2$	<1'	Traces	9×11	12	≈ 0.03*	[51, 62]
EFG	$1 - 1.7 \times 10^5$	31"	65-155"	15-16	50	2	[59]
OFZ	$1 - 5 \times 10^5$	65"	60-180"	20	80	8	[28]
LHPG	$8.6 \times 10^5 - 4.4 \times 10^6$	-	-	2-3	10	6	[77]
MPD	-	-	-	1-5	20-100	≈ 60	-

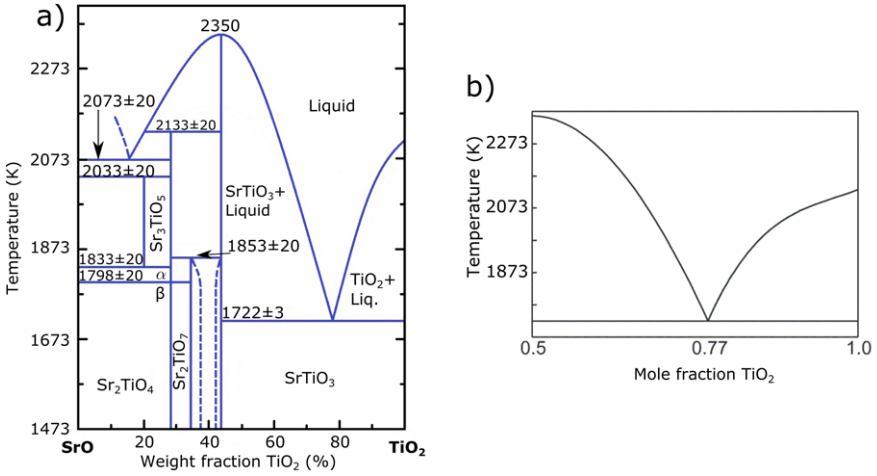

Figure 2.4.1.: a) Phase diagram of the SrO-TiO_2 pseudo binary system (Image source: ACerS – NIST standard reference database 31). b) TiO_2 rich side of the phase diagram, investigated in detail by Guguschev et al. [31].

2.4. Thermodynamics and non-stoichiometry

The phase diagram of the pseudo binary SrO-TiO_2 system is shown in figure 2.4.1. It shows that there are several phases with different compositions, but $SrTiO_3$ is only found in the cubic perovskite structure and does not have other polymorphs besides the transition to a tetragonal phase at about 105 K [84]. The TiO_2 rich side of the phase diagram has been explored carefully by Guguschev et al. [31] since the liquidus temperature is much lower on that side, which makes top-seeded solution growth from self flux attractive (see section 2.3.3). The SrO rich side of the phase diagram is not attractive for this method since the liquidus temperatures are much higher and growth in a very SrO rich regime could lead to the formation of Ruddlesden-Popper (RP) phases. The RP phases are a series of phases with the general formula $Sr_{n+1}Ti_nO_{3n+1}$: they consist of SrO layers separated by n layers of regular $SrTiO_3$[85–88].

$SrTiO_3$ can accommodate a large concentration of both cation and anion defects. This was shown by for example McCarthy et al. [89], who performed extensive studies in the ternary Sr–Ti–O system at 1648 K and found significant phase widths for $SrTiO_3$. Cation vacancy concentrations up to at least 0.12 at% have been found in $SrTiO_3$ ceramics [90], while cation excesses and deficiencies up to 2.8 at% have been reported for $SrTiO_3$ thin layers [91]. Also, up to 1 in 6 oxygen atoms can be removed from the material without losing the cubic perovskite structure or changing the lattice parameter much [89, 92]. This is probably due to Ti going from an oxidation state of 4+ to 3+ and so accommodating the charge difference. Since the crystal growth experiments discussed here are all performed at temperatures >>1648 K, it is expected that even larger deviations from stoichiometry are possible, at least in a metastable state. Local deviations from stoichiometry, measured by photoemission electron microscopy, were reported in the thesis of Annemarie Köhl, who performed microspectroscopy on Fe doped $SrTiO_3$ thin films before and after resistance switching [93]. A defect complex resembling a rectangular Ruddelsden-Popper phase was proposed as an explanation for the spectra found in the non-stoichiometric areas.

Fugacities

Thermodynamic equilibrium calculations were employed to find the most abundant vapor phase species formed during the growth process in slightly reducing and oxidizing conditions used for the TSSG growth (see Table 2.3.1 for the used gases and gas mixtures). Nitrogen is more reducing at high temperatures than argon, because in nitrogen the oxygen content is lowered due to the formation of nitric oxide, NO and related species. The calculations were done using the FactSage software package. For the calculations, one mole of $SrTiO_3$ was equilibrated with 100 moles of the corresponding gas under a total pressure of one bar. Thermodynamic data for the gases were taken from the FactSage databases. Data for the $SrO - TiO_2$ melt and for relevant solid phases were taken either from the same databases or, if applicable, from Ref [31].

From the thermodynamic point of view, stoichiometric $SrTiO_3$ evaporates under partial dissociation:

$$SrTiO_3(s) \rightarrow SrO(g) + TiO_2(g) \tag{2.4.1}$$

Especially at very high temperatures and under strongly reducing conditions, however, further dissociation according to

$$SrO(g) \rightarrow Sr(g) + O(g) \tag{2.4.2}$$

or

$$TiO_2(g) \rightarrow TiO(g) + O(g) \tag{2.4.3}$$

respectively, may occur (at low oxygen partial pressure and high temperature oxygen appears mainly atomic rather than molecular). Figure 2.4.2 demonstrates this for five different growth atmospheres that were used in the TSSG experiments. As depicted there, SrO and TiO_2 fugacities are independent of the atmosphere as long as the crystal composition is stoichiometric. The fugacity of SrO can exceed one mbar, which is remarkably high and results in strong evaporation even for bulk growth processes where the surface/bulk ratio is comparably small. TiO_2 is much less volatile, but close to the melting point of $SrTiO_3$ its fugacity approaches 10^{-6} bar which may result in significant evaporation, at least if large surfaces are exposed. The dominant, but not exclusive, evaporation of Sr metal-rich volatile species is in agreement with experimental findings [89].

Additionally, it was demonstrated that the fugacity of SrO and TiO_2 at the liquidus temperature is not only a function of temperature, but also of the composition of the melt solution [31]. With the thermodynamic data assessed there, equilibria between solids ($SrTiO_3$, TiO_2), liquids ($SrO–TiO_2$ melt), and the gas phase (SrO(g), TiO_2(g)) were calculated, and the results are summarized in figure 2.4.3. It turns out that SrO has the highest vapor pressure, expressed by its fugacity f. p_{SrO} is $\gtrsim$3 mbar for pure $SrTiO_3$ at its melting point [31]. For the "reduced species" Sr and TiO, the fugacity rises in the order of air $<$ N_2 (2.83 vol% O_2) $<$ Ar (0.16 vol% O2) $<$ Ar $<$ N_2. For these calculations it was assumed that the latter N50 gases contain a residual oxygen partial fugacity of 2×10^{-6} bar, which proved realistic in recent experiments [70]. As mentioned before, nitrogen is more reducing than argon, because in nitrogen the oxygen content is reduced further by the formation of nitric oxide, NO, and similar species.

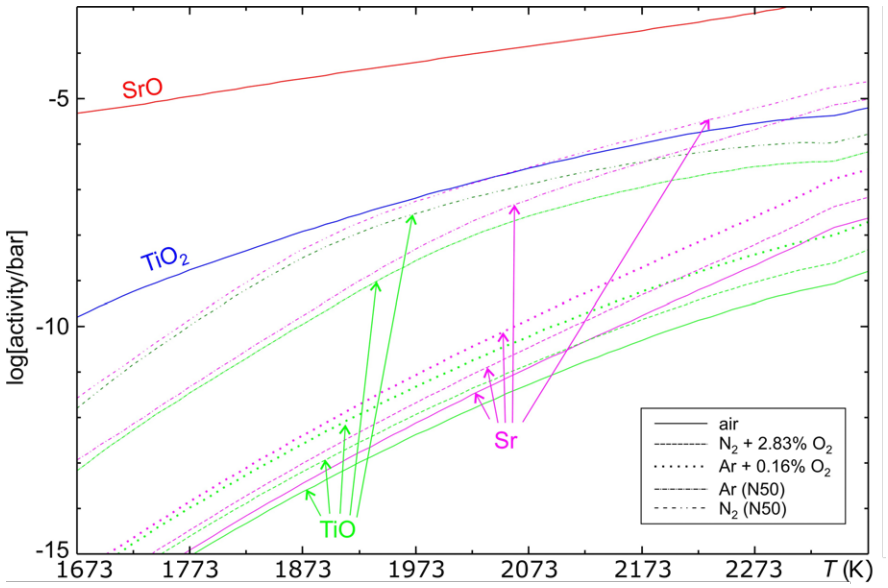

Figure 2.4.2.: Activities of the gaseous species SrO, TiO_2, Sr and TiO depending on temperature for different growth atmospheres. Note: SrO and TiO_2 activities do not depend on oxygen partial pressure (from Ref. [30]).

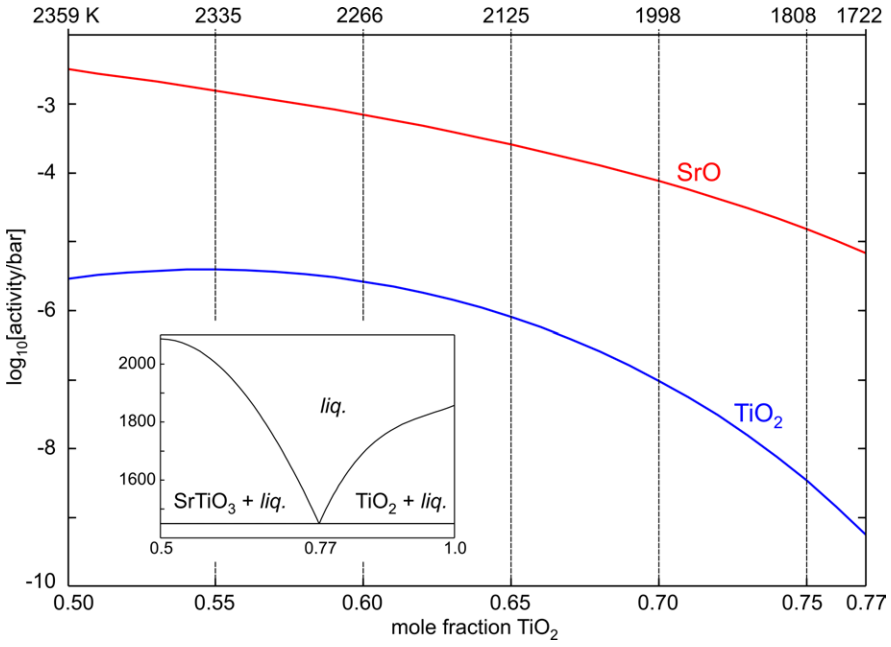

Figure 2.4.3.: Fugacity of the main species SrO(g) and TiO_2(g) over a $(1-x)$SrO+$x$$TiO_2$ melt for compositions ranging from $SrTiO_3$($x = 0.5$) to the $SrTiO_3$/TiO_2 eutectic ($x = 0.77$) at the corresponding liquidus temperatures $T_{liq(x)}$ which are given as labels on the upper abscissa. The inset shows the phase diagram between $SrTiO_3$ and TiO_2 (taken from Ref. [31]).

2.5. Point defect formation energies

Varley et al. and Liu et al. recently performed ab initio calculations to determine the formation energies of different point defects and combinations of point defects in $SrTiO_3$ in different chemical environments. The formation energy of, for example, an oxygen vacancy is given by:

$$E^f(V_O^q) = E_{tot}(V_O^q) - E_{tot}(SrTiO_3) + \mu_O + q \times \epsilon_F + \Delta^q \tag{2.5.1}$$

where $E_{tot}(V_O^q)$ is the total energy of a supercell with an oxygen vacancy with charge state q, $E_{tot}(SrTiO_3)$ is the energy of a perfect crystal in the same supercell, $q \times \epsilon_F$ represents the electron chemical potential or Fermi level, Δ^q is a correction for the finite size of the supercell and μ_O is the chemical potential of oxygen [94, 95]. The chemical potentials can vary over a wide range, limited by the stability condition for STO:

$$\mu_{Sr} + \mu_{Ti} + 3\mu_O = \Delta H_f(SrTiO_3), \tag{2.5.2}$$

where the chemical potentials are $\mu_x \leq 0$, referenced to pure solids of Sr and Ti and molecular oxygen [94, 95]. The formation of TiO_2 and SrO further limit the chemical potentials:

$$\mu_{Ti} + 2\mu_O < \Delta H_f(TiO_2), \tag{2.5.3}$$

$$\mu_{Sr} + \mu_O < \Delta H_f(SrO). \tag{2.5.4}$$

Therefore, for a given oxygen chemical potential, the chemical potentials of Ti and Sr can vary within [94]:

$$\Delta H_f(SrTiO_3) - H_f(SrO) - 2\mu_O < \mu_{Ti} < H_f(TiO_2) - 2\mu_O, \tag{2.5.5}$$

$$H_f(SrTiO_3) - H_f(TiO_2) - \mu_O < \mu_{Sr} < H_f(SrO) - \mu_O. \tag{2.5.6}$$

The values of μ_{Ti} and μ_O for which $SrTiO_3$ is stable are given in figure 2.5.1.

With these limits, Varley et al. calculated the formation energies for Sr, Ti and O defects for different values of ϵ_F for oxygen rich conditions and chemical potentials corresponding to a hydrogen annealing experiment by Tarun and McCluskey [96] ($\mu_O = -3.20$ eV and $\mu_H = -0.61$ eV). The results show that V''_{Sr} and $V^{\bullet\bullet}_O$ are the stable defects for Sr and O over the entire range while the ionization state of the Ti vacancy changes with the Fermi level. The energies of the most favorable defects are shown in figure 2.5.2. It is clear that the formation energy of the cation vacancies is much higher in oxygen poor than oxygen rich conditions.

Liu et al. also calculated the formation energy for combined defects like anti-sites, though their calculation method is less advanced and did not predict the band gap as accurately as the method used by Varley et al. [94, 95]. While the defect formation energies might not be exact, the defects with low formation energies should still be common. For SrO rich conditions, Liu et al. found that the following defect formation reaction had the lowest ΔH:

$$SrO + \frac{1}{2}Ti^{\times}_{Ti} + \frac{1}{2}O^{\times}_O \rightleftarrows \frac{1}{2}SrTiO_3 + \frac{1}{2}V^{\bullet\bullet}_O + \frac{1}{2}Sr''_{Ti} \tag{2.5.7}$$

with a ΔH of 2.89 eV [95]. Under TiO_2 rich conditions, two reactions have a very similar ΔH:

$$TiO_2 + \frac{2}{3}Sr^{\times}_{Sr} \rightleftarrows \frac{2}{3}SrTiO_3 + \frac{1}{3}Ti^{\bullet\bullet}_{Sr} + \frac{1}{3}V''_{Sr}, \tag{2.5.8}$$

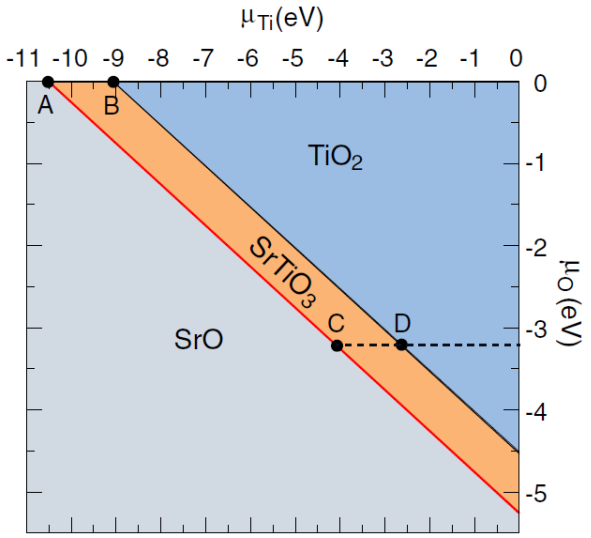

Figure 2.5.1.: Allowed values of Ti and O chemical potentials defining the stability of $SrTiO_3$. The chemical potential μ_O, μ_{Ti} and μ_{Sr} are limited by the formation of SrO and TiO_2 as described in the text. The line joining A and B corresponds to $\mu_O = 0$, while the line between C and D corresponds to $\mu_O = -3.20$eV, i.e., to the experimental conditions in Ref. [96] (taken from Ref. [94]).

and

$$TiO_2 + Sr_{Sr}^{\times} + O_O^{\times} \rightleftarrows SrTiO_3 + V_{Sr}'' + V_O^{\bullet\bullet}, \tag{2.5.9}$$

with $\Delta H = 1.90$ and 1.85 eV, respectively.

The most important findings for the discussions in this work is that O and Sr vacancies are always ionized and Ti vacancies are ionized over a large part of the possible values of the Fermi level. Cation vacancies have a much lower formation energy in oxygen poor conditions than in oxygen rich ones and cation anti-site defects are common when one cation has a significantly higher concentration.

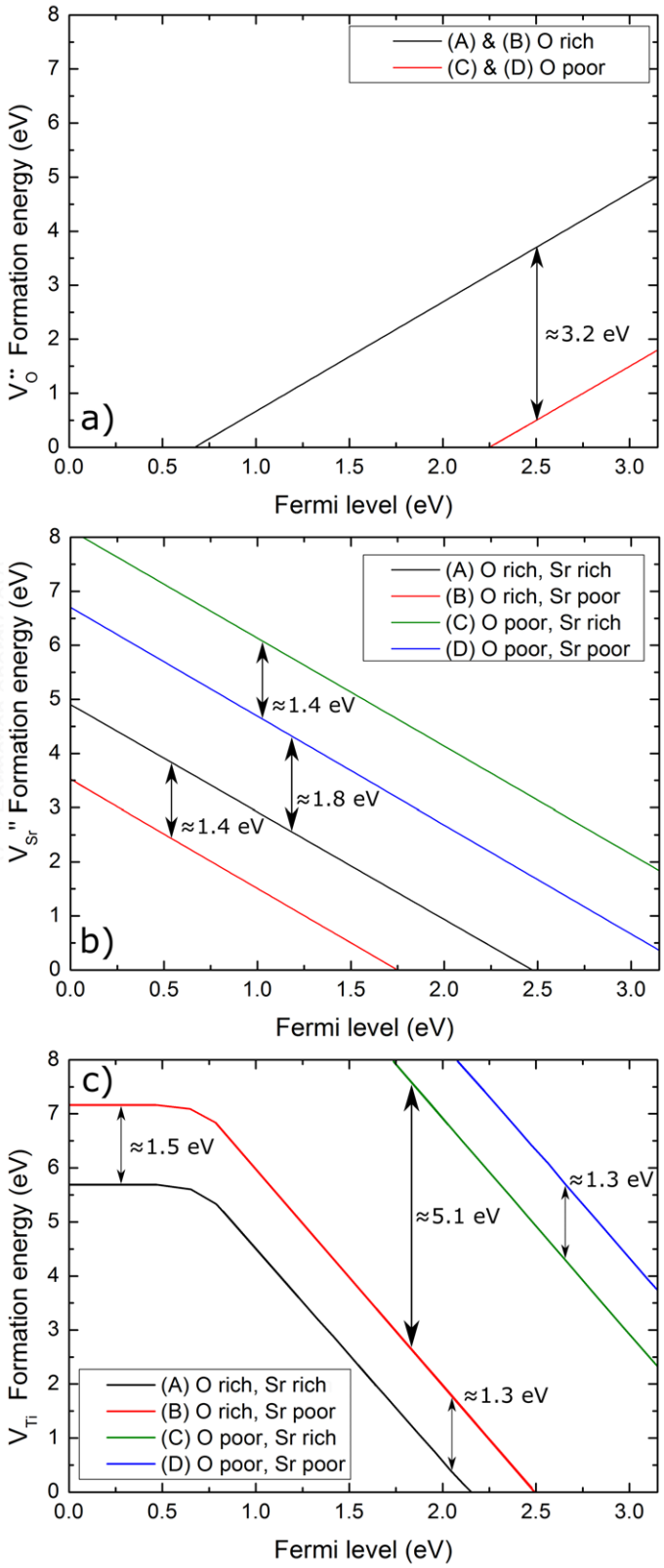

Figure 2.5.2.: Defect formation energies for a) $V_O^{\bullet\bullet}$, b)V_{Sr}'' and V_{Ti} (with different charge states), calculated by Varley et al. [94]. (A), (B), (C) and (D) correspond to the points marked in figure 2.5.1.

2.6. Spectroscopic methods

2.6.1. General principles

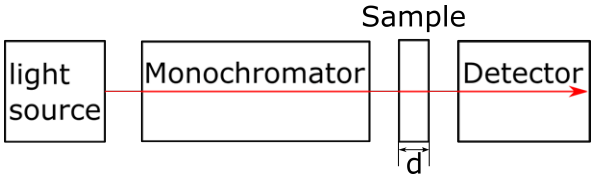

Figure 2.6.1.: General principle of spectroscopy.

Spectroscopy is the quantitative measurement of the optical properties of a material as a function of wavelength. When light strikes a material, different molecular processes, like the breaking of bonds, electronic excitation, rotation or vibration, occur, depending on the photon energy [97]. A schematic depiction of the measurement of a transmission spectrum is shown in figure 2.6.1. A ray of ligth from a suitable source is passed through a monochromator to select a single wavelength, through the sample, and into a detector. The selected wavelength is scanned over the desired wavelength range. The transmission is defined as the fraction of original light that passes through the sample and is calculated using:

$$Tr = \frac{I}{I_0} \tag{2.6.1}$$

With Tr the transmission, I_0 the initial intensity of the beam and I the intensity of the beam after passing through the sample. In practice, a spectrometer usually has a reference beam, which has nearly the same optical path, but does not pass through the sample, so I_0 can be measured in the same conditions.

Absorbance, sometimes called optical density, is defined as:

$$A = \log\left(\frac{I_0}{I}\right) = -\log(Tr) \tag{2.6.2}$$

Absorbance is important because it is directly proportional to the concentration, c, of the absorbing species [97]:

$$A = \epsilon d c \tag{2.6.3}$$

With ϵ the extinction coefficient (also known as molar absorptivity) in cm^{-1} and d the sample thickness in cm. This is called the Lambert-Beer law. For solid samples, the concentration $c = 1$. The extinction coefficient determined this way includes the absorption in the sample and the reflection at the surface. To compensate for this, the absorption coefficient, α, can be calculated using [98]:

$$\alpha = -\frac{1}{d}\ln\frac{\sqrt{(1-R)^4 + 4Tr^2R^2} - (1-R)^2}{2TrR^2} \tag{2.6.4}$$

With R the reflectance. The absorption coefficient is very useful since it does not depend on sample thickness and is sensitive to the processes that absorb the light in the material, which can be calculated from theory.

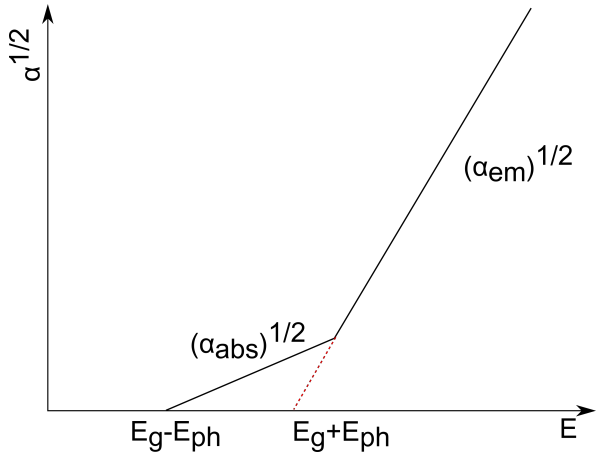

Figure 2.6.2.: Determining the band gap energy for an indirect allowed absorption (after [99]).

2.6.2. Determining band gap values from optical spectra

The largest absorption in the spectrum of a semiconductor is usually the band gap. When the photon energy is high enough, charge carriers are excited over the band gap. The band gap energy can be determined from a spectrum if the type of band gap and transition is known (direct or indirect semiconductor and allowed or forbidden optical transition). For a direct allowed absorption, the absorption coefficient around the band gap is given by [99]:

$$\alpha(\nu) \propto \sqrt{h\nu - E_g} \tag{2.6.5}$$

with ν the frequency of the light, h Planck's constant and E_g the band gap energy. From this equation, it follows that when α^2 is plotted against the photon energy, there is a linear part in the graph where $h\nu$ is close to E_g. When this linear part is extrapolated to $\alpha^2 = 0$, the band gap energy is found. This type of graph is known as a Tauc plot [100].

A direct forbidden transition occurs when the direct transition between the conduction and valence bands is forbidden by a selection rule (for example symmetry forbidden or spin forbidden) at the extreme point of the density of states, but allowed in the neighborhood of the extreme. The equation for α near E_g then becomes [99]:

$$\alpha(\nu) \propto (h\nu - E_g)^{3/2} \tag{2.6.6}$$

So in this case $\alpha^{2/3}$ is plotted against the photon energy and again extrapolated.

In an indirect semiconductor like $SrTiO_3$, the maximum of the valence band is at a different point in the Brillouin zone than the minimum of the conduction band. This means that a phonon has to be emitted or absorbed to maintain the momentum in this transition. This is reflected in the equation for α near E_g [99]:

$$\alpha(\nu) \propto (h\nu - E_g \pm E_{ph})^2 \tag{2.6.7}$$

Where E_{ph} is the energy of the phonon involved. This means that a plot of $\sqrt{\alpha}$ versus the photon energy will show two linear parts around the band gap energy, one corresponding to phonon absorption and one to phonon creation (see Fig.2.6.2).

For a forbidden indirect absorption, α near E_g is given by [99]:

$$\alpha(\nu) \propto (h\nu - E_g \pm E_{phonon})^3 \tag{2.6.8}$$

and E_g can be found from a plot of $\alpha^{1/3}$ versus photon energy.

The different shapes of the absorption curves can be used to determine the type of the band gap experimentally, especially if the size of the absorption coefficient and the temperature dependence are considered as well [99].

2.7. Mie scattering

Gustav Mie described the scattering and absorption of electromagnetic radiation at a spherical metallic particle in a continuous dielectric medium by applying the Maxwell equations [101]. When an electromagnetic wave interacts with such a particle, the electrons at its surface oscillate in response. From quantum mechanics, it is known that such oscillations are quantized and the eigenmodes of such collective oscillations are known as plasmons (in the case of electrons at the surface of small metallic particles these are more specifically surface plasmon polaritons). When the frequency of the radiation is in resonance with the eigenfrequency of the surface plasmons, the oscillation of the electrons becomes strong and the radiation is absorbed.

The extinction, scattering and absorption cross sections of the particles, σ_{ext}, σ_{sca} and σ_{abs}, are calculated from the complex dielectric functions of the particles and the medium through $m = \sqrt{\epsilon_{particle}/\epsilon_{medium}}$ and a size parameter $x = 2\pi r/\lambda$ with r the particle radius and λ the wavelength. The cross sections are given by:

$$\sigma_{ext} = \frac{2\pi r^2}{x^2} \sum_{j=1}^{\infty} (2j+1)(|a_j|^2 + |b_j|^2) \tag{2.7.1}$$

$$\sigma_{sca} = \frac{2\pi r^2}{x^2} \sum_{j=1}^{\infty} (2j+1)\,\mathrm{Re}(a_j + b_j) \tag{2.7.2}$$

$$\sigma_{abs} = \sigma_{ext} - \sigma_{sca} \tag{2.7.3}$$

and the coefficients a_j and b_j are given by:

$$a_j = \frac{m\psi_j(mx)\psi_j'(x) - \psi_j(x)\psi_j'(mx)}{m\psi_j(mx)\xi_j'(x) - \xi_j(x)\psi_j'(mx)} \tag{2.7.4}$$

$$b_j = \frac{\psi_j(mx)\psi_j'(x) - m\psi_j(x)\psi_j'(mx)}{\psi_j(mx)\xi_j'(x) - m\xi_j(x)\psi_j'(mx)} \tag{2.7.5}$$

Where ψ_j, ξ_j, ψ_j', ξ_j' are the Ricatti-Bessel functions and their derivatives [101, 102]. The absorption coefficient of the medium and the particles combined, α_{tot}, is given by:

$$\alpha_{tot} = \alpha_{medium} + \int N(r)\sigma_{ext}(r)dr \tag{2.7.6}$$

with α_{medium} the absorption coefficient of the medium, $N(r)$ the density of particles with radius r, and $\sigma_{ext}(r)$ the extinction cross section of particles with radius r.

In $SrTiO_3$, TEM investigations found nanometer sized voids (see chapter 8). These nanovoids are believed to be responsible for the yellow to brownish coloration of some STO crystals through Mie scattering. It is known that, for example, air bubbles in water can scatter light [103], since the scattering is caused by a sudden change in refractive index. However, the

classical Mie calculations were formulated for particles in an absorbing medium and do not always give correct results when the medium absorbs more than the scatterers. The classical Mie equations can predict a negative extinction coefficient if the extinction coefficient of the particles is smaller than that of the medium ($k_{particle} > k_{medium}$), which is unphysical [103]. Because of this, the Mie theory was expanded in the near field [104–107] and the far field approximation [108–111]. But, since in the case of nano-voids, the objects do not absorb at all, this problem can be resolved by simply setting the absorption contribution to the extinction coefficient to zero for all wavelengths. This gives:

$$\alpha_{tot} = \alpha_{medium} + \int N(r)\sigma_{sca}(r)dr. \tag{2.7.7}$$

The calculations are then performed using a numerical calculation script, in this case written in GNU Octave (see appendix A.2). This description assumes spherical particles or spherical nano-voids. Since the voids observed in the TEM images are somewhere between spherical and cubic, describing them as spheres is a reasonable simplification. The scattering center density is estimated from the TEM investigation and described with a lognormal distribution (see chapter 8). The complex refractive index of $SrTiO_3$ was taken from Ref. [1] and for the nano-voids $n' = 1$ and $k' = 0$ were used for all wavelengths.

3. Experimental details

3.1. Spectroscopy

3.1.1. Room temperature and low temperature spectroscopy

Room temperature spectra were measured using a Perkin-Elmer lambda 19 spectrometer, which can be used for wavelengths from the UV to the near IR range. The spectrometer is equipped with a point detector and scans through the wavelength range, giving a monochromatic sample illumination. The samples measured were polished chemo-mechanically on both sides except for the LHPG fibers which were too small and so were only polished mechanically. Thicknesses were typically between 0.5 and 1 mm. Low temperature spectra down to 4 K were measured using a liquid helium flow cryostat (Oxford Optistat CF ST).

By using small apertures it was possible to measure spectra of small samples or locally on bigger wafers. For small apertures or samples with a high absorption, the difference in intensity of the reference and sample beams is too large to accurately measure a transmission value. This is due to the signal levels then being too different for the processing electronics. To compensate this, a neutral density filter can be applied to the reference beam, which decreases the light throughput by a certain factor for all wavelengths.

To compensate for sample reflection and differences in sample thickness, the measured transmission value can be converted to the absorption coefficient, α, in cm^{-1}, using [98]:

$$\alpha = -\frac{1}{d} \ln \frac{\sqrt{(1-R)^4 + 4Tr^2R^2} - (1-R)^2}{2TrR^2} \tag{3.1.1}$$

Where R is the reflectivity, d is the sample thickness in cm and Tr is the transmission. R was calculated from the refractive index, n, using $(1-n)^2/(1+n)^2$. The refractive index data reported by Dodge [112] was used for the IR spectra while the refractive index data reported by Trepakov *et al.* [35] was used for the UV/VIS spectra because it is more accurate in this spectral range.

3.1.2. High temperature spectroscopy

The main problem with measuring absorption spectra of samples at high temperatures is that the sample and the furnace will glow. This thermal radiation will also reach the spectrometer and can cause the beam from the light source of the setup to be drowned out. This problem can be alleviated by increasing the distance between the furnace and the spectrometer and collimating the beam. With increasing distance, the amount of diffuse thermal radiation that reaches the detector will decrease [113]. The beam of the light source is collimated as much as possible, so a maximum of its intensity reached the spectrograph. This is why the beam is monochromated after it reaches the detector slit. Not doing so would mean that stray thermal radiation would be mistaken for a real signal at the current wavelength.

Another issue is that in a setup with a furnace and long optical paths it is difficult to incorporate a reference beam. Instead, Schwabe et al. measured the spectra for all temperatures twice, once with and once without the sample [113]. Since the position of the sample holder is not exactly fixed in the setup used here, the choice was made to use a reference spectrum from

the lambda 19 spectrometer. To convert the measured intensity, I, to transmission values, Tr, the following correction was applied:

$$Tr(T) = I(T)\frac{Tr_{\lambda 19}(RT)}{I(RT)} \tag{3.1.2}$$

with $Tr_{\lambda 19}(RT)$ the room temperature spectrum measured on the conventional lambda 19 spectrometer. These values can then be converted to absorption coefficient with equation 3.1.1. These calculations were done with the python scripts in appendix A.1.

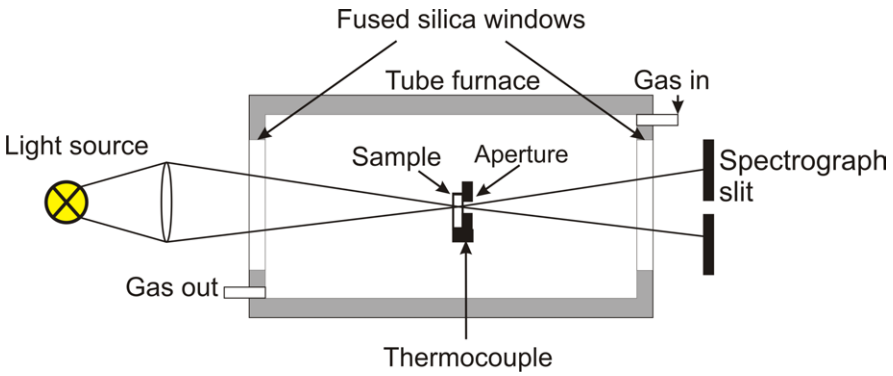

Figure 3.1.1.: High temperature spectroscopy setup. The sample can be heated to a maximum of about 1900 K. The light source and spectrometer can be adjusted to the desired wavelength range. (Taken from Ref. [114])

The high temperature IR and UV/VIS spectra were measured in the custom setup shown schematically in figure 3.1.1. The sample is mounted inside a tube furnace (Hesse Instruments HT-19), which can reach up to 2000 K, giving a maximum possible sample temperature of about 1900 K, though the maximum temperature used was 1673 or 1703 K. The spectra were measured every 50 K during heating (10 or 20 K/min) and cooling and averaged afterwards. This was done because the thermocouple is not mounted on the sample directly and lags slightly behind the sample temperature. If non-reversible changes in the spectrum of the sample were detected, the cooling spectra were evaluated and the transmission values were calculated using a reference spectrum acquired after the high temperature measurement. The sample compartment can be flushed with different gases to investigate atmospheric influences.

For different measurement series different light sources and spectrometers were used (see table 3.1.1). The light source was either an Energetiq EQ-99 LDLS laser driven xenon plasma source, which emits light at wavelengths from 170 nm to 2100 nm, or a high power halogen lamp with focusing optics. The plasma source has a small spot size, which makes it easy to collimate, and a high intensity in the UV/VIS range but is not very powerful in the NIR range. The halogen lamp has a higher intensity in the NIR, but is not as powerful in the UV, is harder to collimate and has a stronger wavelength dependence of the intensity in the UV/VIS range. For the UV/VIS measurements, an Oriel MS125 1/8 m grating spectrograph with a Si CCD detector was used, which was later replaced with a Princeton Instruments IsoPlane 320 SCT spectrograph with a 2D Si CCD detector. For the IR measurements, an Acton SpectraPro 2300i spectrograph with an InGaAs diode array was used. The settings for each measurement series are shown in table 3.1.1. For the IR measurements and series recorded with the IsoPlane spectrometer, dark spectra (with the light source covered) were measured and subtracted to further decrease the influence of the thermal radiation.

The setup was improved by replacing the Oriel spectrograph with the IsoPlane and incorporating a shutter that can be triggered by a PC. There are several advantages to the new

Table 3.1.1.: Measurement conditions for the different high temperature spectroscopy series. For the UV/VIS Re1 and MPD-Sc series an annealing effect was detected and so only the spectra measured during the cooling were converted and investigated further.

Series	**Section**	**Sample**	**Spectrometer**	**Light source**	**Wavelength (nm)**	**Maximum temperature and heating rate (K, K/min)**	**Holding time (min)**	**Atmosphere**
UV/VIS V1	4.1	Verneuil	Oriel	Xe plasma	280-930	1703, 20	10	Air
UV/VIS V2	4.1	Verneuil	Oriel	Xe plasma	280-930	1703, 20	10	N_2 flow
IR V1	4.2	Verneuil	SpectraPro	Xe plasma	1030-1560	1673, 20	10	Air
UV/VIS Re1	4.3	TSSG Re1	Oriel	Halogen	350-1000	1673, 20	10	N_2 flow
UV/VIS Ox4	4.3	TSSG Ox4	Oriel	Halogen	350-1000	1673, 20	10	Ar + 2.83 vol% O_2 flow
UV/VIS MPD-Sc	5	MPD-Sc1	IsoPlane	Halogen	375-900	1665, 10	10	Air
UV/VIS V 3	5	Verneuil	IsoPlane	Halogen	375-900	1665, 10	10	Air
IR MPD-Sc	5	MPD-Sc1	SpectraPro	Halogen	1110-1640	1665, 20	20	Air
IR V2	5	Verneuil	SpectraPro	Halogen	1110-1640	1665, 20	20	Air

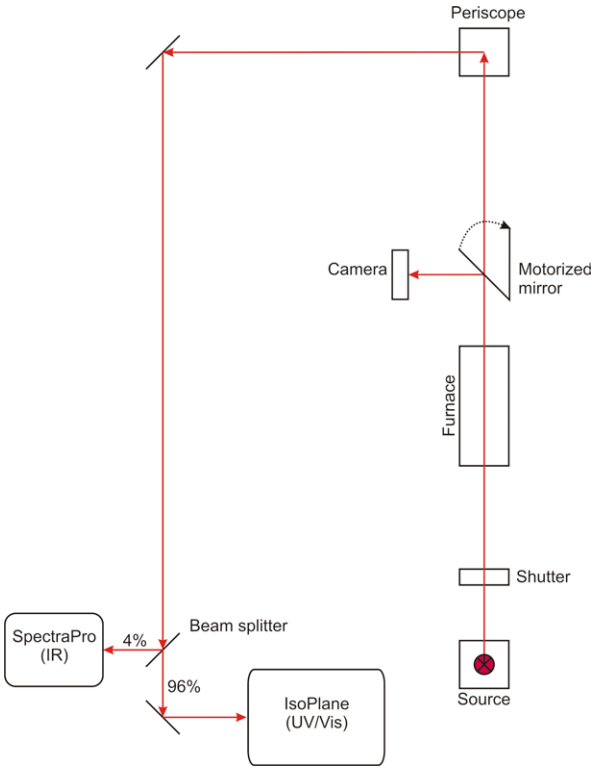

Figure 3.1.2.: Proposed enhanced high temperature spectrometry setup.

spectrometer: it has a higher spectral resolution, less internal stray light, is very well suited to imaging spectroscopy and can be controlled from LabView. The big advantage of controlling the spectrometer from LabView is that it is possible to integrate control of other hardware, like the thermo controller and the shutter, and advanced triggering of the spectrometer becomes possible. For example, it is fairly easy to have the LabView program close the shutter, record a dark spectrum, open the shutter, record a sample spectrum and then subtract the dark spectrum. Another example of the extended functionality is to record spectra at fixed time intervals on a heating curve to perform kinetic measurements on annealing processes. With the 2D detector it is now also possible to measure different areas of multicolored samples at the same time. The setup could be further enhanced by adding a beam splitter, which would make it possible to measure both IR and UV/VIS spectra at the same time by dividing the beam between two spectrometers (see Fig. 3.1.2). Adding a flip mounted mirror and a camera would enable direct sample monitoring without disturbing the optical path. So far, the integration of the shutter and the new spectrometer has been realized and tested.

3.2. Other characterization methods

3.2.1. Temperature dependent thermal conductivity

To accurately measure the temperature dependence of the thermal conductivity, Differential Scanning Calorimetry (DSC) measurements were performed first [30]. The sample was Verneuil grown $SrTiO_3$ and the measurements were performed in platinum crucibles using a NETZSCH DSC 401 F1 calorimeter in an argon atmosphere to determine the specific heat capacity (c_p). The samples were heated to 1873 K using a heating rate of 20 K min^{-1}. The densities (ρ) of samples prepared from the Verneuil material and two TSSG crystals grown

below 2013 K (crystals Ox4 and Re3 from Ref. [30]) were determined by Archimedes' principle (buoyancy method). Linear thermal expansion of a {100} Verneuil cuboid (sample dimensions: 5 mm × 5 mm × 10 mm) was measured up to temperatures exceeding 1873 K using a horizontal push-rod dilatometer (DIL 402 C, NETZSCH) in a helium atmosphere and a heating rate of 5 K min^{-1}. Temperature dependent values for thermal diffusivity (a) were determined using the high temperature laser-flash analysis (LFA) method. The experiment was performed in an argon atmosphere and with temperatures of up to 1973 K [30]. The sample was covered with graphite prior to the measurements. The temperature dependent values of c_p, ρ and a, determined by DSC, buoyancy method, dilatometry and LFA (measured by NETZSCH-Gerätebau GmbH), were used to calculate the temperature dependent thermal conductivity (κ) according to:

$$\kappa(T) = \rho(T) \times c_p(T) \times a(T) \tag{3.2.1}$$

3.2.2. Transmission electron microscopy

Transmission electron microscopy (TEM) investigations on TSSG and LHPG samples were performed with an aberration corrected FEI Titan 80-300 operated at 300 kV. For high resolution TEM (HRTEM) imaging we tuned the spherical aberration to a slight negative value of $C_s = -10$ μm (determined by analysis of Zemlin tableaus [115]) and used a small over-focus. All other aberrations were corrected to minimum. For thin samples (thickness typically below 5 nm) this results in bright atom contrast and even weakly scattering oxygen atomic columns can be directly imaged [116, 117].

Scanning TEM high angle annular dark field imaging (STEM-HAADF), also known as STEM Z-contrast, was performed with a semi-convergence angle of the incident electron probe of 9 mrad, giving a spatial resolution of about 0.13 nm, and a semi-acceptance angle of the annular dark field detector (Model 3000, Fishione Instruments) of 35 mrad. Samples for TEM investigation were prepared to electron transparency solely by wedge polishing [118] in order to avoid possible ion-milling induced formation of voids or particles in the sample.

3.2.3. Inductively coupled plasma optical emission spectroscopy

Chemical elemental analysis was carried out using an inductively coupled plasma optical emission spectrometer (ICP-OES) (IRIS Intrepid HR Duo, Thermo Fisher Scientific, USA). The samples were ball-milled (MM-2, Retsch GmbH, Germany) and analyzed after microwave digestion (ETHOS plus, MLS GmbH, Germany) in a mixture of nitric and hydrofluoric acid at 493 K. The spectrometer was calibrated with synthetic solution standards. To ensure high accuracy, the sample matrix matched the matrix of the calibration standard. The Sr and Ti concentrations were measured directly and the oxygen concentration was determined by assuming it makes up the rest of the sample weight (taking into account the concentration of any other elements measured).

3.2.4. Energy dispersive Laue mapping

Energy dispersive Laue mapping (EDLM) is a new non-destructive qualitative characterization technique to identify low-angle grain boundaries in single crystals [119]. The method uses a spatially resolved micro X-ray fluorescent device which can scan a sample with a 25 μm resolution. The crystal only needs to be planarized on one side and can otherwise have almost any geometry. The resolution is limited by the spot size of the focused X-ray beam. The radiation of the excitation source interacts with the sample, ejecting electrons from the

inner shells of the atoms, which is followed by electrons from the outer shells "falling" to the inner shells while emitting a photon. If the sample is crystalline, Bragg reflections will be detected as well, which are found at specific energies. This can be seen from Bragg's law [120]:

$$2d\sin(\theta) = n\lambda \tag{3.2.2}$$

where d is the spacing between two crystal planes, θ is the angle of incidence, n is a positive integer and λ is the wavelength. So, when the wavelength is right for a certain spacing, a Bragg reflection will reach the detector. Since different grains in the crystal have a slightly different orientation, the Bragg reflexes will be recorded for different energies. This way, subgrain misorientations in $SrTiO_3$ down to between 40 and 100" can reliably be identified and displayed in a two dimensional diffraction intensity map [119].

The EDLM map of MPD-Sc-A was measured using a M4 Tornado (Bruker) μ-XRF spectrometer. The spectrometer was equipped with an Rh X-ray source operated at 50 kV and 600 mA and a circular silicon drift detector with a high energy resolution of $<$145 eV. The measurement time for each point was 20 ms and the mapping was performed 4 times and averaged.

4. Temperature dependent optical absorption and heat conduction

In this chapter, the optical absorption and heat transport of strontium titanate are discussed for temperatures from 4 K to 2350 K, through measurements and extrapolations. These properties determine the heat transport through the crystal and those that the stability of the crystal growth. These findings give information to determine which growth methods are more likely to be effective for $SrTiO_3$ and whether this is determined by intrinsic material properties or other factors. The main mode of heat transport near the melting point of STO (2350 K) is radiative, so the optical absorption, especially in the infrared, is very important. The optical absorption is increased by the shrinking of the band gap, which allows more absorption by band-to-band excitation of electrons and results in a larger intrinsic free carrier concentration through thermal excitation. Free carriers can of course also be generated by dopants or charged vacancies. Free carriers absorb light in the infrared and therefore can have a large impact on the radiative heat transport, as it has already been demonstrated for the transparent semiconducting oxide β-Ga_2O_3 grown by the Czochralski method [121]. Although its effect on the overall heat transport through the crystal is not as strong at growth temperatures, the heat conduction of $SrTiO_3$ has also been determined for temperatures up to 1700 K.

The band gap temperature dependence and high temperature infrared absorption parts of this chapter are largely based on an article that the author published in Physica Status Solidi A (Ref. [114]). The high temperature spectra of the TSSG crystals and the thermal conductivity were part of a paper in CrystEngComm (Ref. [30]) where I was a co-author.

4.1. Temperature dependence of the band gap

Strontium titanate has an indirect band gap of 3.2 eV at room temperature [1], which decreases with increasing temperature [122–124]. Bieger et al. [123] studied the absorption edge of STO from 10 K to 700 K during their study of oxygen uptake kinetics in this material. Goldschmidt and Tuller [122] studied the nature of the band transition (direct or indirect) and the Urbach broadening of the absorption edge from room temperature to 1473 K. The shrinkage of the band gap with rising temperature shifts the fundamental interband absorption to longer wavelengths and thereby increases the number of intrinsic free carriers that are thermally exited over the band gap.

To determine the temperature dependent band gap energy, UV/VIS spectra were measured from 4 K to 1703 K. From these spectra the band gap energies were extracted, fitted and extrapolated. For these experiments, two undoped Verneuil grown crystals were used (provided and polished by CrysTec GmbH). The samples had sizes of $5 \times 5 \times 0.5$ mm^3 and $5 \times 5 \times 0.18$ mm^3 and they were colorless and electrically insulating at room temperature.

The spectral dependencies of the absorption coefficient of STO for low and high temperatures are shown in figure 4.1.1(a) and (b), respectively. The temperature ramp for the high temperature UV/VIS spectra was measured twice, once with the sample chamber flushed with N_2 and once with the sample in ambient atmosphere to investigate atmospheric effects. The

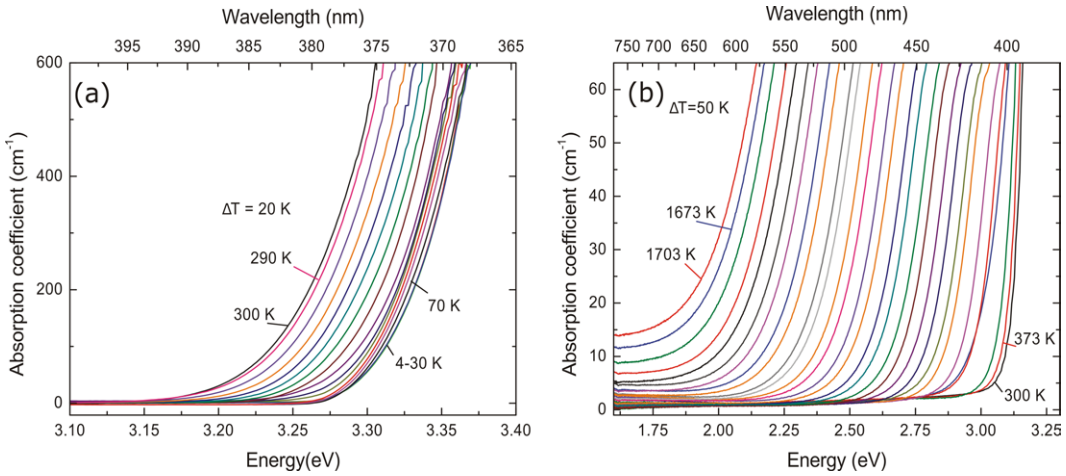

Figure 4.1.1.: (a) Absorption coefficients for temperatures from 4 K up to room temperature in helium and (b) from room temperature up to 1703 K in nitrogen. (Taken from Ref. [114])

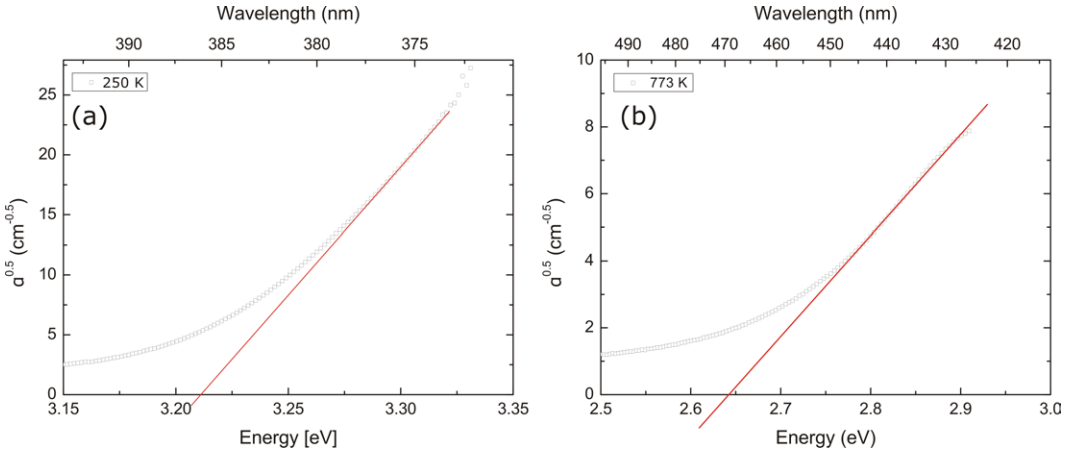

Figure 4.1.2.: Examples of the band gap determination. The extrapolation of the linear part of the $\sqrt{\alpha}$ versus E curve to $\sqrt{\alpha} = 0$ yields $\sim E_g + E_{ph}$ at low temperatures, (a), and $\sim E_g - E_{ph}$ at high temperatures, (b), respectively. (Taken from Ref. [114])

sample showed no sign of coloration in either case. Furthermore, no differences larger than the experimental errors in determining the absorption coefficients could be observed between both runs.

Since STO has an indirect band gap [1], the absorption coefficient, α, around the band gap energy is given by:

$$\alpha \propto (h\nu - E_g \pm E_{ph})^2 \tag{4.1.1}$$

with $h\nu$ the photon energy, E_g the band gap energy and E_{ph} the phonon energy (see Ref. [99] and section 2.6.2). From this equation it follows that a plot of $\sqrt{\alpha}$ versus the photon energy should show, under ideal conditions, two linear parts around the band gap. Extrapolations of these linear parts to $\sqrt{\alpha} = 0$ should result in $E_g + E_{ph}$ and $E_g - E_{ph}$ for emission and absorption of the momentum conserving phonon, respectively (explained in more detail in section 2.6.2). Because the phonon occupation numbers are low at low temperatures, photon absorption is predominantly accompanied by phonon emission. Therefore it is assumed here

that the plots of $\sqrt{\alpha}$ vs. $h\nu$ for the measurements below room temperature are dominated by the linear part that belongs to phonon emission and the extrapolation yields $E_g + E_{ph}$. A typical example is shown in figure 4.1.2 (a). For the evaluation of the absorption measurements above room temperature, on the other hand, it is expected that phonon absorption plays a more important role. Furthermore, these measurements were limited to absorption coefficients below 65 cm^{-1}, mainly due to stray light problems (while the low temperature measurements could be accurately performed up to 600 cm^{-1}). The consequence is that the absorption onset can only be assessed in the region of low photon energies, where phonon absorption should prevail. Therefore the extrapolation (see typical example in Fig. 4.1.2(b)) yields a value near $E_g - E_{ph}$ and one expects a discontinuity of about $2E_{ph}$ in the extrapolated energies between the low and the high temperature data. Indeed, such a discontinuity is observed and can be removed by adding 0.12 eV to the energy values extrapolated from the high temperature data. Since E_{ph} is found to be ~ 60 meV in the fit of the temperature dependence of the band gap (see section 4.1.1), amount and sign of this correction are justified by the preceding considerations (it should be mentioned however, that the correction may also contain systematic experimental uncertainties arising from the combination of measurements performed on two different spectrometers using samples of different thickness). Figure 4.1.3 shows the band gap energies determined by the described extrapolation procedure for the whole temperature range from 4 K to 1703 K, including the correction for the high temperature data. The energy values actually represent $E_g + E_{ph}$. While this difference is important for the below room temperature data, it becomes negligible at elevated temperatures because of the lower accuracy of the corresponding measurements and extrapolations. (The random error of the energy value at 373 K is estimated to be ± 0.05 eV and increases to ± 0.1 eV at 1703 K.)

4.1.1. Extrapolation

The observed temperature dependence of the absorption edge can be well described by a single-phonon model that can be analytically expressed by [125, 126]:

$$E_g(T) = E_g(0) - S\langle\hbar\omega\rangle \left(\coth\left(\frac{\langle\hbar\omega\rangle}{2kT}\right) - 1 \right) \tag{4.1.2}$$

where $E_g(0)$ is the band gap energy at 0 K, S is a dimensionless measure of the electron–phonon coupling strength, and $\langle\hbar\omega\rangle$ is an average of the contributing phonon energies. This equation reflects both sources of the band gap temperature dependence: lattice expansion and electron-phonon interaction. Both of them have nearly the same analytical temperature dependence [125, 126]. The best-fit parameters found are $E_g(0) = 3.268$, $S = 5.6$ and $\langle\hbar\omega\rangle = 60$ meV for the measurements in air and $E_g(0) = 3.265$, $S = 6.1$ and $\langle\hbar\omega\rangle = 66$ meV for the measurements in N_2 flow respectively. The fit curves, represented in figure 4.1.3, deviate less than the estimated experimental error, indicating that the atmospheres do not have a significant effect on the shift of the absorption edge. On average $E_g(0) = 3.266$, $S = 5.9$ and $\langle\hbar\omega\rangle = 63$ meV are found. The average phonon energy is in the energy range of the optical phonon modes reported by Balachandran and Eror [127]. When extrapolated to the melting point (2350 K), a band gap of 1.2 ± 0.1 eV is found.

The temperature dependence of the absorption edge is rather strong in STO, though not as strong as in In_2O_3 [128]. In both cases the strong dependence seems to be the result of a large electron–phonon coupling (for In_2O_3 $S = 8.24$). Both the coupling and the temperature dependence are much stronger than found in, for example, Si, GaAs, GaP or diamond (which have S-values of 1.49, 3.00, 3.35 and 2.31, respectively [125]).

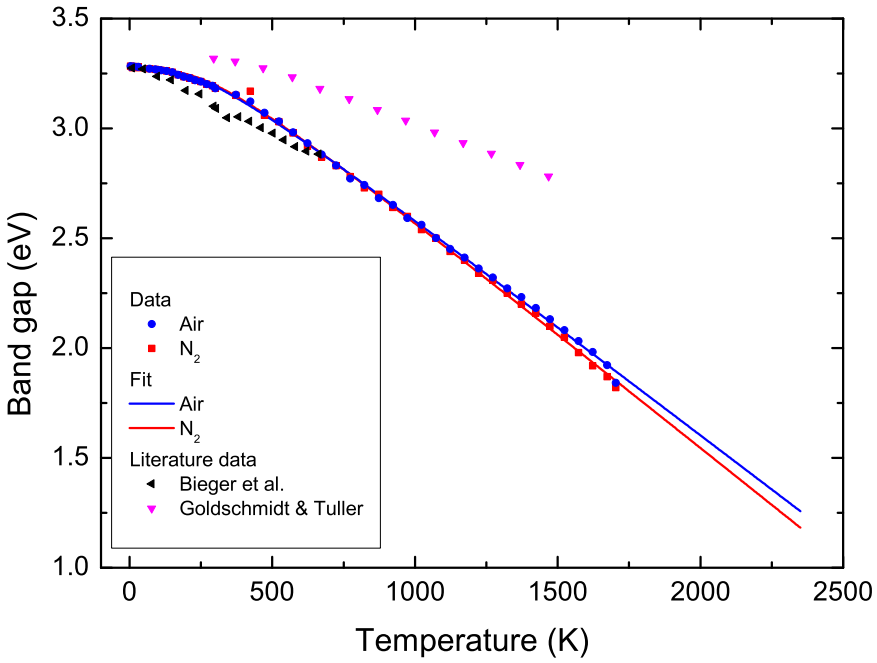

Figure 4.1.3.: Band gap energies for the low and high temperature measurements. The energies were fitted and extrapolated to 2350 K. The values found here are compared with data from Bieger et al. [123] and Goldschmidt and Tuller [122] (G&T). The data from Goldschmidt and Tuller differs quantitatively when different absorption coefficient values are used for $E_\alpha(T) = E_g(T)$, but is qualitatively very similar. Here the data for $\alpha = 2000$ cm^{-1} is shown. (Taken from Ref. [114])

The absorption edge energies found by Goldschmidt and Tuller [122] at higher temperatures are significantly larger than ours (see Fig. 4.1.3). In contrast, the measured spectra are very similar (see Fig. 4.1.4). Goldschmidt and Tuller determined the band gap by taking the energy at which a certain absorption coefficient value is reached (this leads to a certain degree of arbitrariness in the determined band gap). This is common practice in amorphous semiconductors and also explains why their values were much higher. When this method is applied to our measurements, similar values were found. When the energy at $\alpha = 40$ cm^{-1} was taken in the spectra measured by Goldschmidt and Tuller, values very close to the ones presented here were found. The method used here is preferable for single crystals since it is based on the physical description of band to band absorption in an indirect semiconductor [99].

Goldschmidt and Tuller also discussed the effect of Urbach tailing on the temperature dependence of the absorption edge in $SrTiO_3$ in some detail [122]. The Urbach tail broadens the low energy side of the absorption edge. It is caused by an exponential tail of the density of states that extends into the forbidden gap and is caused by disorder in the material or local electric fields like those caused by charged point defects [129–131]. Here it was assumed that this effect is not really noticeable for $\alpha \gtrsim 10$ cm^{-1} in a single crystalline material. Therefore it was largely ignored in the present work.

Bieger et al. [123] found $E_g(T)$ values similar to those presented here. Their values are fairly close to ours, within the estimated combined measurement and analysis error in the 10–700 K range reported in that publication (assuming their method introduces an error of 50 meV or larger, see Fig. 4.1.3).

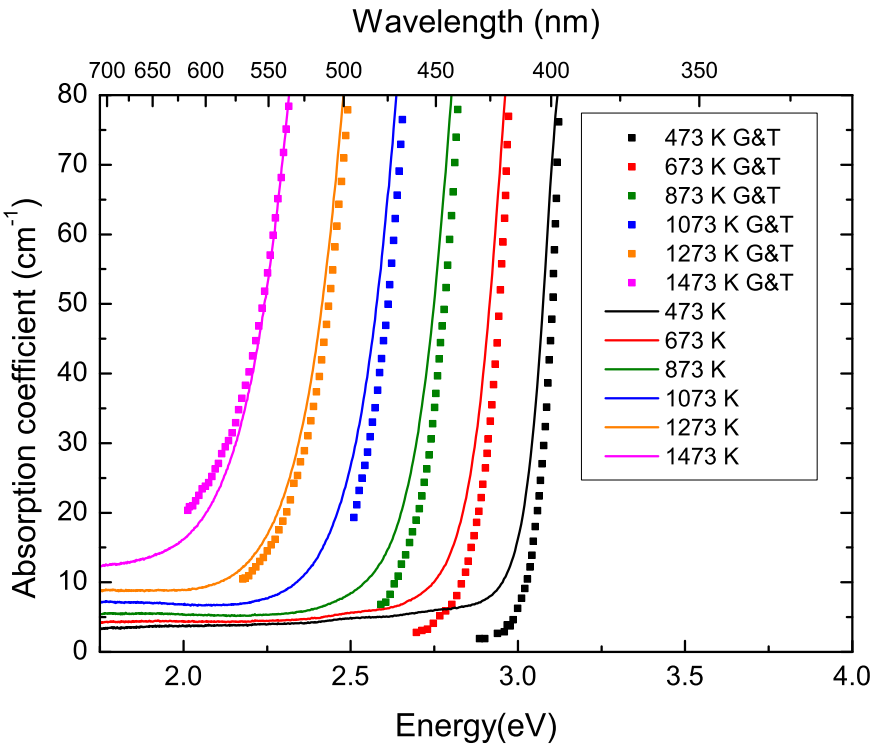

Figure 4.1.4.: Comparison of some of the spectra measured by Goldschmidt and Tuller [122] (G&T) with the spectra measured here. (Taken from Ref. [114])

4.1.2. Direct absorption

The large shrinkage of the band gap will influence the radiative heat transport through a growing crystal by increasing the fundamental band to band absorption and by increasing the number of intrinsic free carriers which absorb in the IR (as discussed in section 4.2). As can be seen from figure 4.1.5, the wavelength of maximum black body emission and the band gap energy of $SrTiO_3$ approach each other as the temperature rises, increasing the possible fundamental energy absorption. The amount of energy available for fundamental absorption over the band gap can be calculated from the band gap at a given temperature and the black body energy density formula form of Planck's law:

$$U(\lambda, T) = \frac{8\pi hc}{\lambda^5} \times \frac{1}{\exp\left(\frac{hc}{\lambda k_B T}\right) - 1} \tag{4.1.3}$$

With U the spectral energy density in Wm^{-3}, h Plancks constant, c the speed of light in vacuum, λ the wavelength in m, k_B the Boltzmann constant and T the temperature in K[132]. The energy density was then integrated from 1 nm to the wavelength corresponding to the band gap at temperature T (see Figs. 4.1.6 and 4.1.7).

At the melting point (2350 K), the total energy of all photons with an energy higher than the band gap is about 3.4×10^{-3} J/m^3, which is 14.5% of the total radiated energy. If the crystal is not grown from the melt but from self flux with slow cooling, it is possible to grow a straight cylinder below 1808 K or 2013 K [30, 31]. In this case, the energy of photons absorbable by excitation over the band gap is 2.8×10^{-5} J/m^3, which is about 0.35% of the total black body emission and about 121 times less than the absorbable energy at 2350 K. Other TSSG crystals were grown at 2013 K where the absorbable energy is 2.45×10^{-4} Jm^{-3},

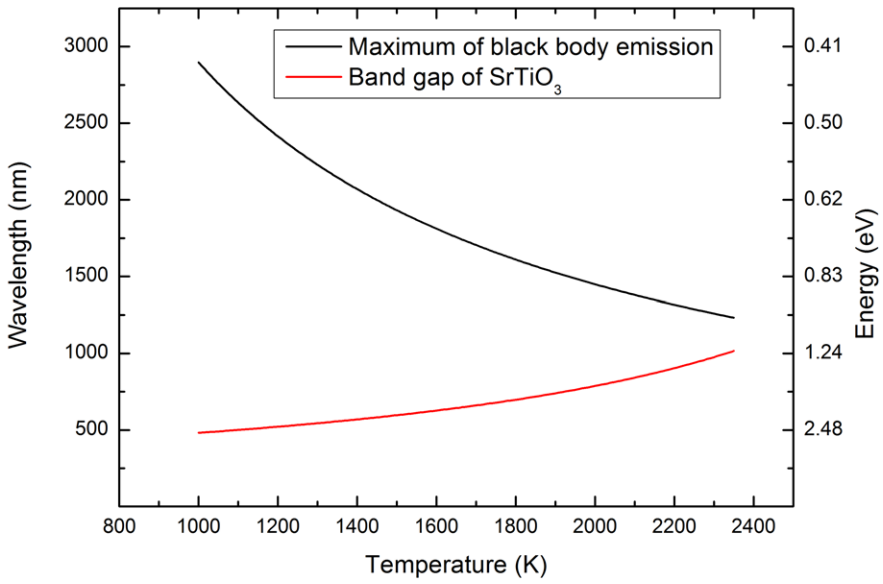

Figure 4.1.5.: Comparison of wavelength of maximum emission with the temperature dependent band gap of $SrTiO_3$.

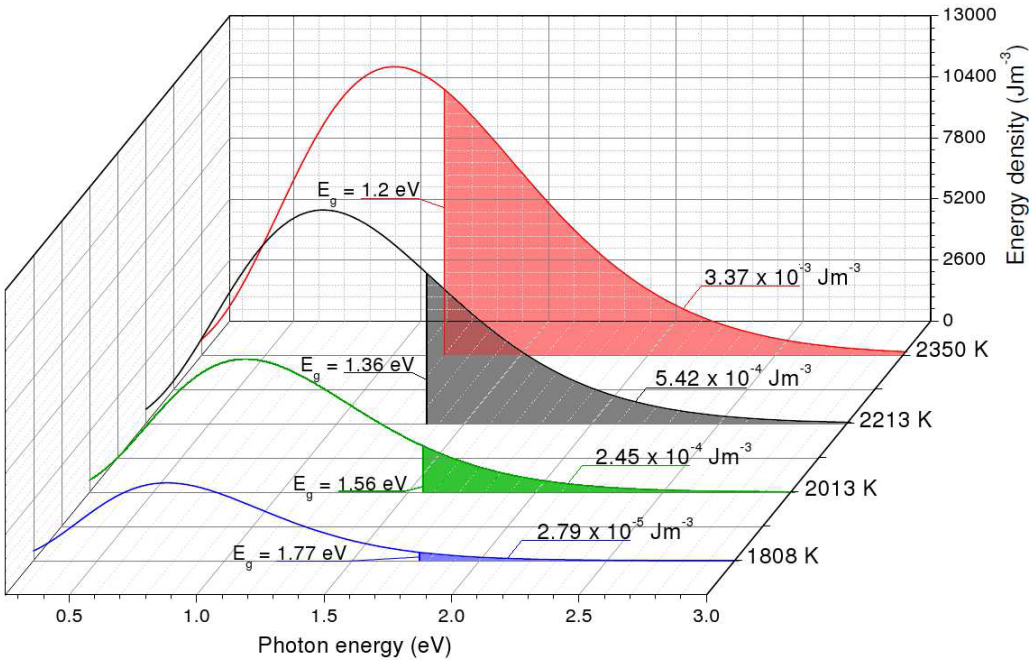

Figure 4.1.6.: Black body radiation energy density. The colored areas correspond to the amount of energy available for absorption by excitation across the band gap. The absorbable energy is about 121 times higher at 2350 K than at 1808 K. (Taken from Ref. [114])

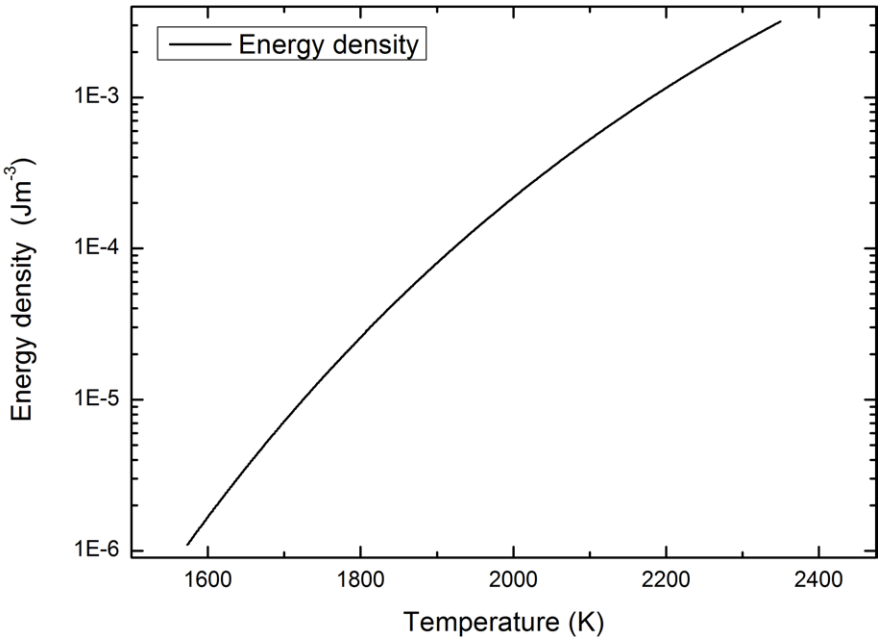

Figure 4.1.7.: Integrated energy density of black body radiation for photons with an energy larger than the band gap. (Taken from Ref. [63])

which is about 14 times smaller than at 2350 K. This difference and the lower IR absorption apparently allows stable growth and improved crystal quality [30, 31].

4.2. High temperature infrared absorption

Since STO has a very high melting point (2350 K), heat transport through a growing crystal will be mostly radiative. This means that the optical absorption in the infrared wavelength range at growth temperatures is very important. STO is transparent in most of the IR range at room temperature, but at higher temperature this can change because of free charge carriers which could be caused by impurities, point defects forming at high temperatures (especially oxygen vacancies) and thermal excitation over the band gap. To investigate the high temperature IR absorption of $SrTiO_3$, spectra were measured for a Verneuil grown wafer 0.5 mm thick (provided and polished by CrysTech GmbH, the same sample as used for the high temperature UV/VIS measurements). The high temperature spectrometry set up was used in the configuration discussed in section 3.1.2, where the spectrometer was an Acton SpectraPro 2300i spectrograph with an InGaAs diode array.

The relative transmission is shown in figure 4.2.2 a) shows that the IR absorption increases significantly above 1373 K. At 1673 K, the transmission is only about half of the room temperature value. This indicates that almost all IR radiation in this wavelength range will be absorbed at the melting point (2350 K). The spectra with significant absorption values are shown in figure 4.2.1. The spectra show no clear peaks, but rather a continuous rise with the wavelength, which indicates that the absorption is caused by free carriers and not by, for example, impurities.

One source of the free carriers could be the formation of oxygen vacancies. Moos et al. set up a model from extensive temperature dependent conductivity measurements to calculate the number of free electrons, holes, oxygen and strontium vacancies, and ionized acceptors between 1273 K and 1753 K [124]. They included a linear temperature band gap dependence,

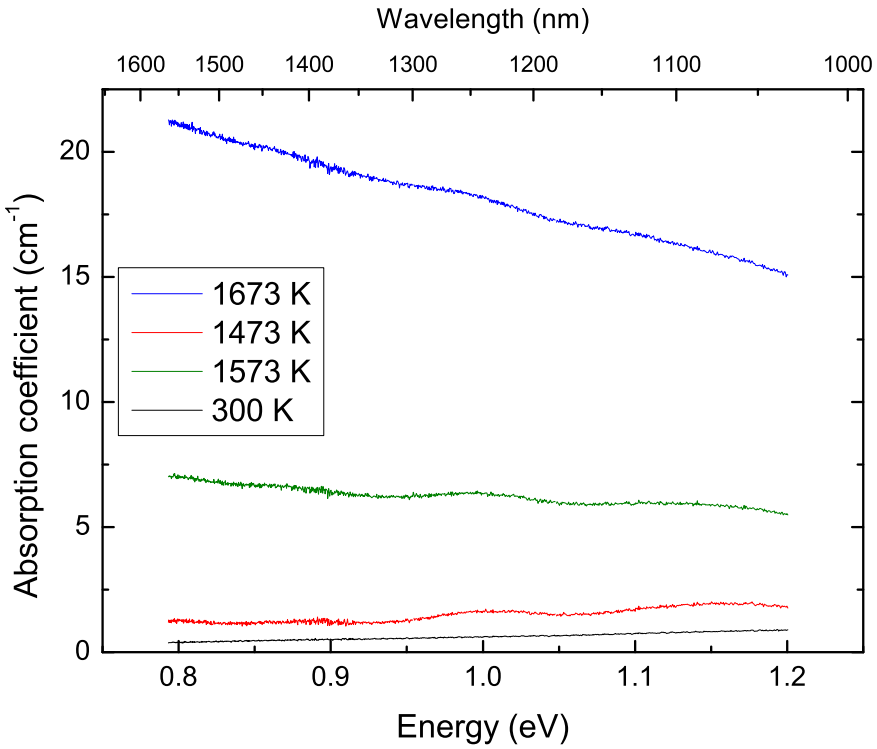

Figure 4.2.1.: Infrared absorption spectra. Above 1400 K the absorption coefficient starts to rise rapidly and exhibits a monotonic increase with wavelength at the higher temperatures. This behavior suggests free carrier absorption. (Taken from Ref. [114])

which is very similar to that reported by Bieger et al. [123] and comparable to the values shown in the previous section. For 1723 K and ambient air, they calculated an oxygen vacancy concentration of about 5×10^{18} cm^{-3} and a total free carrier density of about 10^{18} cm^{-3}. For our measurements in nitrogen flow, we estimate that about 1% of the atmosphere in the furnace is ambient air. That gives us an oxygen partial pressure of about 2 mbar and according to the model of Moos et al. a free carrier concentration in the 10^{18} cm^{-3} range. The difference between the two atmospheres, according to that model, is that at in the ambient atmosphere the predominant carriers are holes while under N_2 flow electrons are the dominant carriers.

Another source could be the excitation of intrinsic charge carriers. Using the obtained function for the absorption edge energies as $E_g(T)$, it is possible to estimate the intrinsic free carrier densities in the absence of electrically active defects. For an intrinsic semiconductor with spherical parabolic energy bands at thermal equilibrium [133]:

$$n_i = p_i = 2\left(\frac{k_B T}{2\pi\hbar^2}\right)^{3/2} (m_n m_p)^{3/4} \exp\left(\frac{-E_g}{2k_B T}\right) \tag{4.2.1}$$

where n_i and p_i are the intrinsic concentrations of electrons and holes, respectively and m_n and m_p are the effective electron and hole masses. To estimate the free carrier concentration, the effective carrier masses are taken to be the electron rest mass, m_0. Marques et al. [134] report that the density of states effective mass values depend on the direction of the transition in k-space (whether it is for example a $\Gamma \rightarrow R$ or a $\Gamma \rightarrow X$ transition), but that they lie close to 1 m_0. The calculated carrier densities are shown in figure 4.2.3. As can be seen, the predicted density at 1750 K is about 10^{18} cm^{-3}, similar to the model of Moos et al. [124].

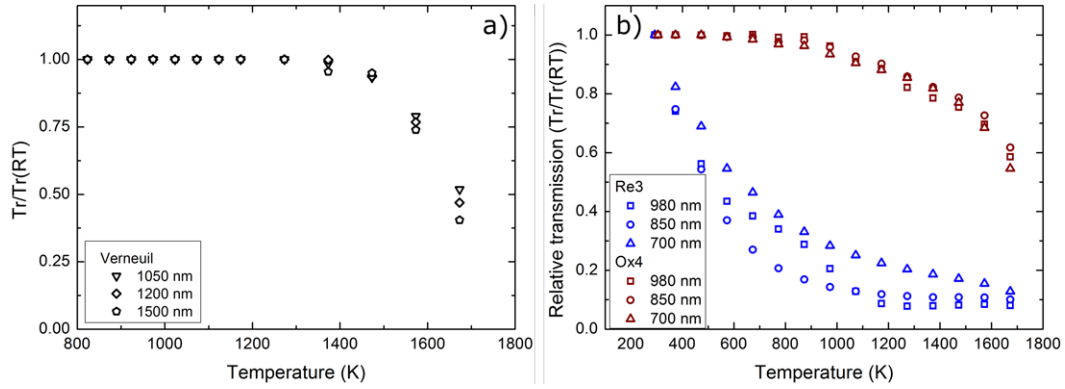

Figure 4.2.2.: Relative transmission, normalized to the room temperature transmission, for a) the Verneuil sample and b) the TSSG samples Re3 and Ox4. (After Refs. [30, 114])

The predicted carrier density rises to $n_i + p_i \approx 10^{19}$ free carriers per cm^3 in total at the melting point.

The estimated carrier concentrations for intrinsic carriers and the formation of vacancies are very similar. The formation energy of charged oxygen vacancies has been reported to depend on the temperature, the oxygen chemical potential and the Fermi level [94, 135, 136]. Since this makes predicting a vacancy concentration rather difficult, only the intrinsic free carriers have been used to predict the IR absorption above the measured temperature range. The free carrier absorption coefficient can be calculated using [98]:

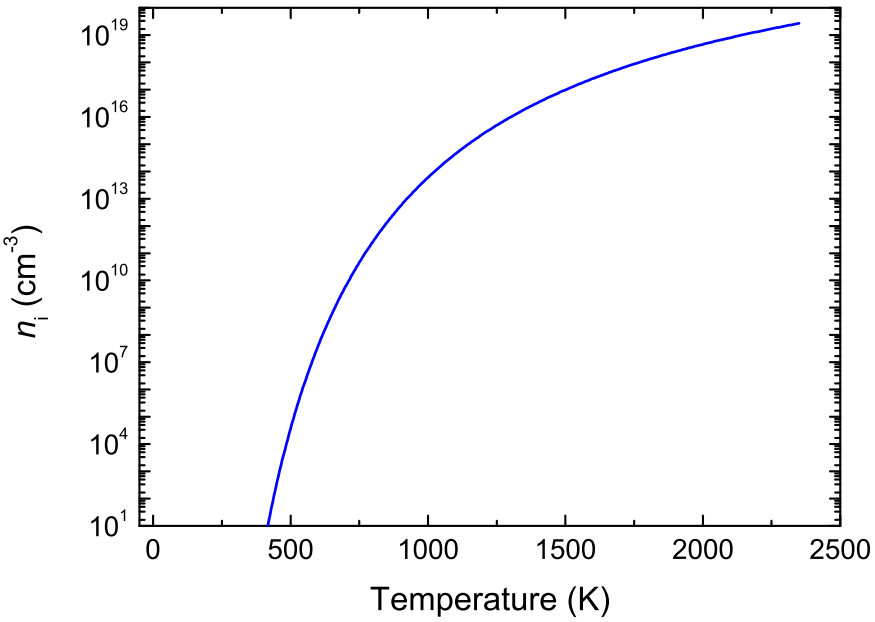

Figure 4.2.3.: Intrinsic free carrier densities in $SrTiO_3$ calculated from the $E_g(T)$ data. (Taken from Ref. [114])

$$\alpha_{fc} = \frac{\lambda^2 q^3}{4\pi^2 c^3 n(\lambda)\epsilon_0}\left(\frac{n_i(T)}{m_n^2\mu_n} + \frac{p_i(T)}{m_p^2\mu_p}\right) \tag{4.2.2}$$

where λ is the wavelength, q is the elementary charge, c is the speed of light, $n(\lambda)$ is the

refractive index, ϵ_0 is the static electric constant, $n_i(T)$ and $p_i(T)$ are the intrinsic free electron and hole concentrations, and μ_n and μ_p are the electron and hole mobilities respectively. Electron mobility values have been determined up to 1373 K by Moos et al. [137], but the only available hole mobility values at high temperatures (up to 1273 K) were measured for highly iron-doped crystals (0.37 mol Fe/mol STO [138]). With such high dopant concentrations, the mobility values will not match those of an undoped crystal. The effective masses are known to change with the temperature [139], but for the temperature range relevant here, no values have been reported. Also, the density of states masses, like those calculated by Marques et al., do not equal the optical mass for materials with a non-parabolic band structure such as STO [140].

Because of these uncertainties, equations 4.2.1 and 4.2.2 were combined with $m_n = m_p = m^*$ and $\mu_n = \mu_p = \mu_{av}$. This gives:

$$\alpha_{fc} = \frac{q^3 \left(\frac{k_B}{2\pi\hbar^2}\right)^{3/2}}{\pi^2 c^3 \epsilon_0 \sqrt{m_0}} \times \frac{\lambda^2}{n(\lambda)} \times \frac{T^{3/2} \exp \frac{-E_g(T)}{2k_B T}}{\sqrt{m^*/m_0}\mu_{av}} \tag{4.2.3}$$

The main temperature dependence is given by the shrinking of the band gap rather than the temperature dependence of $\sqrt{m^*/m_0}\mu_{av}$, which also is unknown. For this reason, $\sqrt{m^*/m_0}\mu_{av}$ was taken as a fit constant to adjust the prediction of the free carrier absorption to the measured data (see Fig. 4.2.4). A good match was found for $\sqrt{m^*/m_0}\mu_{av} = 1.5\,\mathrm{cm^2V^{-1}s^{-1}}$, which is a reasonable value since the room temperature mobility of $SrTiO_3$ is around 5 $\mathrm{cm^2V^{-1}s^{-1}}$ at room temperature, independent of the carrier concentration [137].

The dependence of α_{fc} on λ^2 is apparently not quite correct (see also Fig. 4.2.1). In effect, the dependence is weaker. Several different scattering mechanisms can be involved in free carrier absorption. Scattering by acoustic phonons, with a $\lambda^{3/2}$ dependence, comes closest to our data [141, 142] which may be expected for such high temperatures. For a more accurate investigation of this scattering mechanism a larger wavelength range has to be considered.

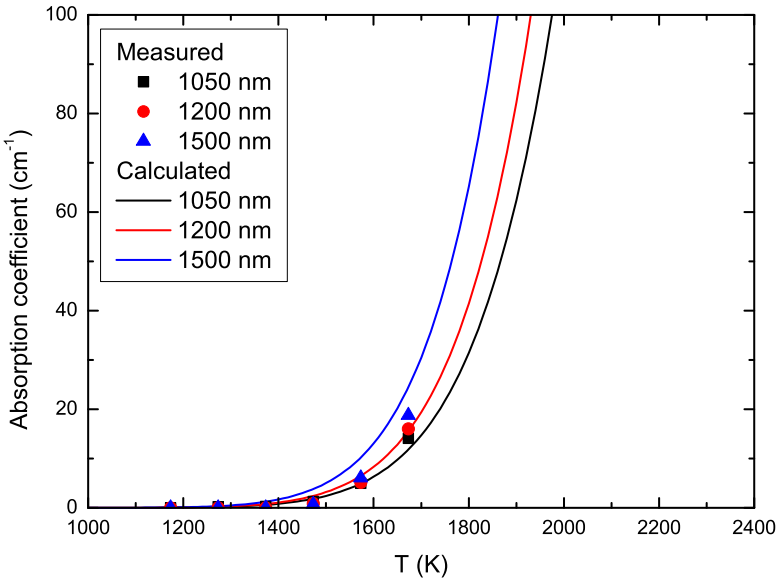

Figure 4.2.4.: Comparison of the calculated and measured absorption coefficients. (Taken from Ref. [114])

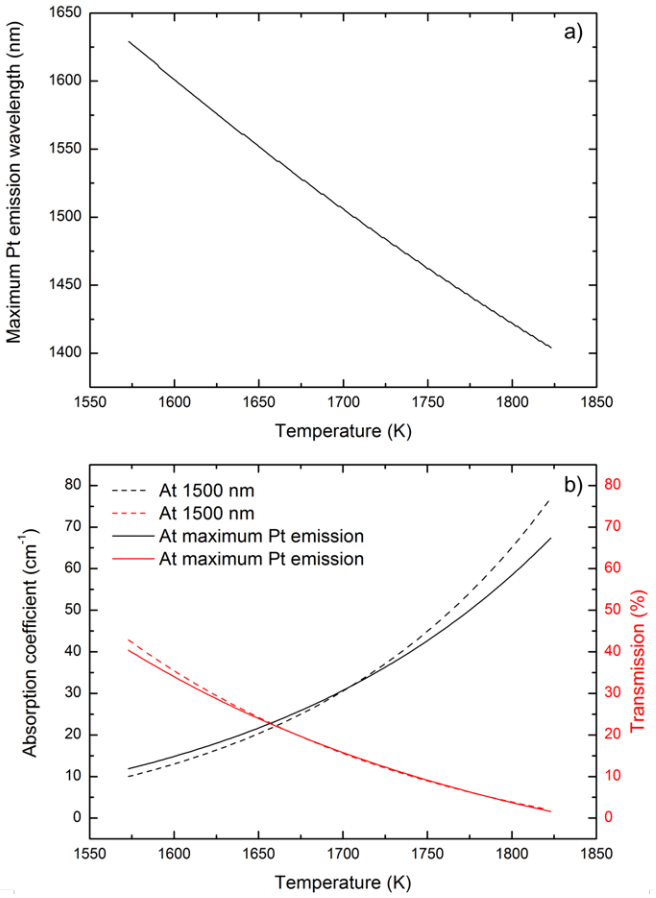

Figure 4.2.5.: a) Wavelength of maximum emission of Pt at different temperatures. Determined by multiplying the black body emissivity curve for that temperature with the 1600 K emission spectrum of Pt reported in Ref. [143]. b) Estimated absorption coefficient at 1500 nm and at the wavelength of the maximum emission of Pt (see Fig. [fig:Wavelength-Pt-maximum]). (Images from [63]).

Using these approximations, it is possible to estimate the radiative heat transport at relevant growth temperatures for the TSSG growth below 1808 K [63]. Since the metal parts of the setup are made of platinum in those growth runs, the black body spectrum was multiplied by the emissivity data for Pt reported by De Sousa Meneses et al. [143], who reported the emissivity up to 1600 K. The values for 1600 K were used in all calculations in the 1573-1823 K range discussed here since the emissivity of Pt changes little over the range reported in Ref [143]. This range roughly corresponds to the temperatures measured along a growing crystal in such a growth experiment.

With the fits of the IR absorption determined above, spectra were estimated for the relevant temperature range [63]. From these spectra the absorption coefficients and transmission values were taken for the wavelength of maximum emission of Pt and for 1500 nm (see Figs. 4.2.5 a) and b). The transmission values were calculated for a sample of 0.5 mm thickness. At 1823 K the first 0.5 mm of the crystal appear to absorb almost all of the infrared radiation while at 1573 K only about half the radiation is absorbed [63].

4.3. High temperature spectra of TSSG crystals

High temperature spectra in the 350-1000 nm range were also measured for crystals grown by the TSSG method starting at 2013 K in atmospheres with different oxygen concentration. The samples selected were approximately 0.5 mm thick disks cut from crystals Ox4 and Re3 from Ref. [30], because these crystals were grown with the largest difference in oxygen concentration in the growth atmosphere (Ar +2.83 vol% for Ox4 and N_2 for Re3). These spectra show the difference caused by free electrons due to oxygen vacancies. For the high temperature measurements the setup discussed in section 3.1.2 was used, but for the measurements discussed here a high power halogen lamp was used as a light source. This was done because the halogen lamp provides more intensity in the IR range.

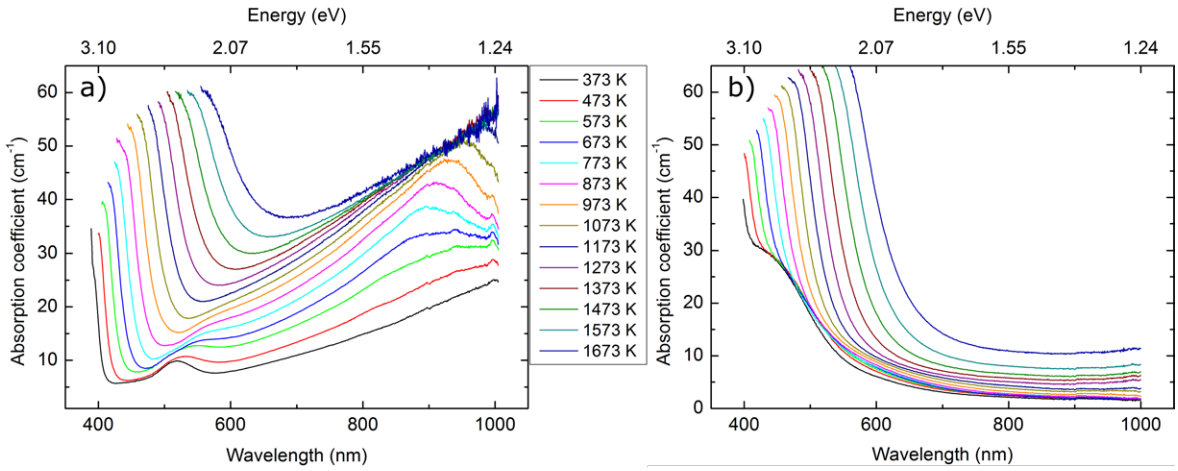

Figure 4.3.1.: High temperature spectra of samples from crystals a) Re3 and b) Ox4. The temperature difference between two spectra is 100 K and the legend applies to both figures.

In figure 4.3.2 the transmission and absorption coefficient values at 980, 850 and 700 nm are compared for the different temperatures [30]. This indicates from which temperature onward the IR transparency will drop and from which temperature on the crystal will cease to be IR transparent. The transmission for these wave lengths is also compared to the room temperature value in figure 4.2.2, since crystal Re3 shows free carrier absorption at room temperature which slightly distorts the picture in figure 4.3.2. The leveling off of the absorption at 980 nm for crystal Re3 in figure 4.3.2 between 573 and 973 K is caused by the decrease in absorption between 950 and 1000 nm for those temperatures (see figure 4.3.1).

Crystal Ox4 shows a wide absorption convoluted with the band gap, which causes its brown color. This does not change with temperature, but is eventually covered up when the temperature rises enough. This absorption is probably caused by light scattering, as discussed in chapter 8. Crystal Re3 has a peak at 518 nm, which appears to shift right with temperature. This peak is probably due to electron transitions in the split up Ti $3d$ bands, which make up the bottom of the conduction band, and shifts by the same mechanism as the band gap (this is discussed in depth in chapter 7). At higher temperatures, this peak is obscured by the rising free carrier absorption.

The figures 4.3.1,4.2.2 b) and 4.3.2 show that the IR absorption in crystal Re3 rises much sooner and faster than for crystal Ox4. From about 1273 K onwards, the transmission of Re3 is so low, it is close to the noise level and the absorption coefficient is around the maximum measurable value of about 55 cm^{-1}. Crystal Ox4, on the other hand, is much more transparent

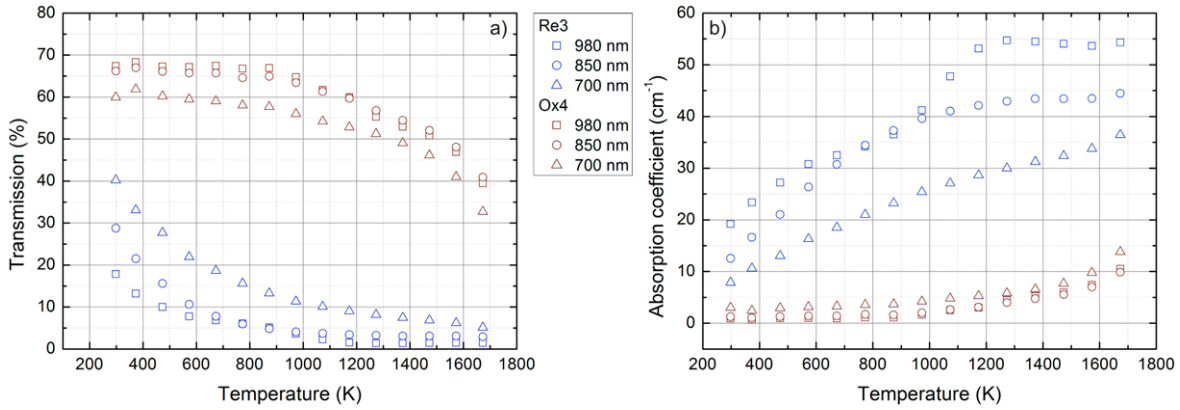

Figure 4.3.2.: Comparison of a) the transmission and b) the absorption coefficient values at 980, 850 and 700 nm for 0.5 mm thick samples from crystals Re3 and Ox4 (after Ref. [30]) The legend in the middle applies to both figures.

at all three wavelengths and only shows an absorption coefficient of up to about 10 cm^{-1} at 1673 K. Also, the transparency does not seem to drop from the room temperature value until the sample is heated to 873 K or more. This difference is due to the free electron concentration of 8.6×10^{18} cm^{-3} in Re3 at room temperature (determined by hall effect measurement). As the temperature rises, the mobility of the electrons decreases [137], which increases the free carrier absorption (see equation 4.2.2). This is because the scattering by phonons increases as the number of phonons rises with temperature and because the number of ionized centers increases even as the contribution of each center decreases with rising temperature (faster electrons spend less time near ionized centers)[144]. Since there are no free carriers in crystal Ox4 at lower temperatures, the dropping mobility has no effect there and the absorption only begins to rise as the free carrier concentration exceeds about $10^{18}cm^{-3}$.

The leveling off of the absorption at 980 nm for crystal Re3 in figure 4.3.2 between 573 and 973 K is caused by the decrease in absorption between 950 and 1000 nm for those temperatures (see Fig. 4.3.1). The decreased absorption there probably does not correspond to a luminescence, but is probably caused by a stray light effect in combination with a very low measured transmission.

4.4. Temperature dependent heat conduction

Even though radiative heat transport has a much larger impact at high temperatures than conductive heat transport (radiative heat transport $\propto \epsilon(T) \times T^4$, conductive heat transport $\propto \kappa(T)\frac{dT}{dX}$, see section 2.2), heat conduction still has an impact, which is larger for lower growth temperatures like those found in TSSG. Because of that, the temperature dependence of the thermal conductivity has been determined for a Verneuil grown crystal (supplied by CrysTec GmbH, Berlin, Germany) and two top-seeded solution grown crystals grown with a starting temperature of 2013 K [30]. One of these crystals was grown in N_2 gas and one in Ar with 2.83 vol% of oxygen (crystals Re3 and Ox4 from Ref. [30]).

The thermal conductivity of STO in the 1573-1823 K temperature range, which is the important range for top-seeded solution growth starting at 1808 K, is between 2.45 and 2.19 $Wm^{-1}K^{-1}$. This is value is quite low: graphite insulating felt (emissivity 0.95) has a thermal conductivity of 1.47 $Wm^{-1}K^{-1}$ at 2273 K in N_2.

The difference between the measured samples is small (see Fig. 4.4.1 a) and the growth atmosphere does not influence the thermal conductivity. In figure 4.4.1 b) the data per

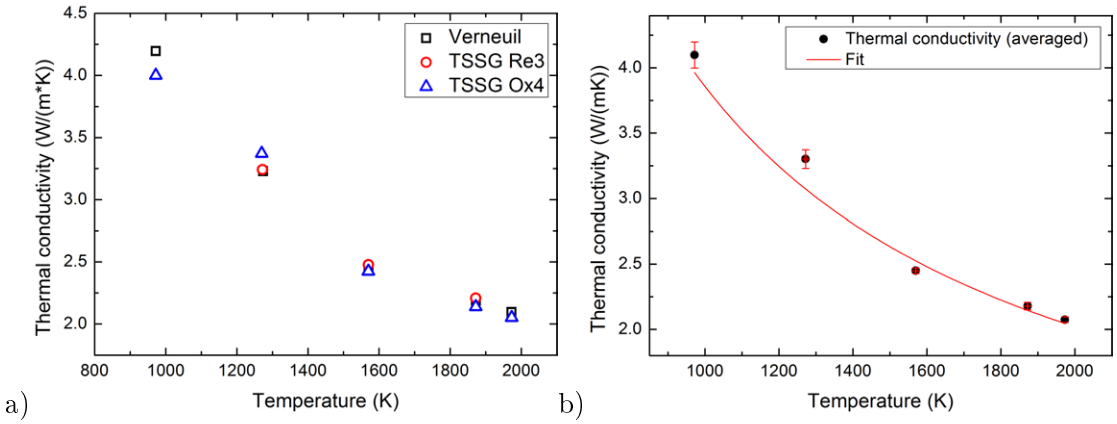

Figure 4.4.1.: a) Temperature dependent thermal conductivity of STO from 973 to 1973 K for Re3, Ox4 and a commercial Verneuil sample. (image adjusted from Ref. [63])

temperature is averaged and fitted with $\kappa = A + B/T$, giving $A = 0.18489$ and $B = 3673$. This function is used since the thermal conductivity of STO is dominated by phonon scattering which has a T^{-1} dependence. Although the radiative heat transport dominates at the growth temperatures for STO, the low thermal conductivity also adds to the problem of removing the crystallization heat from the growth interface.

4.5. Summary

The results in this chapter show clearly that at high temperatures the heat transport through $SrTiO_3$ is very low, both due to a high optical absorption and low thermal conductivity. The infrared spectra show that the absorption is due to free carriers which are formed by thermal excitation over the shrinking band gap and the formation of charged vacancies. The band gap energy and the black body emission maximum also approach each other to within about 0.2 eV, which means the fundamental band to band absorption is a significant factor in reducing the radiative heat transport. Together, all these measurements show that the low heat transport at high temperatures is caused by fundamental properties of $SrTiO_3$ and not by an external factor such as impurities. Increasing the oxygen partial pressure in the atmosphere can reduce or prevent the tendency of spiral or foot formation in top-seeded solution growth starting at 2013 K, but not in Czochralski growth. At those temperatures, the number of free electrons, both intrinsic and from ionized vacancies, is probably too large already.

The low heat transport at the melting point will cause growth instabilities and crystal spiraling. The infrared absorption and the fundamental absorption both show a strong temperature dependence, which means that when the growth temperature is reduced, as it is in TSSG, stable automated growth becomes possible. Another option is to use the EGF method. There a stoichiometric melt is used, but the crystal grows from a layer of molten material on a shaper that sticks out above the melt and is fed by a capillary. In the Cz method, the melt level drops during growth, moving the growth interface lower into the crucible. The crucible walls are the hottest part of the growth set up and radiate large amounts of heat onto the crystal, which increases during the growth process. But in the EFG method, the growth interface stays in one place which eliminates that effect and makes it much easier to achieve a homogeneous temperature field. Also, the shape of the meniscus is controlled by the die, further reducing growth instabilities.

With the data measured here, it becomes possible to model the heat transport and temper-

ature gradients for TSSG or EFG growth. The heat transport through STO makes stable Cz growth very difficult and the high temperature gradients required in manual growth to prevent spiraling mean that the crystal quality is not very high (see section 2.3.2 and table 2.3.3). The heat transport is not easy to calculate, since the temperature profile has a large influence on the infrared absorption of the crystal and radiation is not only passing through the crystal from the melt, but also from the sides of the crucible and from the after heater if one is used. With the high absorption coefficients in the infrared range found here and the band gap approaching the black body emission maximum near the melting point of stoichiometric STO, the first few millimeters of the crystal absorb almost all infrared radiation. The heat transport through much of the crystal will probably have to happen by conduction at the melting point. For TSSG growth, especially starting below 1808 K, the radiative heat transport becomes much more efficient.

Acknowledgments

I would like to thank Martin Naumann for measuring the high temperature spectra shown in this chapter, as well as Mike Pietsch and Dr. Klaus Irmscher for their help with the low temperature spectra. Additionally, I would like to thank the thermophysical properties department of NETZSCH-Gerätebau GmbH for measuring the temperature dependent heat conduction, Thomas Wurche for cutting the samples and Manuela Imming-Friedland and Viola Lange for the chemo-mechanical polishing.

5. Compensation doping of $SrTiO_3$

5.1. Sc doped STO

To grow scandium doped $SrTiO_3$ from the melt, the micro pulling down method was used (see section 2.3.5). The advantages of this method are small melt volumes (in the order of 1 g of material) and high growth rates of up to 60 mm/h. Because of the capillary at the bottom of the crucible, the incorporation of dopants should be diffusion controlled and therefore a distribution coefficient close to 1 can be expected after a short growth time (see section 2.3.5). The disadvantages are that the exact amount of dopant weighed in is hard to control for such small weights and the diameter of a typical fiber is only about 1 mm, though it is possible to grow fibers with a larger diameter or even ribbons with a differently shaped crucible capillary. Once the growth of undoped $SrTiO_3$ was successfully achieved, it was attempted to grow Sc doped fibers. Sc is reported to be a p-type dopant in $SrTiO_3$ that occupies the Ti position [71, 72] and could compensate free electrons from oxygen vacancies at high temperatures. This would increase the infrared transparency and increase the stability of melt growth. However, p-type doping cannot negate the intrinsic free carrier absorption since the concentration of intrinsic free carriers is too high to compensate by doping (see section 4.2). Also, the Sc concentration has to be similar to the concentration of n-type defects, or the free carrier absorption will be increased instead of lowered.

The Sc doped fiber MPD-Sc was grown as detailed in section 2.3.5. Due to the melt flowing out of the crucible, the crystal has a large diameter of 3-6 mm (see Fig. 2.3.10). The concentration of Sc incorporated was determined by the ICP-OES method and found to be 0.105±0.004 at-ppm of the crystal (see table 5.1.1) which corresponds to a maximum of 1.76×10^{19} cm^{-3} holes. Two wafers were cut out of the crystal and chemo-mechanically polished (MPD-Sc-A and B). These wafers were investigated with optical microscopy and scanning electron microscopy to investigate whether the Sc had formed secondary phase particles or was integrated in the lattice. No particles were found, so it is believed that the Sc atoms were incorporated in the STO lattice. The conductivity of the grains of the wafers were measured with the four probe method and the material was found to be highly resistive. This fits with the findings of Higuchi et al. who found that Sc is a deep dopant in $SrTiO_3$ [72].

EDLM mapping was performed on wafer MPD-Sc-A (see section 3.2.4). The results are shown in figure 5.1.1. The mapping clearly shows four main grain orientations in the crystal, though two of these are not homogeneous and appear to contain subgrains. The melt outflow caused several grains to grow in random orientations at the side of the seed crystal and the original orientation appears to be completely lost. XRF mapping could not be used to search for Sc second phase particles since the concentration of Sc was below the detection limit.

Table 5.1.1.: Element concentrations of crystal MPD-Sc.

[Sr] (at-%)	**[Ti] (at-%)**	**[Sc] (at-ppm)**
20.11± 0.029	19.84± 0.15	0.105±0.004

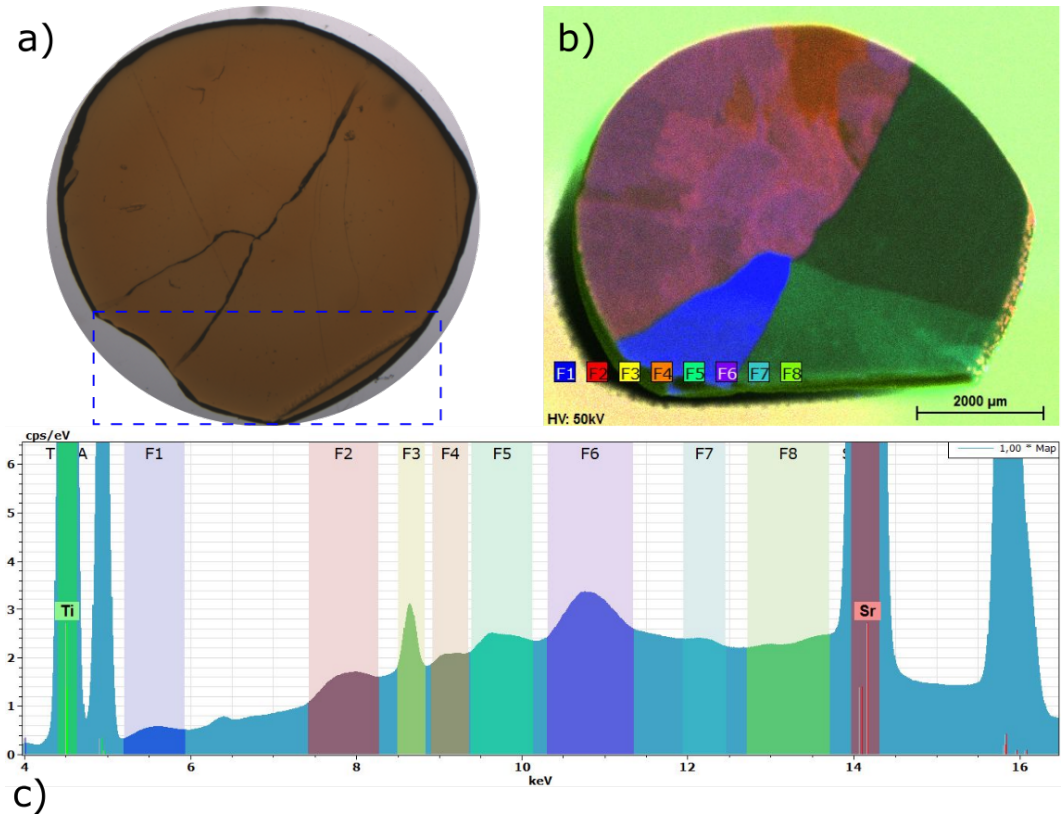

Figure 5.1.1.: a) Photograph of sample MPD-Sc-A. The blue box marks the area cut away for ICP-OES. b) Results of the EDLM mapping. The crystal clearly shows several grains and subgrains. c) XRF spectrum of the sample with the Bragg- and element peaks marked.

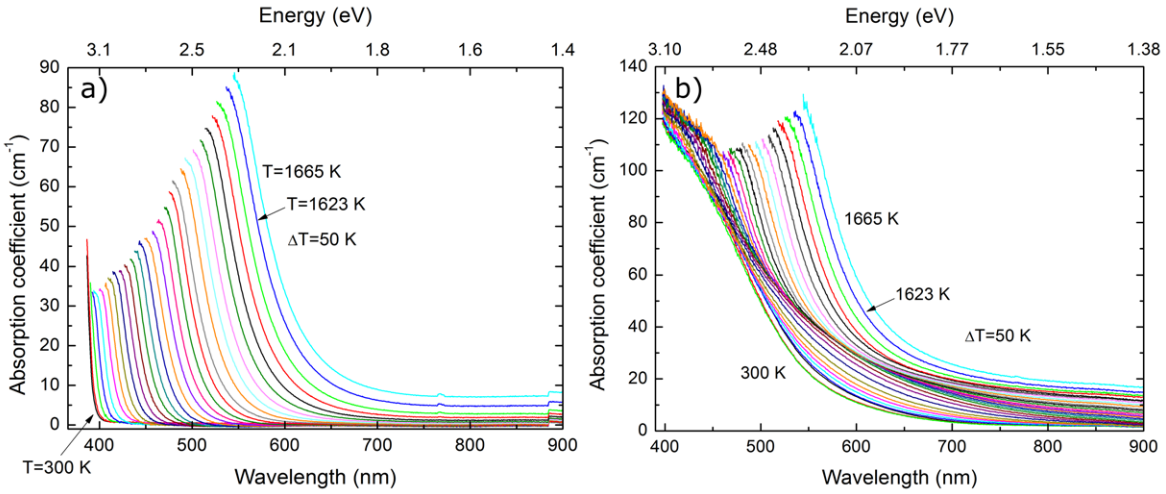

Figure 5.2.1.: High temperature UV/VIS spectra of a) Verneuil wafer and b) MPD-Sc-A, recorded with the IsoPlane spectrometer (see section 3.1.2). Sample MPD-Sc-A showed significant annealing (see Fig. 5.2.2), so only the spectra measured during cooling are shown here.

5.2. High temperature spectroscopy

If the compensation doping is effective, the high temperature spectra should reveal this. Because of that, high temperature UV/VIS and IR spectra were measured for MPD-Sc-A and a Verneuil reference sample. The reference sample was measured as well since these were the first two series acquired with the IsoPlane spectrograph.

The high temperature UV/VIS spectra of the Verneuil reference sample shows the expected behavior (see Fig. 5.2.1 a). MPD-Sc-A showed significant annealing during the high temperature UV/VIS series, so only the cooling spectra are evaluated (see Figs. 5.2.1 b and 5.2.2). Here the brown coloration obscures the shift of the band gap below about 1200 K. Both series do not show the free carrier absorption, so the effect of the compensation doping cannot be determined from these spectra.

High temperature infrared spectra were measured for MPD-Sc-A and a Verneuil sample for comparison (see Fig. 5.2.3). A new comparison series was measured rather than using the data from section 4.2 to ensure minimal differences in alignment. As can be seen in figure 5.2.3, the Verneuil sample shows the expected behavior, with the free carrier absorption dominating the spectrum and little absorption measured under about 1300 K. This can also be seen when the relative transmission in figure 5.2.4 is compared to figure 4.2.2: the behavior is qualitatively the same and the measured values are close. The multi-peak feature below 1400 nm is caused by atmospheric gases.

The high temperature IR series for MPD-Sc-A looks quite different. The absorption becomes significant around 923 K and slowly increases, with a very broad peak just above 1200 nm dominating the spectrum. The free carrier absorption appears to rise as well since the long wavelength side rises comparably. The relative transmissions show again that MPD-Sc-A begins absorbing at lower temperatures and reaches a similar absorption to the Verneuil sample. This behavior suggests that more of the dopant becomes ionized as the temperature rises until the free carrier absorption due to excitation of charge carriers over the band gap starts to take over at higher temperatures. The contribution of oxygen vacancies to the conductivity appears to be over compensated.

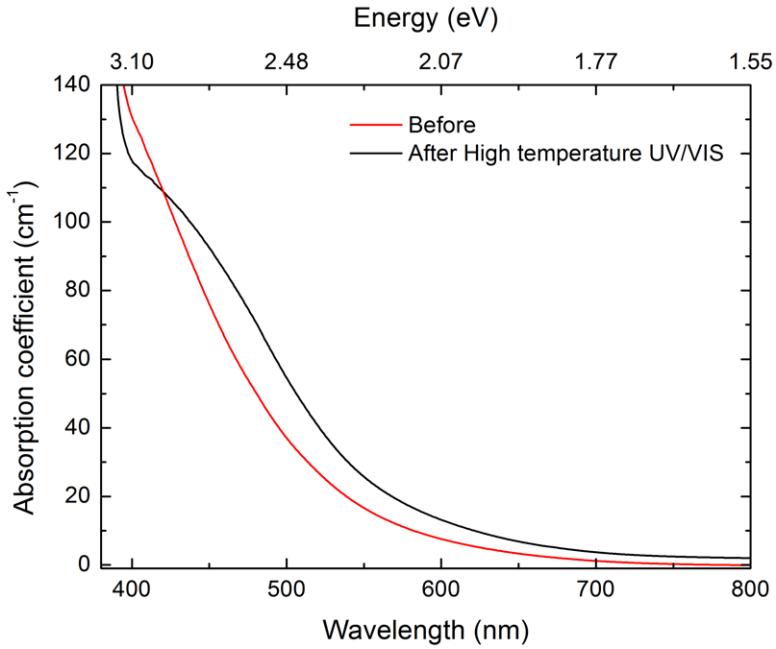

Figure 5.2.2.: Room temperature spectra of MPD-Sc-A before and after the UV/VIS high temperature spectrometry series.

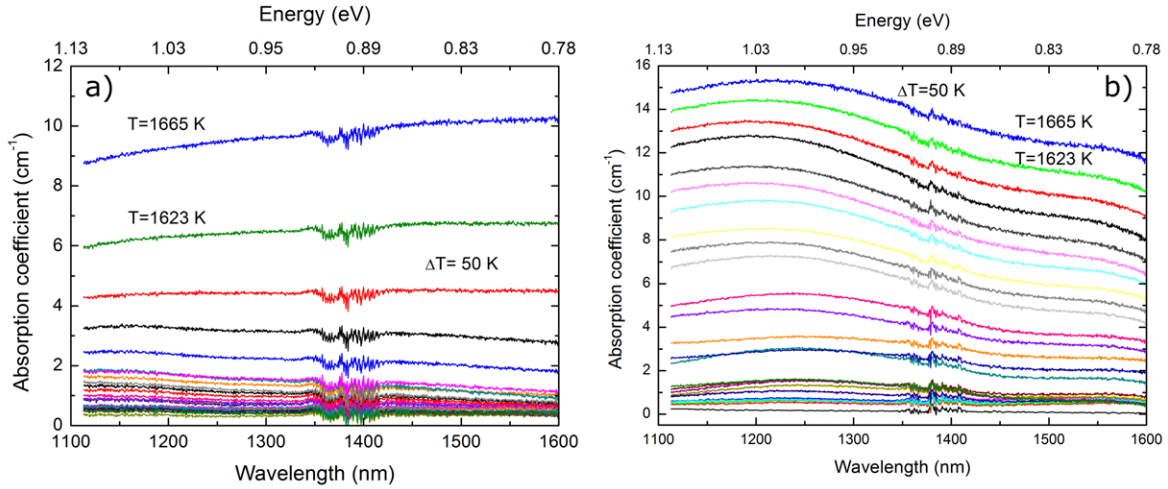

Figure 5.2.3.: High temperature infrared spectra of a) the Verneuil sample and b) MPD-Sc-A. The Verneuil sample shows the expected free carrier absorption, while MPD-Sc-A shows a peak at just over 1200 nm. The absorption in the Sc doped sample is higher. The multi-peak feature below 1400 nm is caused by atmospheric gases (the high temperature setup has a long beam path through the ambient atmosphere, see section 3.1.2).

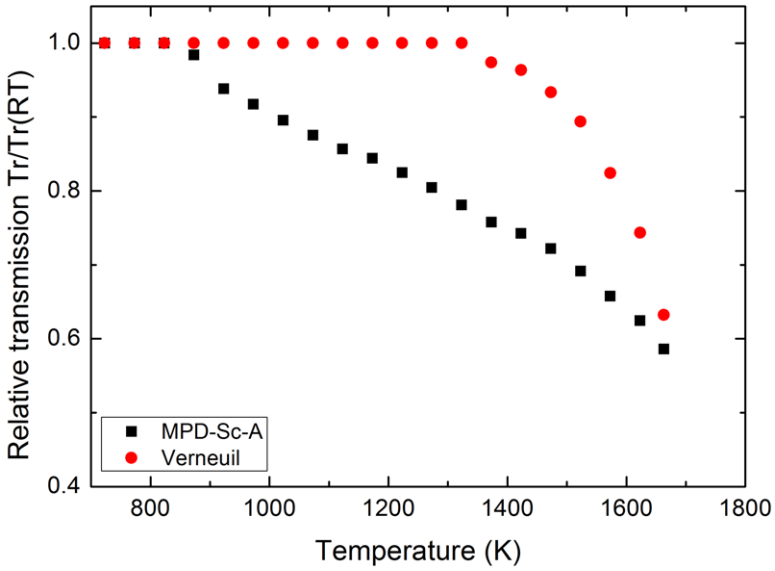

Figure 5.2.4.: Relative transmission at 1600 nm for MPD-Sc-A and the Verneuil wafer.

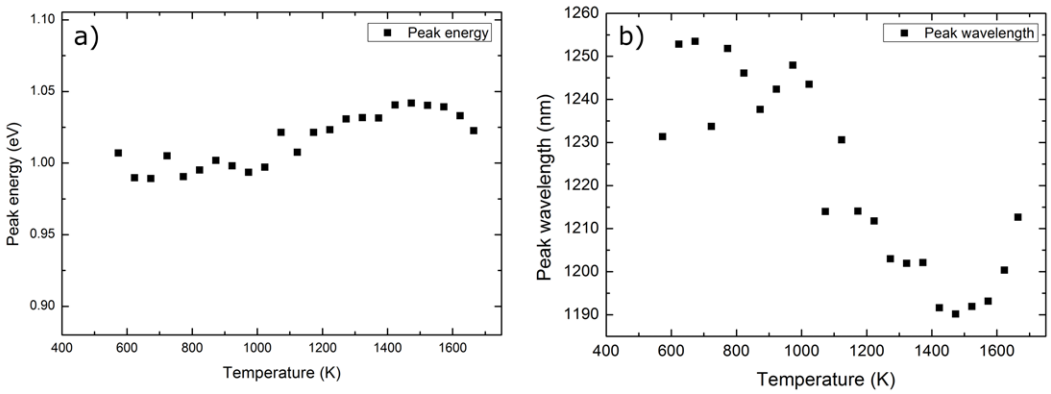

Figure 5.2.5.: a) Peak energy and b) peak wavelength.

The peak around 1200 nm in the MPD-Sc-A spectrum appears to be tied to Sc, since it increases with temperature just like the ionized fraction of Sc dopant ions. However, as figure 5.2.5 shows, the peak barely shifts, which means the valence and conduction bands are most likely not involved in this transition since the band gap decreases much more in this temperature range. The nature of this absorption band remains unclear for now.

5.3. Summary

The doping of $SrTiO_3$ with Sc was successful, but did not decrease the high temperature IR absorption. The doping level was higher than the contribution of the oxygen vacancies to the free carrier concentration, resulting in a higher absorption which was nearly equal to the absorption of undoped STO. When the carrier concentration is determined by the intrinsic free carriers excited over the band gap, the free electron concentration is too high to be compensated by p-type doping (see Fig. 4.2.1). The Sc doped sample showed a broad absorption peak just above 1200 nm. It is unclear what causes this absorption band, but it appears that the ionization of Sc ions plays a role. Also, the peak barely shifts with

temperature (if at all), so an absorption that involves the valence or conduction band can be excluded.

Acknowledgments

I would like to thank Martin Naumann for measuring the high temperature IR spectra, Dr. Rainer Betram for the ICP-OES measurements, Dr. Christo Guguschev for the EDLM measurements and Dr. Steffen Ganschow for his support with the MPD growth. Also I am grateful to Manuela Imming-Friedland and Viola Lange for the chemo-mechanical polishing

6. Influence of the growth atmosphere on the optical properties

6.1. Introduction

Stoichiometric $SrTiO_3$ is transparent and colorless. However, as-grown crystals are rarely colorless. Verneuil grown crystals are blue/black and highly conductive in the as-grown state and need to be annealed to lose this coloration (see chapter 7 and Ref. [32]). Crystals grown by other methods tend to either be blue/black or yellow to brown, depending on the growth atmosphere, though sometimes other colors were found. The blue/black coloration can usually be removed by annealing in an oxidizing atmosphere, but the brown coloration cannot be annealed away. To understand the origin of different optical properties in detail, our group investigated crystals grown under different growth conditions.

The influence of the growth atmosphere on the crystal coloration became apparent in a study on the influence of the atmosphere on crystal growth stability in top-seeded solution growth below 2013 or 2073 K [30]. This influence was then studied in detail for laser heated pedestal grown crystal fibers [77]. The latter growth method was selected since it does not use a crucible, which allows almost any atmosphere to be used. Also, the LHPG method has high growth rates and the small size of the fibers makes it fairly cheap and fast to grow crystals in a wide range of atmospheres. Here the different crystals and growth conditions are discussed while the mechanisms behind the blue and brown coloration are discussed in chapters 7 and 8.

The work on the top-seeded solution grown crystals is taken from reference [30] and the work on the laser heated pedestal growth crystals is from reference [77]. Both of them are articles published in CrystEngComm where I was a co-author.

6.2. Results and discussion

6.2.1. Top-seeded solution grown crystals

Cylindrical $SrTiO_3$ single crystals with diameters between 25 and 29 mm and lengths up to 30 mm were grown by high temperature top-seeded solution growth (TSSG) in a flow of nitrogen or argon carrier gas mixed with oxygen (0.16 to 2.83 vol%, see table 2.3.1 for growth conditions). The chamber gas pressure was held at atmospheric pressure. The grown crystals were found to be transparent to translucent and had a brownish tint (Fig. 6.2.1 a–c). If the crystal was pulled along the ⟨100⟩ direction, the growth was stable and the interface was characterized by a planar (100) facet during growth of the cylindrical section. Well pronounced {100} and less pronounced {110} facets were formed at the periphery of the crystal (Fig. 6.2.1 a–c). Even a relatively defined tail section could be grown without foot formation.

If the crystal was grown with less oxygen in the carrier gas (argon, 5N purity), the boule shape deviated from cylindrical to spiral shape after a crystal length of approximately 24 mm, as can be seen in figure 6.2.2. Except for the difference in oxygen partial pressure, the crystals Ox3 and Ne1 were grown under identical growth conditions. It is worth noting that the crystal coloration changed over the length. The cone and first part of the cylindrical

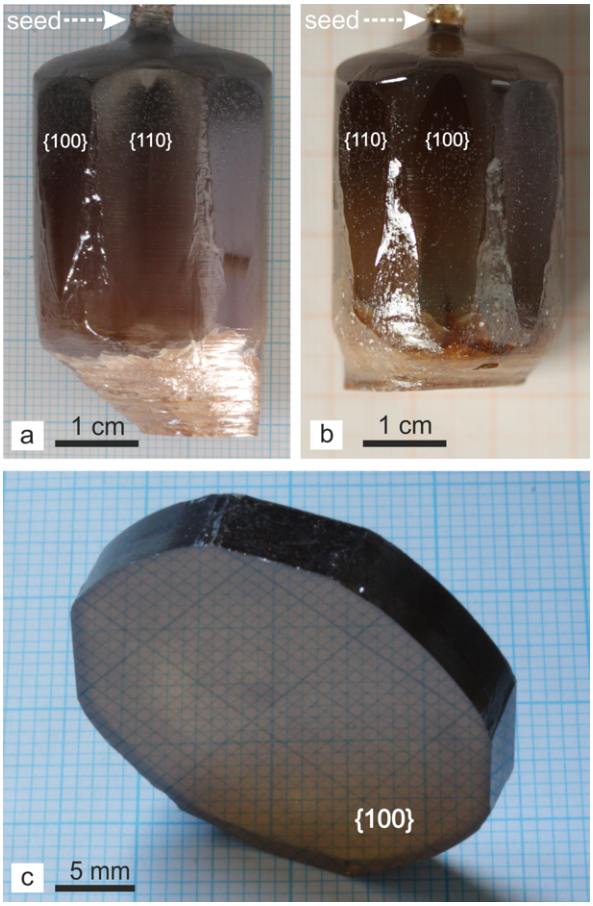

Figure 6.2.1.: (a–b) $SrTiO_3$ crystals Ox1 and Ox2 grown by top-seeded solution growth at temperatures below 2013 K. (c) Cut and polished section of the crystal shown in (a). (Taken from Ref. [30]).

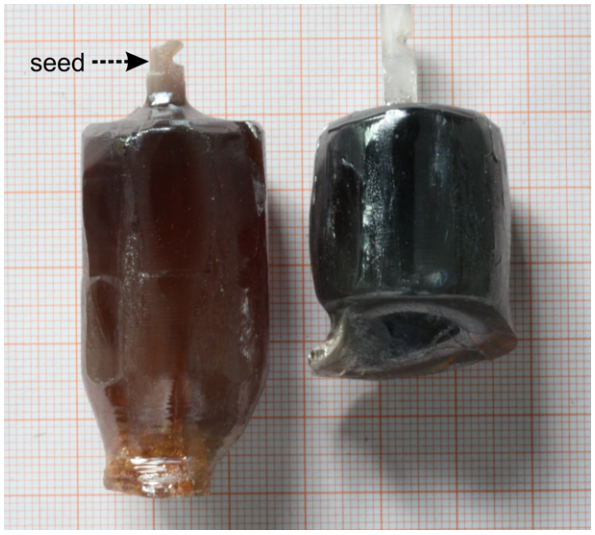

Figure 6.2.2.: $SrTiO_3$ crystals grown in oxygen enriched argon atmosphere (left crystal, Ox3) and in pure (5N) argon (right crystal, Ne1). Except for the difference in oxygen partial pressure, the crystals were grown under identical conditions. (Taken from Ref. [30]).

section of the boule of crystal Ne1 had a distinct bluish/greyish tint, whereas at a cylinder length of approximately 10 to 15 mm the crystal showed large colorless sections (Fig. 6.2.3 b). A slightly yellowish coloration was observed at the crystal foot.

For crystals grown in a flow of pure nitrogen (5N purity), a stable growth was possible only up to a critical cylinder length between 7 and 13 mm. Exceeding this length, a very pronounced foot appeared and spiral formation started. Furthermore, it was not possible to stabilize the growth even when high temperature gradients were applied. Figure 6.2.4 a) shows a typical crystal grown under these conditions (see table 2.3.1). As-grown crystals in a nitrogen atmosphere are nearly opaque (Fig. 6.2.4a–b) and show blue chatoyance on the surface. Their coloration is between dark blue and dark gray. In thin polished sections, differences in the coloration and transparency can be distinguished (Fig. 6.2.3), mainly caused by slight differences in free carrier concentrations.

6.2.2. Laser heated pedestal grown crystals

The growth conditions for the series of fibers grown form stoichiometric (ST) and Sr enriched melt (SR) are detailed in section2.3.6. Depending on the oxygen concentration in the growth environment (table 2.3.2), the LHPG crystals showed different colorations (Fig. 6.2.5). Those grown in oxygen rich conditions (5 - 40 vol%) had typically strong brown to orange colors. Growth in atmospheres containing less oxygen (0.4 – 5 vol%) yielded more transparent and less tinted fibers. By using strontium enriched feed rods in an atmosphere with approximately 1 vol% oxygen, colorless transparent crystals were grown. Growth in atmospheres containing oxygen concentrations at the ppm level like in nitrogen and in Argon (both 5N purity) led to grayish or bluish tints. Due to high temperature gradients most of the crystals were cracked during cooling to room temperature.

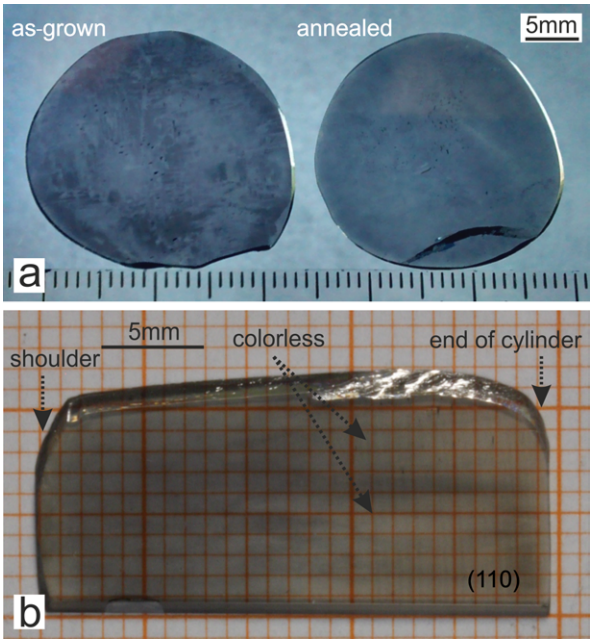

Figure 6.2.3.: (a) As-grown and annealed (1923 K for 10 h) sections of crystal Re3. (b) As-grown sample of crystal Ne1, cut parallel (110) and close to the periphery of the crystal. (Taken from Ref. [30]).

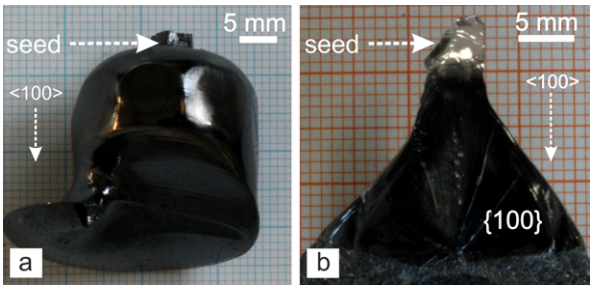

Figure 6.2.4.: $SrTiO_3$ crystals grown under slightly reducing conditions (5N nitrogen). (a) Foot and spiral formation after a few mm growth of a cylindrical part (crystal Re1). (b) Convex interface shape during diameter expansion (crystal rapidly frozen into the melt) shown for a centrally (100) cleaved crystal (crystal Re2). (Taken from Ref. [30]).

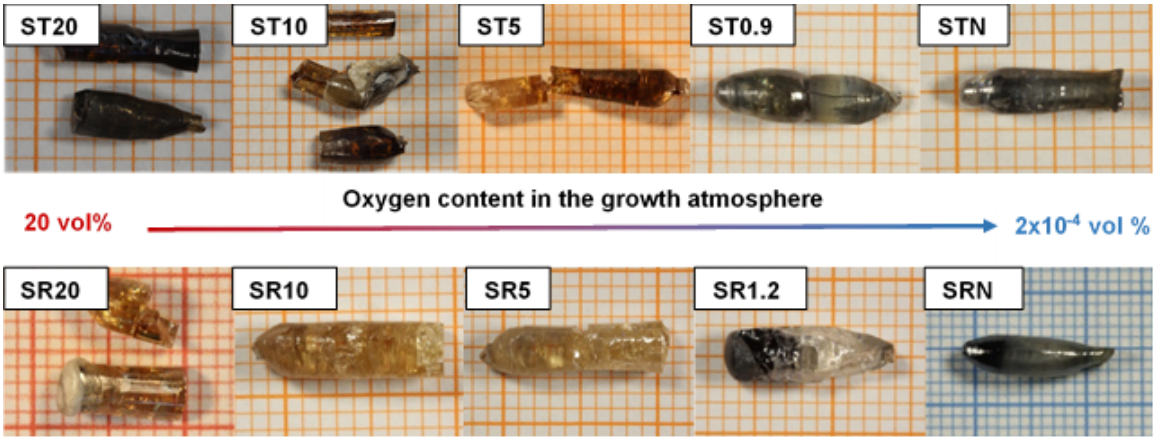

Figure 6.2.5.: Selected crystals representing the results of different growth conditions. Fibers grown from the stoichiometric feed material (ST-series) are shown in the top row. The bottom row contains the SR-series, with crystals grown from starting ceramics with Sr-excess. The numbers indicate the oxygen content of the growth atmosphere in vol%. Note that although no oxygen was added to the atmospheres of STN and SRN, there is however still residual oxygen present in the nitrogen carrier gas ($<2\times10^{-4}$ vol%). (Taken from Ref. [77]).

6.2.3. Optical properties

In figure 6.2.6, optical absorption spectra of the top-seeded solution grown crystals from the ultraviolet (UV) to the near infrared (IR) range are shown. The brown crystal Ox4 shows a broad absorption in the 390 nm to 750 nm range (discussed in chapter 8) while the bluish-grayish crystals (e.g. crystal Re3) show a peak at 513 nm and a broad absorption which increases with the wavelength. The peak around 513 nm is also observed for as-grown Verneuil crystals [48] and could be related to the formation of Ti^{3+} when the crystal is oxygen deficient (discussed in chapter 7). The broad absorption at higher wavelengths is characteristic of free carriers ($\alpha_{fc} \propto \lambda^2$). The difference between the IR absorption of the brown and bluish-grayish crystals indicates that the lower growth stability of crystals grown at low oxygen partial pressure (N50 N_2 gas) is caused by higher absorption in the IR due to free carriers generated by oxygen vacancies.

The absorption of infrared light by free carriers has a massive effect on growth stability, as is discussed in section 2.2 and chapter 4. Both crystals (Ox4 and Re3) show a large drop in transmission with increasing temperatures (see section 4.3). This drop is caused by the increase in free carriers, both thermally excited over the shrinking band gap and created by oxygen vacancy formation and it is larger for Re3 since the crystal already has a significant free carrier density at room temperature. This explains the lower growth stability and the spiraling observed for crystals grown conditions with low oxygen concentrations.

Crystal Ne1 was grown in N50 Ar. Even though this means a slight increase in oxygen partial pressure, the crystal coloration is comparable to crystals grown in nitrogen for the top part of the as-grown bulk crystal. Interestingly, the crystal is partially colorless in the central section as can be seen in figure 6.2.3, and the spectral properties are comparable to transparent and colorless Verneuil crystals (Fig. 6.2.6). During crystallization from self-flux the growth temperature is continuously lowered due to depletion of strontium oxide in the solution. At some point, conditions are reached at which the oxygen vacancy concentration is low enough to be compensated by diffusion of oxygen into the lattice during further cooling. Obviously,

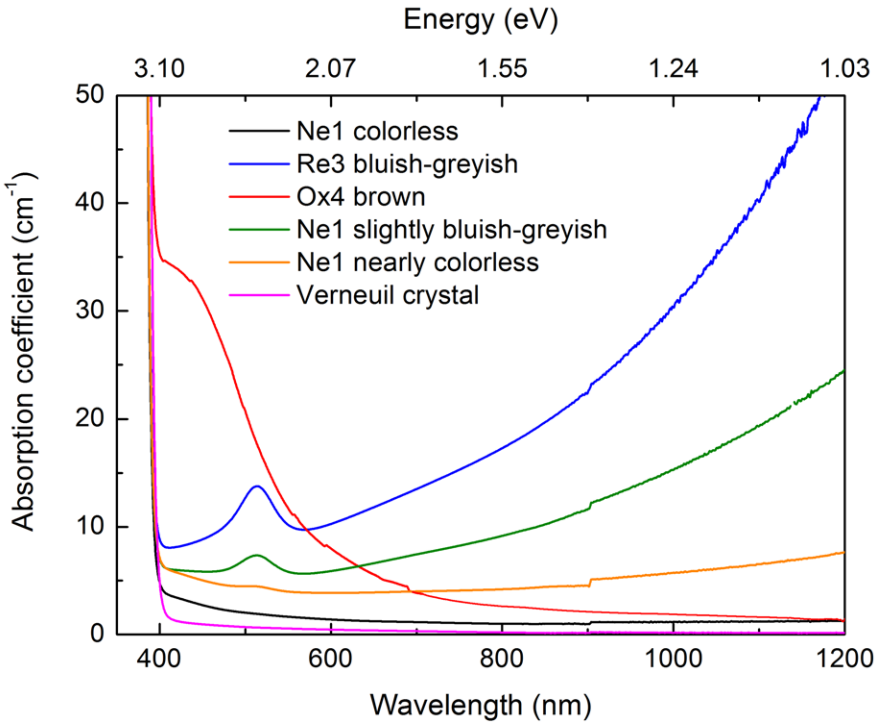

Figure 6.2.6.: Absorption coefficient depending on wavelength shown for crystal sections prepared from as-grown crystals and for a colorless Verneuil crystal. All samples were chemo-mechanically polished. (Taken from Ref. [30]).

under these conditions the crystal is neither significantly reduced nor was it exposed to a high oxygen partial pressure. Additionally, $SrTiO_3$ dissociation is reduced at lower temperature.

A second change in crystal coloration to a yellowish tint can be seen for the crystal part grown at the end of the growth run. Due to blocking of infrared light in the bluish-grayish crystal part of the shoulder and the top of the cylinder (Fig. 4b), the growth stability is reduced and the crystal tends to grow in directions where the transmission is not hindered (see Fig. 6.2.2 and section 2.2). This situation can be avoided completely under an oxygen enriched nitrogen or argon atmosphere because it increases the relative infrared transmission (see Fig. 6.2.6) of all crystals and crystal parts. That means the crystal growth process becomes more stable due to increased heat flow to the top of the crystal, which is at a much lower temperature than the growth interface. The risk of a symmetry breakdown is reduced due to more effective cooling of the growing crystal. The absorption between 400 and 700 nm is characteristic of brown crystals grown at high oxygen partial pressure (0.16 to 2.83 vol% oxygen in the gas flow). In figure 6.2.6 typical spectra are shown for crystal Ox4 grown in an atmosphere containing 2.83 vol% oxygen.

The absorption spectra of the LHPG crystal fibers are shown in figure 6.2.7 a) and b). All analyzed fiber crystals grown in an atmospheres to which oxygen was added, both those grown from stoichiometric and Sr enriched feed rods, show broad absorption in the 400–500 nm range (see Fig. 6.2.7). The crystals from both series clearly become more transparent in the 400-500 nm range as the oxygen partial pressure in the growth atmosphere is decreased.

The fibers from the SR-series show a lower absorption in the 400-500 nm range (see Fig. 6.2.7 b). The general trend that the absorption in the 400-500 nm area rises with increasing oxygen partial pressure in the growth atmosphere holds for this series as well. Crystal SR20 shows the highest absorption in the 400-500 nm range in the series, but still has only a light

brown coloration. This absorption is lower than for ST20, which was grown in an atmosphere with equal oxygen content. Crystal SR1.2 appears colorless to the eye (see Fig. 6.2.5) and shows almost no absorption in the 400-500 nm region above the baseline level. The absorption of SR1.2 is clearly much lower than that of crystal ST0.9.

Crystal STA shows only minor absorption in the visible region that rises with the wavelength, characteristic of free carrier absorption. A small peak is visible around 519 nm, which appears to be the same as the one found at 513 nm in the TSSG crystals grown in Ar or N_2. The highest point of this peak is found at a slightly different wavelength, but that can be attributed to the width of the peak, its relatively low height and the free carrier absorption which changes the base line absorption. As discussed in chapter 7, the peak is probably caused by an intra-conduction band transition between bands largely made up of Ti 3d orbitals separated by crystal field splitting.

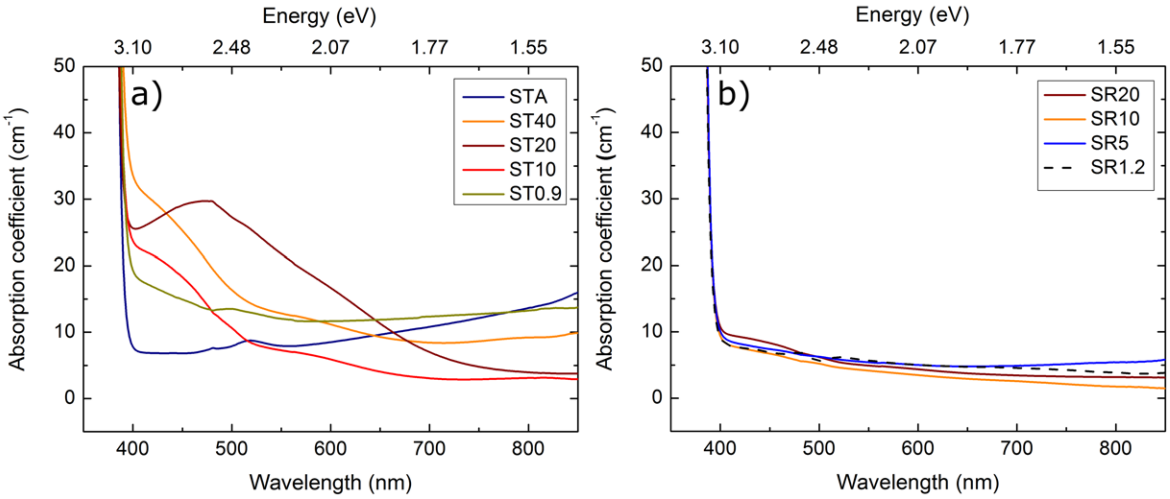

Figure 6.2.7.: Absorption spectra for (a) the ST series and (b) the SR series. (Taken from Ref. [77]).

Both the ST and the SR series show significant baseline absorption, even though crystals like SR1.2 are colorless to the eye. This deviation can be explained by the purely mechanical polishing of the samples which produces a relatively high surface roughness and leaves grinding marks. Grinding marks cause diffuse scattering and that results in higher absorption coefficients. This can be seen by a comparison of differently polished Verneuil-grown samples (5×5 mm standard wafer supplied by CrysTec GmbH) (see Fig. 6.2.8). One sample was mechanically polished similar to the rest of the fibers and the other sample was chemo-mechanically polished. If the fluctuations (which are caused by preparation artifacts) in the Vernueil (mechanical) curve are neglected, the average difference in the absorption coefficient over the whole wavelength range is roughly 3-4 cm^{-1}.

6.2.4. Crystal composition

The results of the ICP measurements of several TSSG crystal samples (Fig. 6.2.9) indicate a trend that brownish and nearly colorless crystals are enriched in Sr, but are not very deficient in oxygen when grown with this method. Reduced bluish-grayish crystals show a high deficiency in oxygen and enrichment in strontium compared to titanium. The deviations from stoichiometry in the crystals are in a similar range as those reported for thin layers [91] and ceramics [90]. By plotting the calculated Sr/Ti ratios (Fig. 6.2.9) for different TSSG

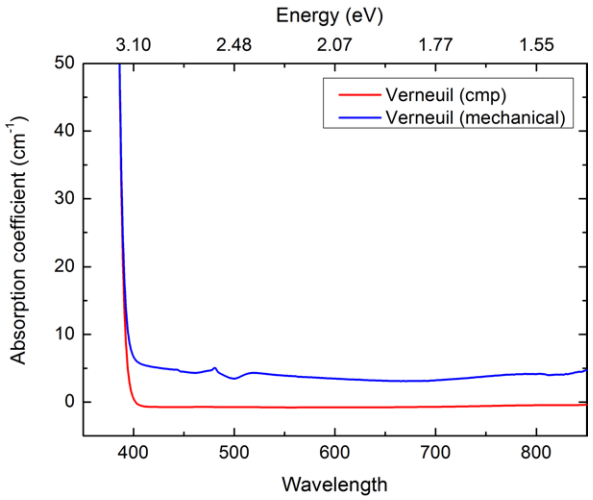

Figure 6.2.8.: Absorption spectra for the two samples prepared from a commercial Verneuil crystal (supplied by CrysTec GmbH). Verneuil (mechanical) was polished like the fiber samples in this work. Verneuil (cmp) was chemo-mechanically polished. A significant difference in absorption is apparent, which explains the rather high absorption coefficients, even though some fibers (e.g. SR1.2) show very little to no coloration to the eye. (Taken from Ref. [77]).

grown crystals, one can see that the highest Sr/Ti ratios were determined for crystals which were grown in nitrogen or argon (N50 purities). This high enrichment of strontium could be the result of strontium diffusing into the lattice from the the gas phase, where Sr is especially present in reducing growth conditions. This additional amount of strontium is generated mainly by evaporation from the melt solution (SrO delivered by reaction 2.4.1 which then partially reacts to free Sr via reaction 2.4.2) due to the large surface area and the highest temperatures in the system during the growth process. It is known that the strontium mobility is enhanced because of interaction with oxygen vacancies [145].

Another factor, which cannot be ruled out as an additional contribution for differences in crystal composition (inparticular the Sr/Ti ratios), is a possible change in the equilibrium composition depending on oxygen partial pressure and temperature, which can be expressed by the shape and position of the solidus curve in the phase diagram. Unfortunately, no thermodynamic data are available so far, which could be used to model this.

Crystal Re1 was grown in a high temperature gradient (no afterheater in use) which could explain why a lower Sr/Ti ratio was detected compared to the sample from crystal Re3. As a result, not only the temperature of the growing crystal is significantly reduced, but also the diffusion rate of Sr and Ti is lowered at lower temperatures. Slight differences in composition were also found for samples selected from different locations of the crystals. This is the result of different system temperatures (depending on the crystallized fraction), associated with a lower oxygen deficiency in the crystals at lower temperature and lower fugacity of the dissociation products.

As-grown $SrTiO_3$ solid solutions are close to the theoretical stoichiometric composition if the crystal is grown at relatively low temperature and at a sufficiently high oxygen partial pressure. The coloration of these crystals is just slightly yellowish. The determined composition is presented in figure 6.2.9 for the foot section of crystal Ne1 and for crystal T1 from Ref. [31] which was grown in a high temperature gradient, below 1813 K and in air. Furthermore, annealing of $SrTiO_3$ solid solutions can be used to shift the composition and thereby to modify

the coloration of the crystals. We found in this study that the oxygen diffusion is hindered for Sr enriched oxygen deficient crystals. This was found for as-grown crystals (crystal Re3) which were annealed in air at a temperature of 1923 K for 10 hours. After annealing, the sample was still deficient in oxygen but less enriched in strontium. The Sr/Ti ratio is close to 1 (see Fig. 6.2.9).

The results of the ICP-OES measurements of the LHPG fiber crystals are presented in figures 6.2.10 and 6.2.11.

Starting from ST40 (grown at high oxygen partial pressure), the Sr/Ti ratio in the series grown from stoichiometric feed rods decreases steadily towards STN (grown at very low oxygen partial pressure). Another feature of the obtained chemical data for the ST-series is the drop of the Sr/Ti ratio between ST10 and ST5. The data indicates that there are apparently two levels of more or less comparable ratios. One for the samples grown in environments containing more than 10% oxygen and one for environments containing less than 5% oxygen. A transition between these two levels can be identified in the range between 5 and 10 vol% oxygen (see Fig. 6.2.11) even though a significant change in color does not occur until the oxygen partial pressure is about 1 vol%.

In addition to the selected fiber samples from the SR series, one of the feed rods for this series has been measured to verify its Sr-excess, which is only 0.5 at%, altough the powder it was sintered from had 3 at% excess, compared to stoichiometric $SrTiO_3$. This loss of Sr can be attributed to the long sintering treatment which leads to significant evaporation of SrO. The chemical compositions of SR10 and SR5 are similar to the compositions of ST10 and ST5, respectively. The main differences are the higher Sr concentrations and thus higher Sr/Ti ratios for the SR series. The transparent crystal, SR1.2 is almost stoichiometric. The tendency to lower Sr/Ti ratios in the direction of lower O_2 partial pressure from the ST growth series can, with the exception of SR20, be confirmed. In the ST series, sample ST20 fell out of line in coloration due to a very broad absorption between 400 and 650 nm, which is also reflected in its composition if compared with compositions obtained from ST40 and ST10. An oxygen excess in the sample is highly unlikely for perovskites and therefore the most likely explanation is an outlier for one of the measurements (either Sr or Ti). Compared to the ST-series, SR20 does not follow the identified trends as it shows an almost stoichiometric composition.

The chemical element analysis (Fig. 6.2.10) revealed that the Sr concentration in the crystals in both series drops with decreasing oxygen partial pressure (with the exception of SR20). This trend is the opposite of what was found for the crystals grown by TSSG, where samples grown in argon or nitrogen (5N purities) atmospheres show higher Sr concentrations than the ones produced in oxygen enriched atmospheres. In top-seeded solution growth, this is attributed to higher Sr mobility in the presence of oxygen vacancies whose concentration is naturally high in reducing environments [145]. Also, the total partial pressure of Sr containing species will be higher in a reducing atmosphere because both SrO(g) and Sr(g) are present (see Fig. 2.4.2). In a TSSG or Czochralski setup, a large crucible (several cm in diameter) containing the melt and the afterheater above the crucible, are heated. That leads to relatively strong evaporation of respective gaseous species and a relatively large hot zone. Compared to that, the hot zone in an LHPG experiment is very small (dependent on the degree of laser beam expansion several mm^3). Hence, even though outgassing of gaseous species is relatively strong, the absolute amount of species in the atmosphere is comparably low for LHPG. Further, the ratio of volume of the growth chamber to volume of the hot zone is much larger for LHPG, which means that a significant part of the already low level of e.g. Sr(g) will most likely condense at the cool walls of the growth chamber. This way the evaporating species is not available for reincorporation into the crystal, which is given as the explanation

for the higher Sr concentration in the TSSG crystals. The reincorporation is further hindered by the rapidly cooling crystals in the LHPG method.

The behavior of the element concentrations in the LHPG fibers might be explained by the formation of antisite defects. Calculations by Liu et al. revealed that Sr_{Ti} antisites and oxygen vacancies [95]:

$$2SrO + Ti_{Ti}^{\times} + O_{O}^{\times} \rightleftarrows SrTiO_3 + V_{O}'' + Sr_{Ti}^{\bullet\bullet} \tag{6.2.1}$$

are energetically favorable for $SrTiO_3$ in an environment with excess SrO. This model could explain the high Sr/Ti ratios in the SR series and the trend to lower Sr/Ti when the oxygen content in the growth atmosphere decreases, since then Sr and SrO both evaporate (see Fig. 2.4.2). This mechanism, however, is not applicable for the ST series which was grown without excess Sr, but still shows the same trend to decreasing Sr/Ti ratio with decreasing oxygen concentration. Similarly, partial Schottky defect formation:

$$Sr_{Sr}^{\times} + O_{O}^{\times} \rightleftarrows V_{Sr}'' + V_{O}^{\bullet\bullet} + SrO(g) \tag{6.2.2}$$

could serve to explain a low Sr/Ti ratio but not its correlation with atmospheric conditions.

Another approach to explain the trends is the formation of titanium vacancies. Varley et al. calculated that the formation energy of titanium vacancies in oxygen rich environments is substantially lower than in oxygen poor ones (see Ref. [94] and Fig.). Near the hot zone in a LHPG setup, enough energy will be available to create a fair amount of these titanium vacancies:

$$Sr_{Sr}^{\times} + V_{Ti}'''' \rightleftarrows Sr_{Ti}'' + V_{Sr}'' \tag{6.2.3}$$

Because the oxygen vacancy concentration is naturally very high at the melting point (close to the melt zone) Sr migration in interaction with these oxygen vacancies is very effective [145]. Thus, the formation of Sr_{Ti} antisite defects close to the melt zone is very well conceivable in oxygen rich environments and could explain the high Sr/Ti ratios in the experiments with oxygen rich atmospheres. Based on the observations made earlier, it seems reasonable to assume that if the oxygen concentration in the atmosphere drops below a certain value, the number of generated titanium vacancies diminishes and the concentration of Sr_{Ti} decreases accordingly. In this way, the lower Sr/Ti ratios measured for the crystals grown in more reducing atmospheres can be explained.

The optical spectra for both series (Fig. 6.2.7 a) and b) show broad absorption in the 400–500 nm range. Recent transmission electron microscopy investigations revealed the presence of nanometer sized voids in brown STO crystals grown by the TSSG method (see chapter 8). These nano-voids scatter light, which can be described by Mie-scattering (see chapter 8). The theoretical Mie-scattering of these nano-voids was in good agreement with the measured absorption spectra, so it is believed that the same effect is observed here for the crystals grown in an oxygen rich atmosphere.

Varley et al. showed recently, that the formation energy of Sr-vacancies and Ti-vacancies in an oxygen rich environment is lower than in oxygen poor environments [94]. For Sr-vacancies, the formation energy is about 1.8 eV higher in the reducing conditions than in oxidizing conditions. The Sr- and Ti-vacancies could form charge neutral vacancy complexes together with oxygen vacancies, since vacancies in STO are almost always charged. The cation vacancies are negatively charged with respect to the lattice while the oxygen vacancies have a positive relative charge, which creates Coulomb attraction between them. These vacancies could cluster together to form the nano-voids that seem to be responsible for low transmittance in the 400-500 nm range. This explains why that absorption is more pronounced for crystals

grown in oxygen rich atmospheres, but is absent for crystals grown in reducing atmospheres. However, the curve shapes of the relatively small absorption of the brown TSSG crystals investigated in chapter 8 do not exactly match the absorptions measured for the TSSG and LHPG crystals, which indicates that an additional source of coloration is present, possibly the Sr_{Ti} anti-site defects discussed above.

Equal cooling rates for every LHPG experiment allow comparisons between the quenched melt zones. It is noteworthy that here, "quenched" means quick rather than shock cooling. The chemical analysis of the quenched melt zones (see Fig. 6.2.12) revealed that they are all oxygen deficient, independent of the atmospheric conditions. This implies, that the growth front of an STO-fiber grown by the LHPG method will always be oxygen deficient. Further, the Sr concentration in the melt zone drops with decreasing oxygen partial pressure. This can be explained by the evaporation of Sr(g), whose activity rises with decreasing oxygen content in the atmosphere while the partial pressure of SrO(g) is independent of the oxygen partial pressure (see section 2.4). A certain loss of Sr can be also attributed to evaporation during the separation of the crystal, which leaves the melt droplet in the hot zone as the laser power was decreased until solidification and cooling to room temperature.

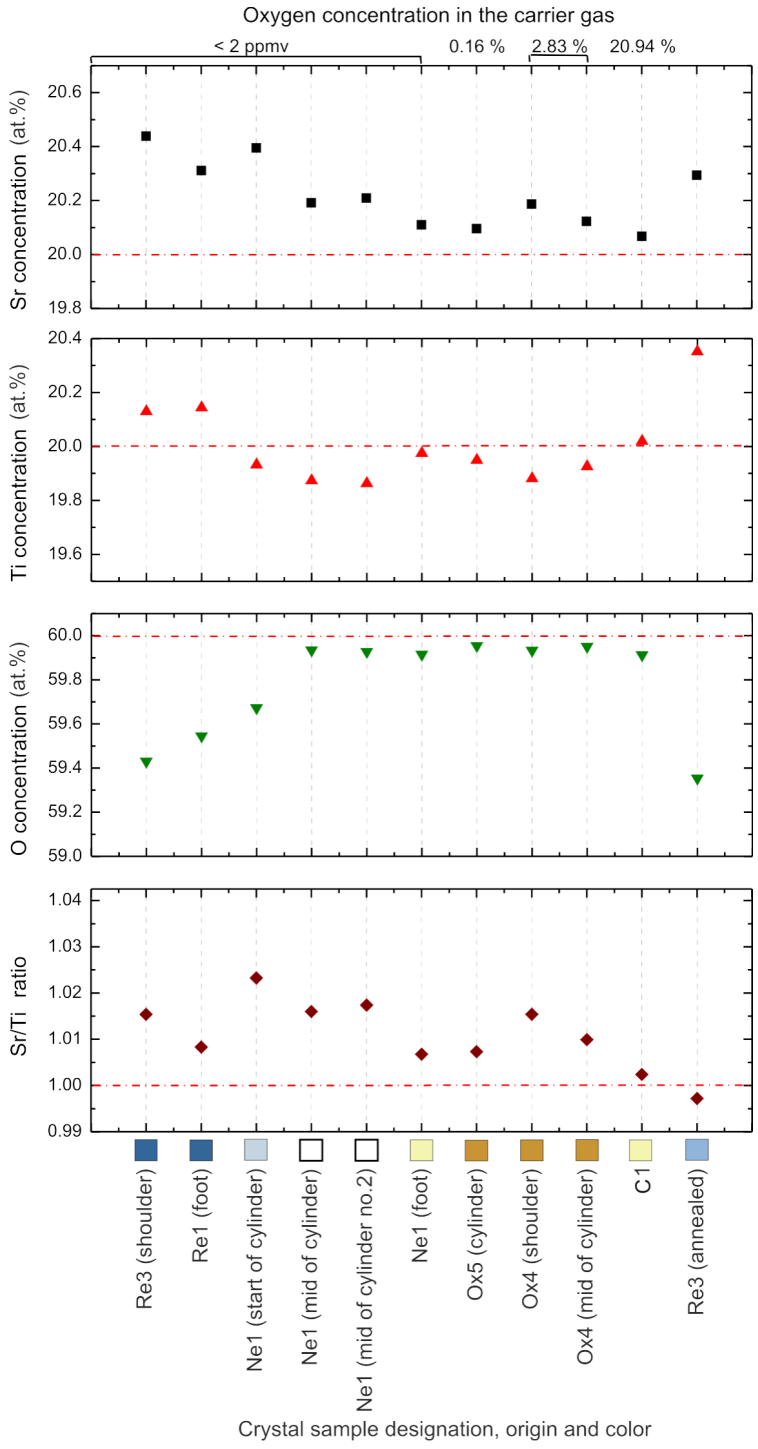

Figure 6.2.9.: Differences in composition plotted for colored and colorless TSSG crystals. The compositions of crystal T1 (grown at high temperature gradient and below 1813 K in air, see Ref. [31]) and of an annealed sample of crystal Re3 (1923 K for 10 h in air) are shown additionally. (Taken from Ref. [30]).

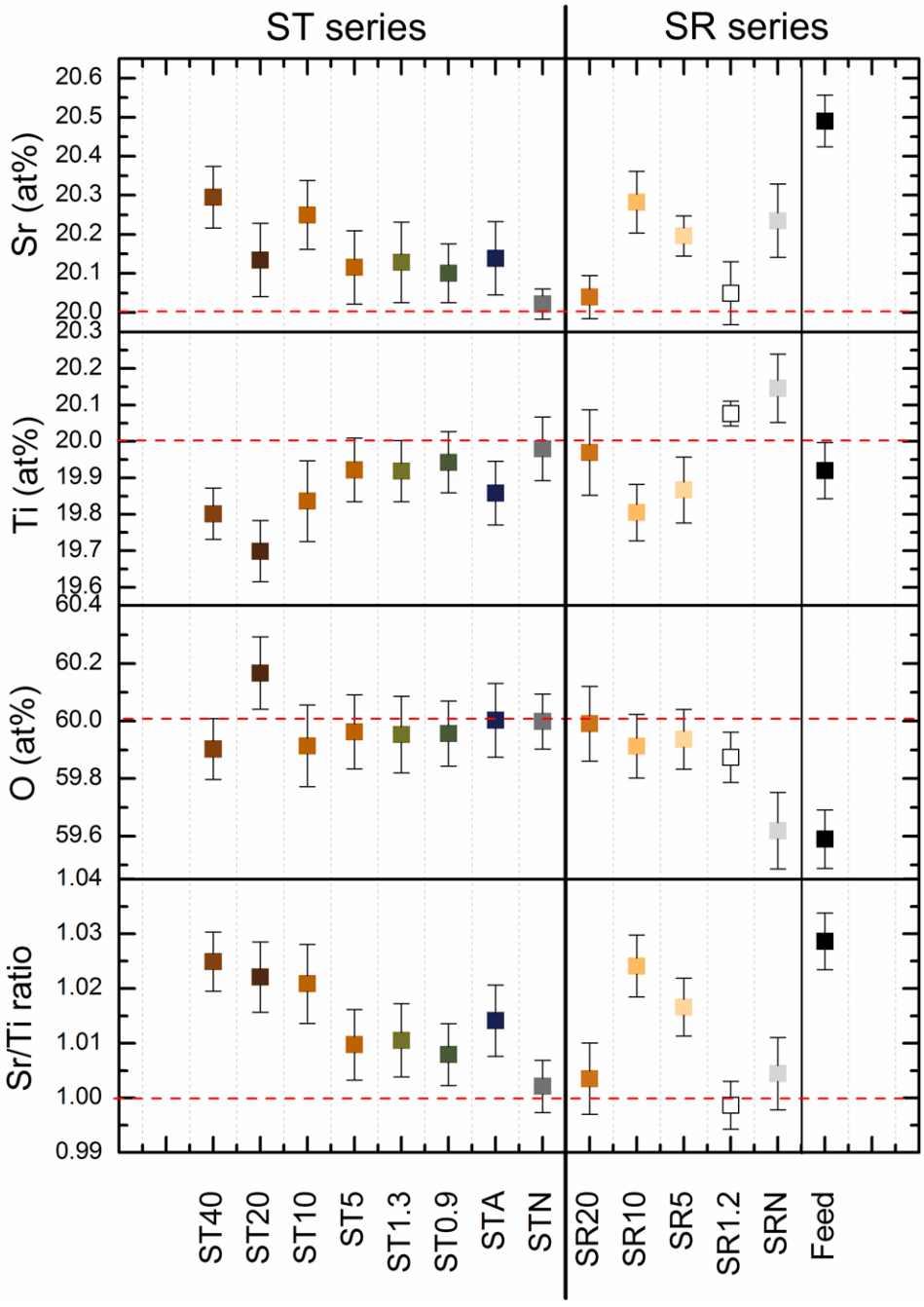

Figure 6.2.10.: Chemical compositions of selected crystal samples of the two series (ST and SR). The concentrations for Sr and Ti have been measured, O and Sr/Ti were calculated. The color of the squares indicates the fiber coloration. For comparison the Sr, Ti and O concentrations of stoichiometric STO are displayed by the red dashed lines. (Taken from Ref. [77]).

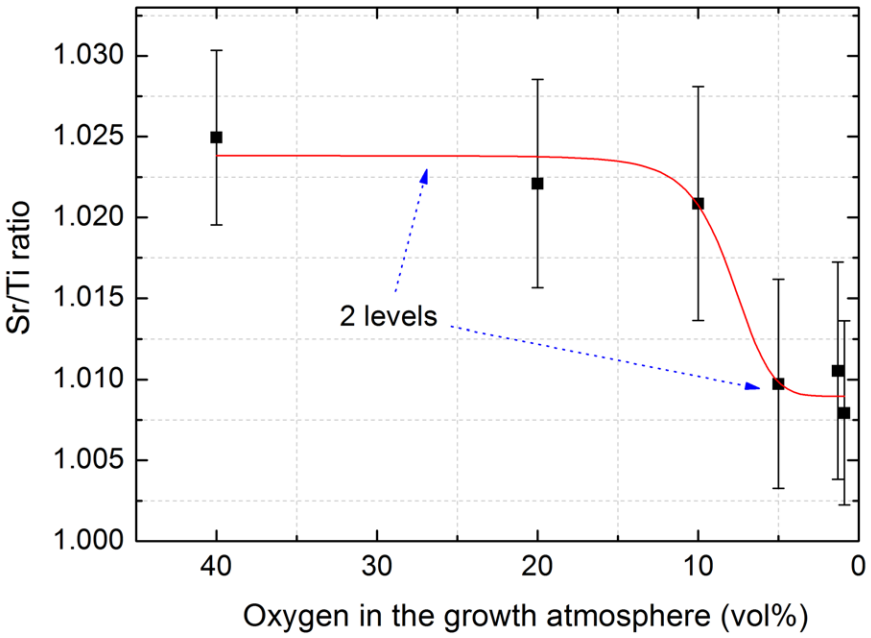

Figure 6.2.11.: Plot of the Sr/Ti ratios for the crystals ST40, ST20, ST20, ST5, ST1.3 and ST0.9. The red line is a sigmoidal fitted guide to the eye through the data points which indicates to plateaus of more or less steady Sr/Ti ratios. (Taken from Ref. [77]).

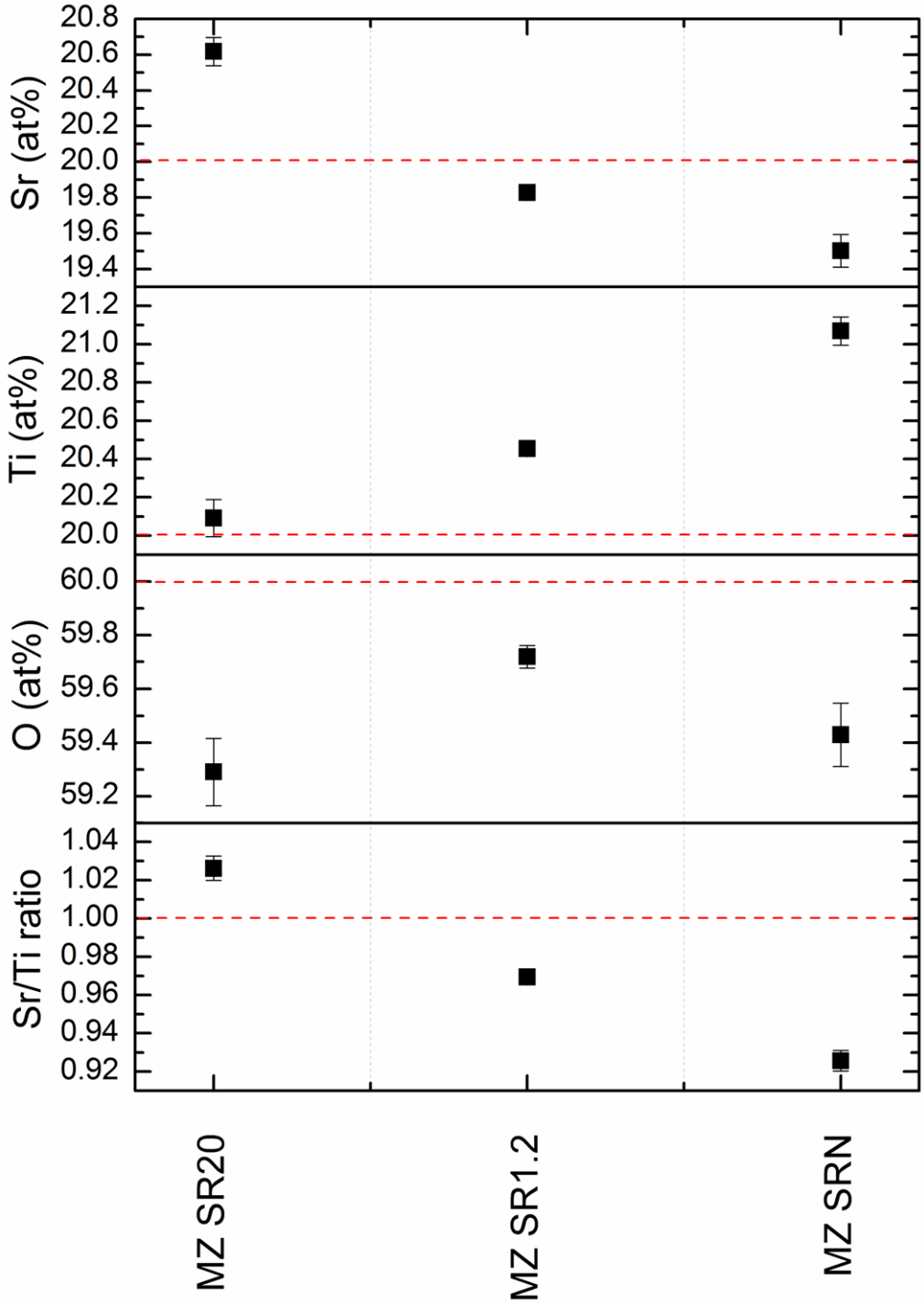

Figure 6.2.12.: Chemical compositions of quenched melt zones (MZ) after the growth runs in high (MZ SR20), low (MZ SR1.2) and very low (MZ SRN) oxygen concentrations in the growth chamber. (Taken from Ref. [77]).

6.3. Summary

The top-seeded solution growth method from TiO_2 rich melts at temperatures below 2013 K is suitable to grow spiral-free $SrTiO_3$ bulk single crystals exceeding one inch in diameter and length. A sufficient oxygen partial pressure is required to avoid growth instabilities. If the oxygen partial pressure is too low, oxygen vacancies form, which then increase the free carrier concentration and lower the IR transmission. But the crystals grown in Ar with 0.16 vol% or more O_2 added showed a strong brown coloration. Crystals which were grown in a "neutral" atmosphere (argon) show large areas which are nearly colorless.

A variety of single crystalline $SrTiO_3$ fibers have been grown by the LHPG method to determine the influence of the oxygen partial pressure in the growth atmosphere and the composition of the feed rod on their coloration. The crystals grown in oxygen rich conditions (between 5 and 40 %vol) are typically brown. Decreasing oxygen partial pressure leads to lighter tints (less coloration). Growth at very low oxygen partial pressures results in blue/black tints. By using feed rods with Sr-excess in an atmosphere containing about one vol% oxygen, it was possible to grow colorless STO crystals directly.

STO crystals grown with an oxygen poor atmosphere show very little or no absorption in the 400-500 nm range. As discussed in chapter 8, this brown coloration is caused by light scattering at nano-voids which are probably formed by the combination of oppositely charged Sr and O vacancies. Since the formation energy of Sr vacancies is about 1.8 eV higher in reducing than in oxidizing atmospheres, the Sr vacancy concentration will be much lower for oxygen poor conditions and fewer clusters will form. Increasing the concentration of Sr in the feed rods for LHPG also reduces this nano-void formation. Both series of experiments indicate that it seems to be possible to find growth conditions that will result in (nearly) colorless crystals, though the differences in the setups and methods are rather large and the conditions that produce colorless STO by the LHPG method are not easily transfered to bulk crystal growth methods from the melt. The correct atmosphere also appears to be required to produce stoichiometric crystals.

Acknowledgments

I want to thank Dr. Christo Guguschev for growing the TSSG crystals, Franz Kamutzki for growing the LHPG fibers and Dr. Rainer Bertram for the ICP-OES measurements. Also I am grateful to Thomas Wurche for cutting the samples, Manuela Imming-Friedland and Viola Lange for the chemo-mechanical polishing and to Dr. Uta Juda for the EPD measurements.

7. Blue coloration of $SrTiO_3$

7.1. Introduction

Strontium titanate grown by the Verneuil method appears black in the as grown state and has to be annealed to become colorless (see Fig. 2.3.2). Thinner samples reveal that the color is a dark shade of blue. The spectrum of an as grown crystal shows that this color is produced by free carrier absorption, which depends on the wavelength as $\alpha_{fc} \propto \lambda^2$ (see Fig. 2.3.2, the free carrier absorption is described by equation 4.2.2). Free carriers absorb primarily in the red and infrared wavelengths, resulting in a blue crystal. The same effect is seen for conductive crystals doped with, for example, Nb, or crystals grown in an oxygen poor atmosphere (see Fig. 7.1.1). For the oxygen deficient samples, the coloration reduces and fades upon annealing.

All n-type $SrTiO_3$ crystals also show a broad peak around 2.4 eV (517 nm), whether they are oxygen deficient or have been doped with one of a variety of metals (Kulagin et al. reported this peak for crystals doped with Mn, Co, Ni, Sm, Pr, Tm or Nd [52, 146] and Wild et al. reported it for crystals doped with Fe, Ni, Nb and for reduced undoped crystals [50]. See Figs. 7.1.1 a) and b). This indicates that the absorption peak is tied to a fundamental property of STO and not to a dopant or impurity complex.

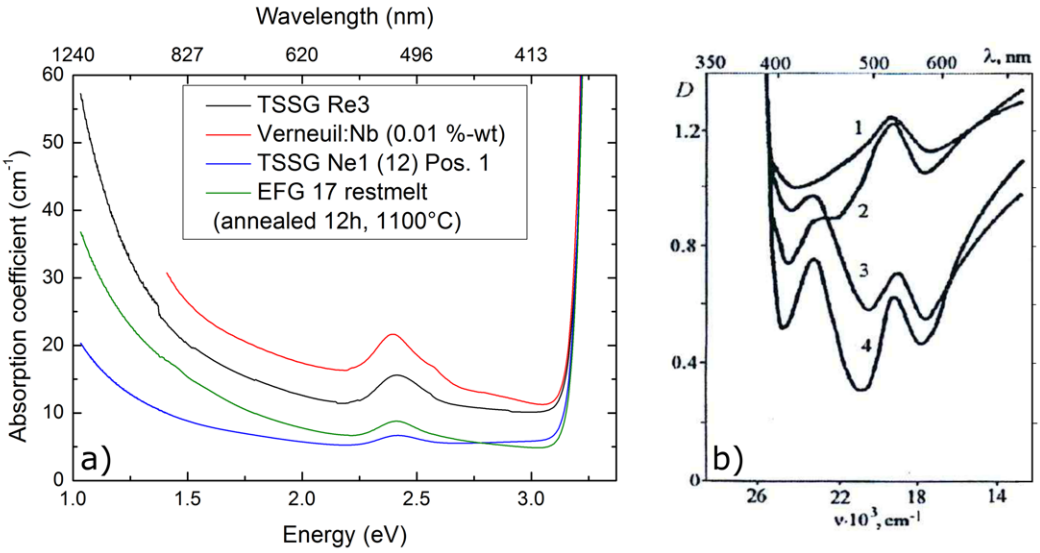

Figure 7.1.1.: a) Comparison of the spectra of several blue colored $SrTiO_3$ crystals. b) Crystals grown by Kalugin et al. doped with (1) Sm, (2) Pr, (3) Nd, and (4) Tm (spectrum is taken in units of optical density which is equivalent to absorbance. Taken from Ref. [52]).

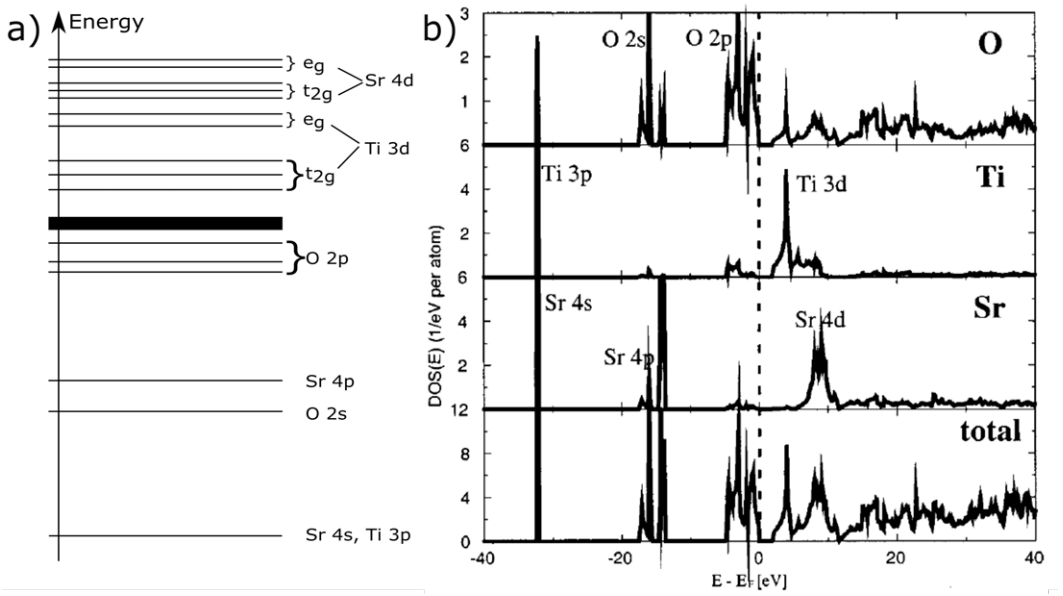

Figure 7.2.1.: a) Relative positions of atomic orbitals in the band structure. b) density of states, as determined by Van Benthem et al. (taken from Ref [1]).

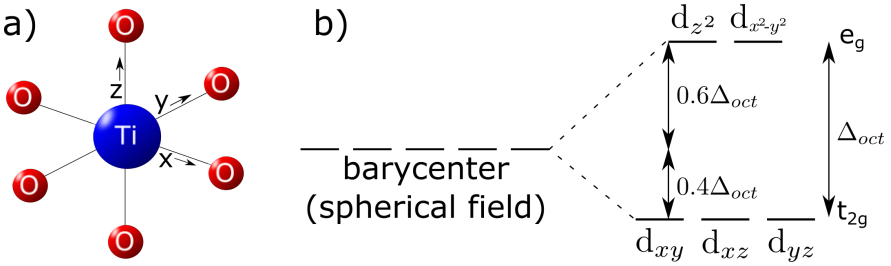

Figure 7.2.2.: Octahedral crystal field splitting for a TiO_2 complex. a) the geometry of the complex and b) the splitting of the 3d orbitals relative to the barycenter or spherical field.

7.2. Review of literature data

When examining the band structure of $SrTiO_3$ (see Fig. 7.2.1), it becomes clear that the top of the valance band is mostly made up out of O 2p orbitals and the bottom of the conduction band is mostly made up out of Ti 3d orbitals [1]. These Ti orbitals are split into t_{2g} (d_{xy}, d_{xz} and d_{yz}) and e_g (d_{z^2} and $d_{x^2-y^2}$) orbitals by the octahedral crystal field splitting (see Fig. 7.2.2), with the e_g orbitals higher in energy since they point directly at the oxygen ions whose negative charge repels the electrons. The density of states between these two groups of orbitals is low (see Fig. 7.2.1 c), which suggests that electrons have to be excited to move between the two parts of the conduction band, which may happen by photon absorption.

In rutile TiO_2, the titanium and oxygen ions also form octahedra, resulting in a similar band structure where again the oxygen 2p orbitals form the top of the valence band and the titanium 3d t_{2g} orbitals form the bottom of the conduction band. When rutile is reduced, it gets a blue coloration due to free carrier absorption. Reduced rutile shows two peaks, one at 2.9 and one at 2.3 eV, which Khomenko et al. investigated with UV/VIS/IR spectroscopy and electron paramagnetic resonance and assigned to the $t_{2g} \rightarrow e_g$ transition [147] (the e_g levels in rutile are split due to the Jahn-Teller distortion). The assignment was made because

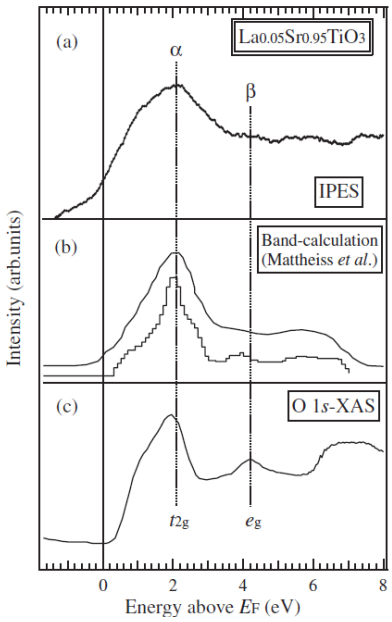

Figure 7.2.3.: (a) IPES spectrum of $La_{0.05}Sr_{0.95}TiO_3$ measured at $E_K = 100$ eV. (b) Energy band DOS calculated by Mattheiss et al. [149] (c) O 1s XAS spectrum of $SrTiO_3$. The separation between the t_{2g} and e_g peaks is about 2.2 eV. (Taken from Ref. [148])

of the match to electrical transitions from the valance band to the e_g levels and because the 2.9 eV and 2.3 eV peaks narrowed and shifted to higher energy when the sample was cooled down.

Unoccupied states in the conduction band can be studied by inverse photoemission spectroscopy (IPES). For IPES, a narrow beam of electrons with a well defined energy is aimed at the sample. These electrons can enter into high energy unoccupied states in the conduction band and then decay to lower lying unoccupied levels. Some of these transitions emit photons and these are recorded in an energy spectrum. Baba et al. performed IPES and X-ray absorption spectroscopy (XAS) measurements on La doped STO crystals at 25 K ($La_{0.05}Sr_{0.95}TiO_3$ and $La_{0.1}Sr_{0.9}TiO_3$) [148]. They found a splitting of just over 2.2 eV between the t_{2g} and e_g states (see Fig. 7.2.3). This is lower than the peak energy in the optical spectrum, but the values are close together and the peak positions are slightly ambiguous in the IPES and XAS spectra.

7.3. Results and discussion

To determine whether the 2.4 eV peak in conductive STO is caused by a transition between the Ti e_g and t_{2g} bands in the conduction band, low temperature spectroscopy measurements were performed on a wafer cut from crystal Re3 and a Nb doped Verneuil grown wafer (0.01 wt%, provided by CrysTec GmbH, see section 3.1.1 for experimental details). The results are shown in figure 7.3.1. The baseline of the spectra was shifted so all the spectra of one series have the same value at a photon energy of 3 eV. As can be seen from figure 7.3.1 a) and b), which show spectra over the whole temperature range, the 2.4 eV peak shifts to higher energies when the temperature is lowered. Figure 7.3.1 c) and d) compare the room temperatue and 4 or 5 K spectrum, respectively. Here the shift to higher energies is again clear and it is also apparent that the peak broadens with rising temperature.

Additionally, high temperature UV/VIS spectra were measured for crystal Re3 (see section 3.1.2), some of which are shown in figure 7.3.2. The peak is visible up to about 873 K, then it becomes obscured by the absorption of the free carriers. It broadens with rising temperature and the peak position becomes more and more unclear as the temperature rises.

The shift of the 2.4 eV peak and the band gap with temperature are compared for both crystals in figure 7.3.3 (the band gaps were determined as discussed in section 2.6.2). The peak and the band gap shift by approximately the same amount of energy from 4 K to 573 K. Above that temperature, the position of the peak becomes difficult to determine as it broadens strongly and is increasingly obscured by the rising free carrier absorption.

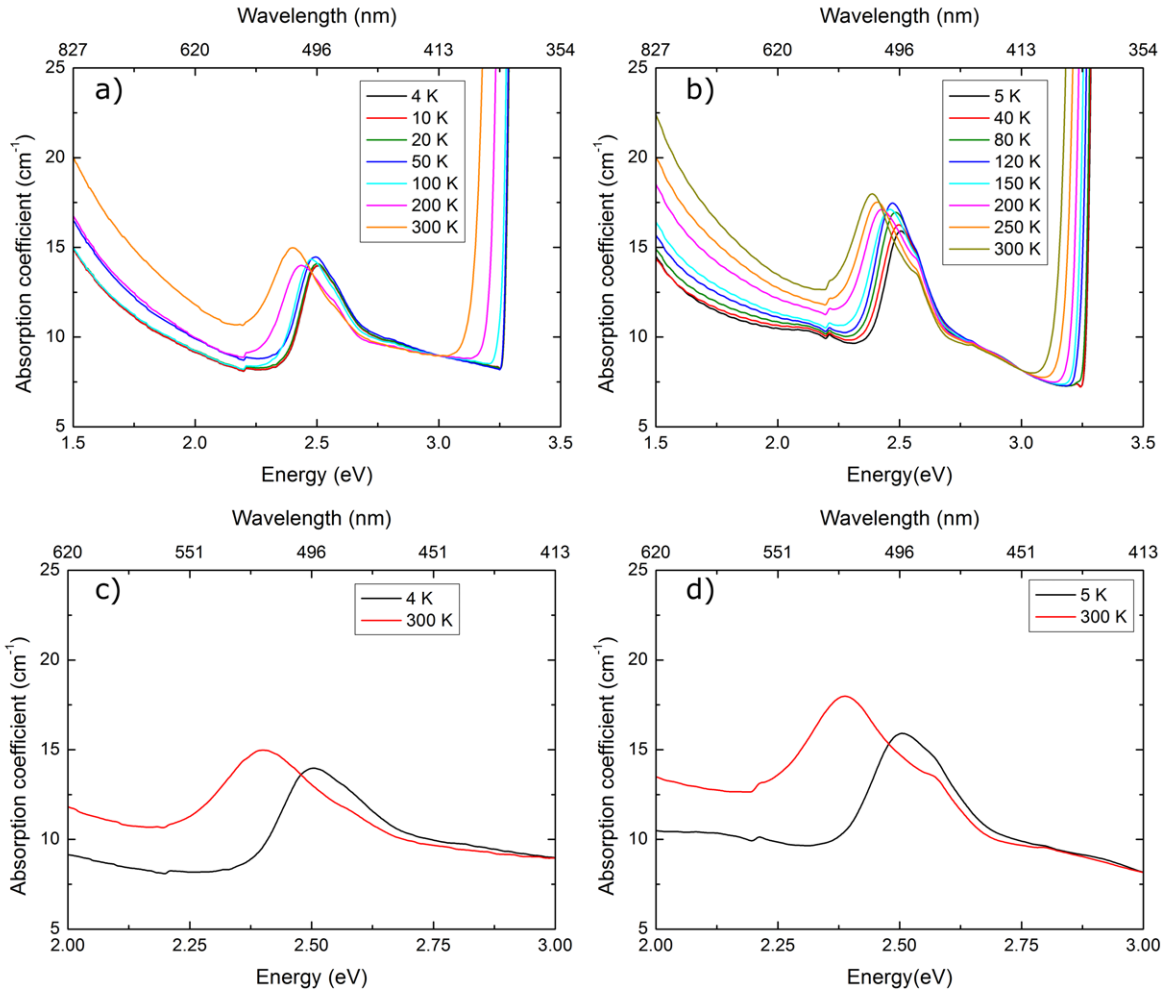

Figure 7.3.1.: Low temperature spectra of crystal Re3 (a and c) and a Nb doped Verneuil grown crystal (b and d). Figure a) and b) show spectra over the full temperature range from room temperature to 4 or 5 K, where it is clear to see that the peak shifts to higher energies. c) and d) show a part of the spectra at room temperature and 4 or 5 K, respectively. Here the narrowing of the absorption peak is clearly visible. The spectrum of the Nb doped crystal shows two convoluted peaks that separate more at higher temperature. The second peak is probably due to transitions involving Nb.

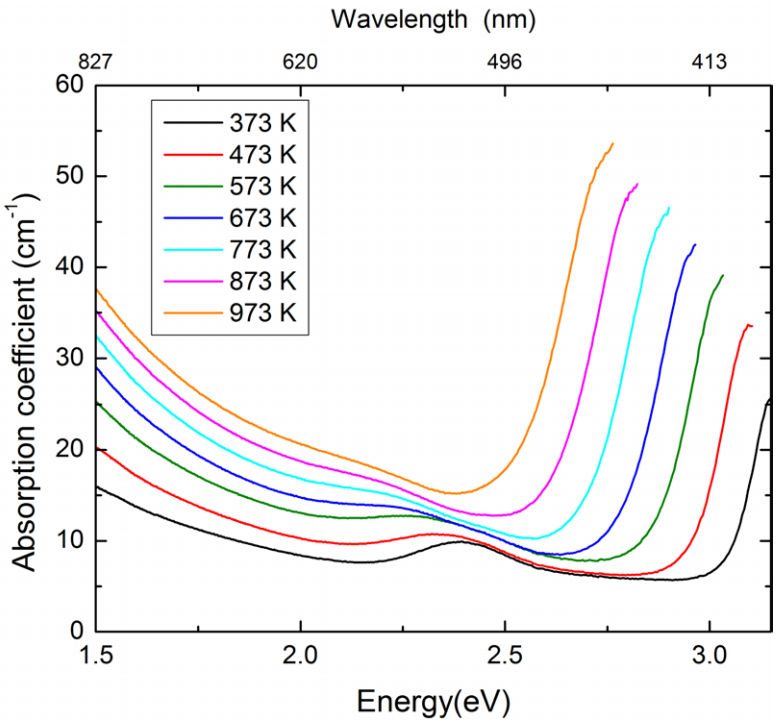

Figure 7.3.2.: High temperature UV/VIS spectra of crystal Re3. The position of the $t_{2g} \rightarrow e_g$ transition peak shifts to lower energy with increasing temperature. The position of the peak becomes less and less clear as it broadens and the free carrier absorption rises.

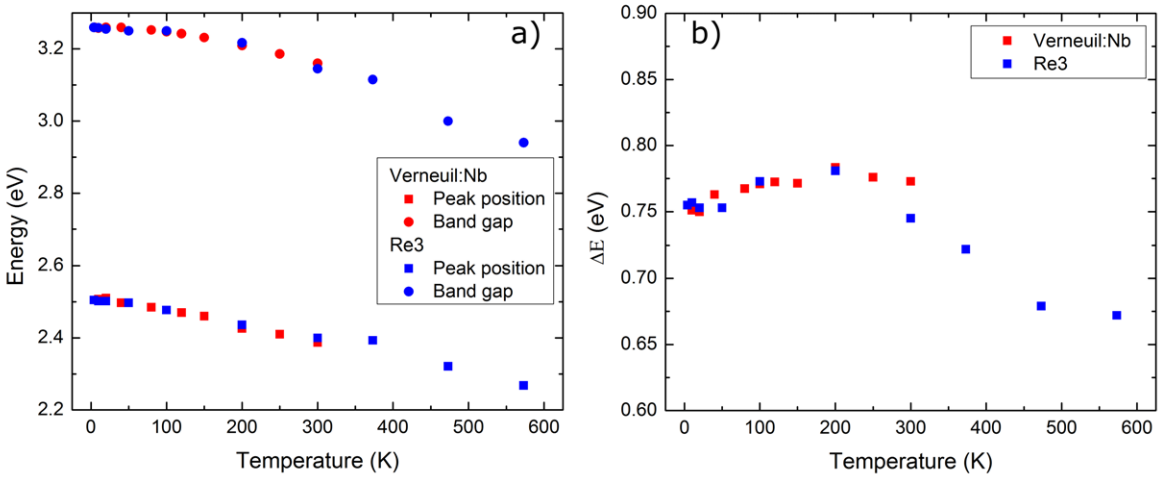

Figure 7.3.3.: a) Position of the band gap and the $t_{2g} \rightarrow e_g$ absorption peak. b) distance between the band gap and the absorption peak. The peak appears to shift about as much as the band gap and the variation in the distance is more or less within experimental error.

7.4. Summary

n-type conductive STO crystals owe their blue color to free carrier absorption and show an absorption peak around 2.4 eV at room temperature. This peak broadens with rising temperature and has a similar temperature dependence as the band gap. Based on these observations, the IPES and XAS measurements reported by Baba et al. [148] and the band structure determinations of Van Benthem et al. [1], this 2.4 eV absorption can be assigned to a transition within the Ti 3d orbitals in the lower conduction band, which are split by crystal field splitting.

Acknowledgements

I would like to thank Martin Naumann for the high temperature spectral measurements and Mike Pietsch and Dr. Klaus Irmscher for their help with the low temperature spectra. Also I am grateful to Thomas Wurche for cutting the samples, Manuela Imming-Friedland and Viola Lange for the chemo-mechanical polishing and to Dr. Uta Juda for the EPD measurements.

8. Brown coloration of nearly stoichiometric $SrTiO_3$ crystals

8.1. Introduction

Several growth methods were used in attempts to produce $SrTiO_3$ with a higher quality than can be provided by the Verneuil method. This includes crystal growth techniques like optical floating zone [28, 150], edge-defined film-fed growth [59] or top-seeded solution growth (TSSG) [30, 31, 61]. Light to dark brown crystals were produced by all these methods when the crystals were grown in an atmosphere with a significant oxygen concentration. Brown STO crystals have also occasionally been produced by the Verneuil method [49]. Annealing colorless STO in oxygen has also been reported to cause a brown color [28, 151].

Ardila et al. [81] and Nabokin et al. [28] speculated that the brown coloration is due to a variation in the local oxygen concentration, while Kawanabe et al. proposed that the loss of Sr would cause the brown coloration [150]. Quinian et al. [49], Wild et al. [50] and Jalan et al. [151] have attributed the brown coloration to iron in the crystals. Fe is a common impurity in many Verneuil grown crystals, making this a reasonable suggestion. However, all these previous investigations were purely phenomenological and lack an explanation of the microscopic origin of the brown coloration.

In this chapter, results of spectroscopic and transmission electron microscopy (TEM) investigations into the origin of the brown coloration are presented. First crystals with almost stoichiometric composition, as determined by inductively coupled plasma optical emission spectroscopy (ICP-OES), were selected to rule out off-stoichiometry effects. Significant deviations from the stoichiometric composition are possible in STO [30, 89, 92]. Later an LHPG crystal with a significant Sr excess and a MPD grown crystal which showed color changes upon annealing were investigated as well.

Based on transmission electron microscopy studies, we propose that the brown coloration of the nearly stoichiometric crystals is due to Mie scattering caused by nanometer sized voids which form by the combination of Sr and O vacancies. The Sr and O vacancies are present in sufficiently high concentrations at growth temperature and attract each other because of their opposite charge[94], resulting in neutral di-vacancies. These di-vacancies probably form the nucleus of the nano voids, which grow by combination with more vacancies. For the crystal with Sr excess, Sr''_{Ti} anti site defects are probably involved as well.

The investigations of the stoichiometric crystals were published in CrystEngComm (Ref. [64]).

8.2. Results

8.2.1. Element analysis

The results of ICP-OES measurements are shown in table 8.2.1. They show that large deviations from stoichiometry are not present for both TSSG crystals C1 and C2 (the standard deviation is typically below 0.4 wt%), which are known to be possible in STO (see section 2.4) and seen for crystal ST40 which shows an Sr surplus and Ti deficiency (see also Fig. 6.2.10).The

measurements are, however, not accurate enough to investigate point defect concentrations. The iron content of crystals C1 and C2 was below the respective detection limits of 10 and 40 wt ppm. For crystal C1 the concentrations of Al, Ni and Zr were determined to be under the detection limits of 40, 25 and 25 wt ppm, respectively.

Table 8.2.1.: ICP-OES results for crystals C1, C2, and ST40. C1 and C2 are grown by the TSSG method and ST40 by the LHPG method.

Crystal	**[Sr](wt%)±σ**	**[Ti](wt%)±σ**	**[Fe](ppm)**	**[Sc] (ppm)**	**Growth method**
C1	47.84±0.37	26.08±0.39	<10	-	TSSG
C2	48.10±0.39	26.09±0.20	<40	-	TSSG
ST40	48.26±0.43	25.73±0.21	-	-	LHPG
Stoichiometric	47.75	26.09	-	-	-

8.2.2. Optical absorption

Room temperature absorption spectra of both top-seeded solution grown crystals are presented in figure 8.2.1, with the spectrum of the colorless Verneuil grown crystal for comparison. The spectra of C1 and C2 are qualitatively comparable and show a broad absorption that convolutes with the fundamental absorption. The absorption is higher for crystal C2, which was grown with an afterheater, which indicates that the temperature gradient at the liquid-solid interface of the growing crystal (perpendicular to the growth interface) and the cool-down rate affect the coloration.

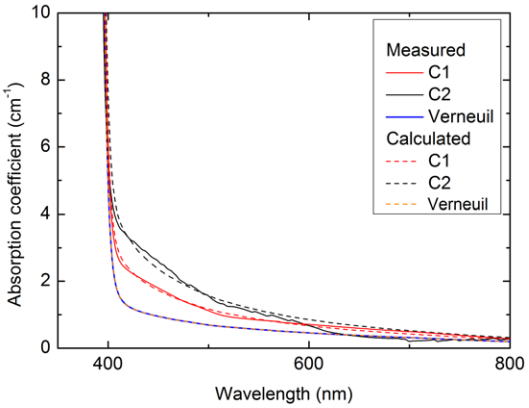

Figure 8.2.1.: Room temperature absorption spectra of TSSG crystals and of a colorless Verneuil crystal for comparison. The dashed lines are the spectra calculated from the light scattering theory. (Taken from Ref. [64])

The low temperature spectra in figure 8.2.2 a) show little change down to 5 K. The band gap shifts from 3.15 eV at room temperature to 3.27 eV at 5 K, which is the same value as found for a Verneuil grown crystal [114]. The broad low wavelength absorption, however, remains unchanged and does not broaden or narrow when the temperature is changed. This makes an impurity effect or an effect caused by point defects unlikely, which would not have been detected by HRTEM.

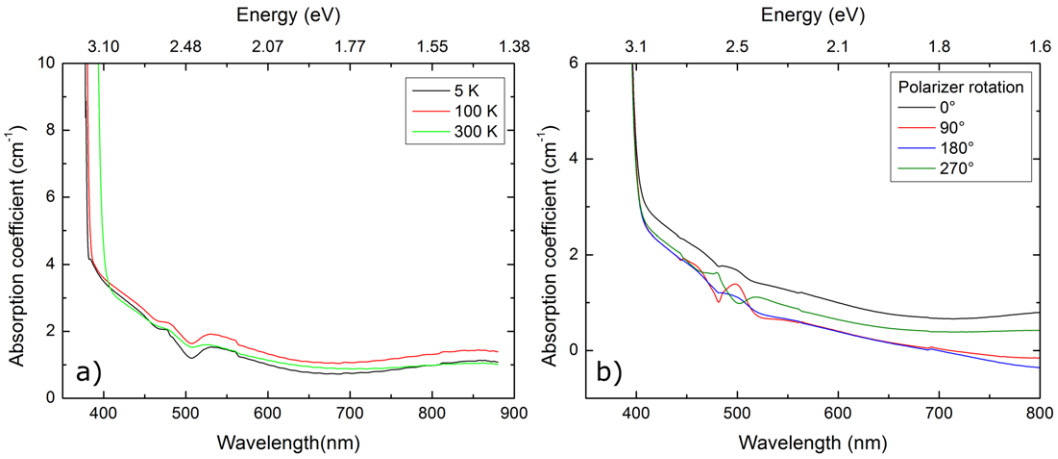

Figure 8.2.2.: a) Low temperature spectra of crystal C1. The broad absorption does not change when the sample is cooled from room temperature to 5 K. The feature around 500 nm is caused by a polarization effect from the combination of the cryostat windows, the polarized spectrometer beam, stress polarization in the sample and an order sorting filter which is switched into the optical path in this wavelength. b) Room temperature spectra of crystal C1 in the cryostat with an additional polarizer in the spectrometer beam before the cryostat. The feature around 500 nm changes when the polarizer is rotated, showing that it is an artifact of the set up.

8.2.3. Transmission electron microscopy

TEM investigation of brownish top-seeded solution grown $SrTiO_3$ crystals reveals the presence of nanometer sized objects in the $SrTiO_3$ matrix (see Fig. 8.2.3 (a)). In STEM Z-contrast images (see Fig. 8.2.3 (b)) the observed objects show the same high resolution pattern as the surrounding $SrTiO_3$ matrix next to them. A crystalline phase with a different crystal structure can therefore be excluded. Also, the objects appeared with reduced intensity compared to the $SrTiO_3$ matrix. This points to a reduced effective thickness of the probed material and is thus a hint that the nanometer sized objects are empty volumes in the $SrTiO_3$ crystal. In order to confirm this hypothesis we performed an aberration corrected HRTEM investigation of brownish $SrTiO_3$ crystals along the [100] projection (see Fig. 8.2.4 (a)). In this projection Sr-, Ti-O- and O-atomic columns are seen separately and their position can be identified in the experimental image by comparing with multi-slice image simulations (the positions are marked in Fig. 8.2.4) [152]. For the HRTEM image shown in figure 8.2.4 (a) a defocus of $df = +11$ nm (over-focus) yielded the best agreement between the experimental and simulated high resolution pattern of the $SrTiO_3$ matrix for the used value of the spherical aberration of $C_s = -10\mu$m (see inset in Fig. 8.2.4 (a)). Looking carefully at the high resolution TEM pattern, we find that in the region of the object the intensity of all three atomic columns differs from that of the $SrTiO_3$ matrix. More precisely: the Sr- and Ti-O-atomic columns/O-atomic columns appear with a higher/lower intensity in the region of the object than in the surrounding $SrTiO_3$ material next to it, respectively (see Fig. 8.2.4 (b)). A comparison of the experimental and simulated images revealed that the HRTEM pattern of the object matches to that of $SrTiO_3$ of 3.1 nm thickness (see Fig. 8.2.4 (e)) while the surrounding matrix next to the object exhibits a thickness of 4.7 nm, see figure 8.2.4 (g). The reduced thickness along the projection direction of 1.6 nm (= 4 unit cells along [100]) agrees well with the lateral dimensions of the considered object of about 2.0 nm. Assuming that the objects

have an approximately spherical shape we can therefore conclude that the objects observed in brownish $SrTiO_3$ crystals are nano-voids.

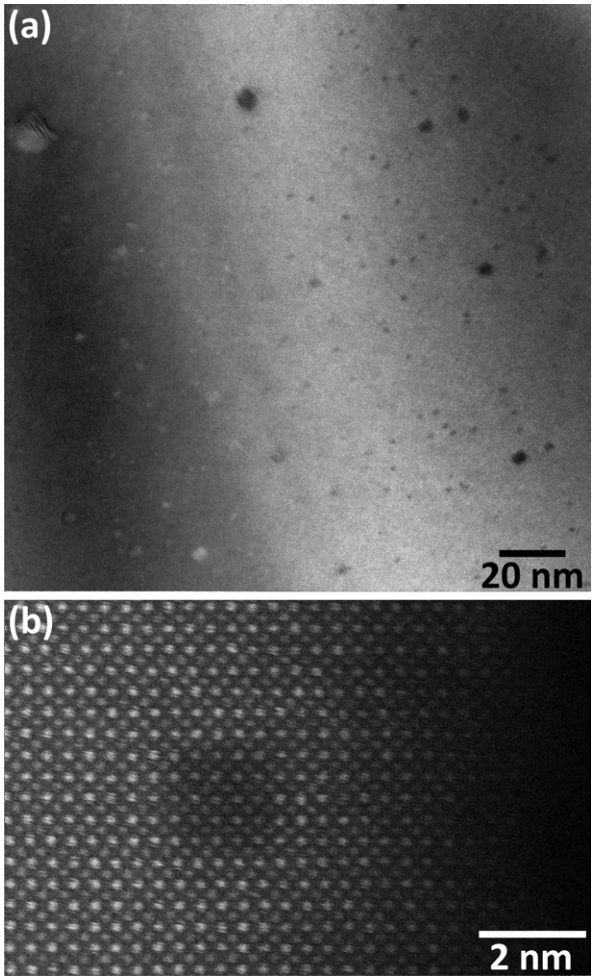

Figure 8.2.3.: (a) TEM image of a brownish $SrTiO_3$ crystal (sample C2) with a representative size and density distribution of nano-voids in the $SrTiO_3$ matrix. The thickness of the TEM sample in the displayed region is approximately 200 nm. (b) High resolution STEM Z-contrast image of a 1.6 nm wide nano void from the same sample. (Taken from Ref. [64])

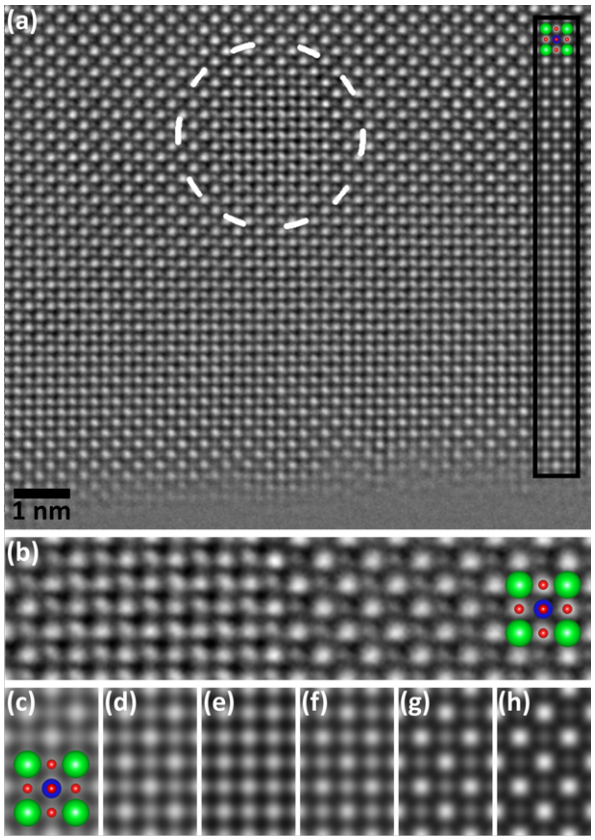

Figure 8.2.4.: (a) Aberration corrected HRTEM image of a 2.0 nm wide nano-void in a brownish $SrTiO_3$ crystal (sample C2) along the [100] projection. The inset with the black frame is a HRTEM contrast simulation of $SrTiO_3$ according to the experimental imaging conditions (C_s=-10 µm, df = +11 nm) with increasing thickness from the bottom (2.0 nm) to the top (5.5 nm). (b) shows a magnified view of (a) taken from the void region (left part of the image), indicated by the dashed white circle in (a), and from the $SrTiO_3$ matrix (right part of the image) next of the cluster. (c-h) are HRTEM contrast simulations of $SrTiO_3$ according to the aforementioned imaging conditions and for a specimen thickness of (c) 1.6 nm, (d) 2.3 nm, (e) 3.1 nm, (f) 3.9 nm, (g) 4.7 nm and (h) 5.5 nm, respectively. The overlays in (a-c) are a schematic model of $SrTiO_3$ seen along the [100] direction, whereby green, blue and red balls denote Sr, Ti and O atoms, respectively. (Taken from Ref. [64])

An estimation of nano-void size distribution from TEM images is summarized for crystal C2 in figure 8.2.5. In total, the approximate densities found were 10^{16} cm^{-3} objects with a diameter between 0 and 5 nm, 10^{15} cm^{-3} objects between 5 and 10 nm diameter, 10^{14} cm^{-3} objects between 10 and 30 nm diameter and about 10^{12} cm^{-3} objects with a diameter larger than 30 nm. These size densities were described by a lognormal distribution (the natural logarithm of the variable has a normal distribution):

$$f(s) = \frac{A}{\sqrt{2\pi}s\sigma \exp\left(-\frac{1}{2}\left(\frac{\ln(s)-\mu}{\sigma}\right)^2\right)} \tag{8.2.1}$$

where s is the void diameter in nm, A is the total number of objects per cm^3, σ is the standard deviation and μ is the mean. The estimated distribution was used to calculate the theoretical spectra (see below).

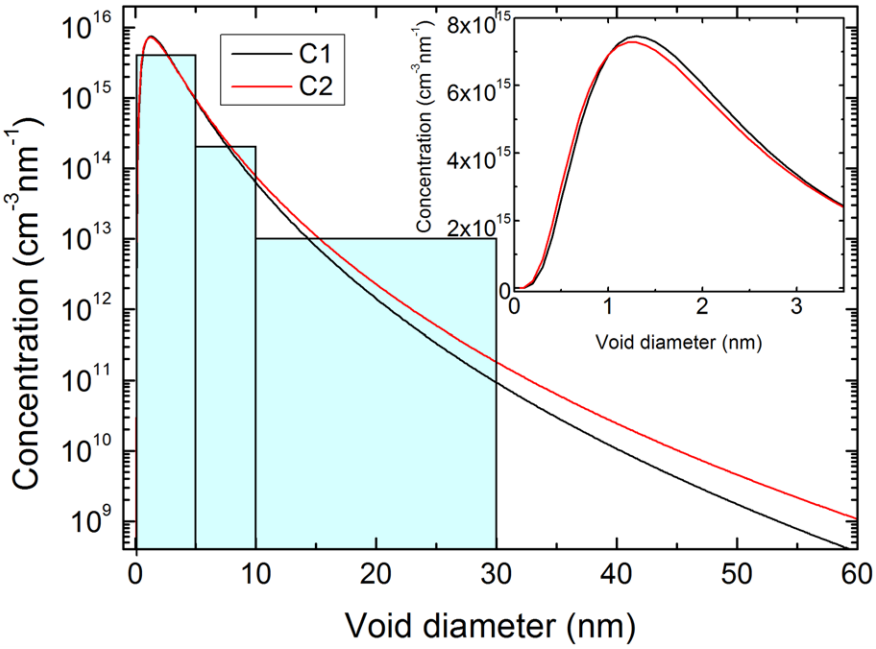

Figure 8.2.5.: The bar plot shows the approximate sum density of nano-voids in the given size range. The lines represent the lognormal distribution fitted to the size density and adjusted until the calculated spectra matched the measured spectra (see Fig. 8.2.1 and sections 8.2.3 and 8.3.1). The inset shows the small diameter range on a linear scale so it becomes apparent that C1 has more small voids than C2. (Taken from Ref. [64])

The Verneuil grown crystal also showed some nano-voids, mainly with a radius in the 10-30 nm range. Very few nano-voids in other size ranges were detected. The difference to the investigated TSSG crystals is that the integrated density found in the 10-30 nm range is only 10^{12} to 10^{13} cm^{-3}, which is at least one order of magnitude lower compared to the brownish TSSG crystals.

In the LHPG sample ST40, nano-voids were found as well, but almost exclusively in the 1-5 nm size category. The typical diameter was 2 nm and the average density was $\approx 10^{15}$ cm^{-3} (see Fig. 8.2.6).

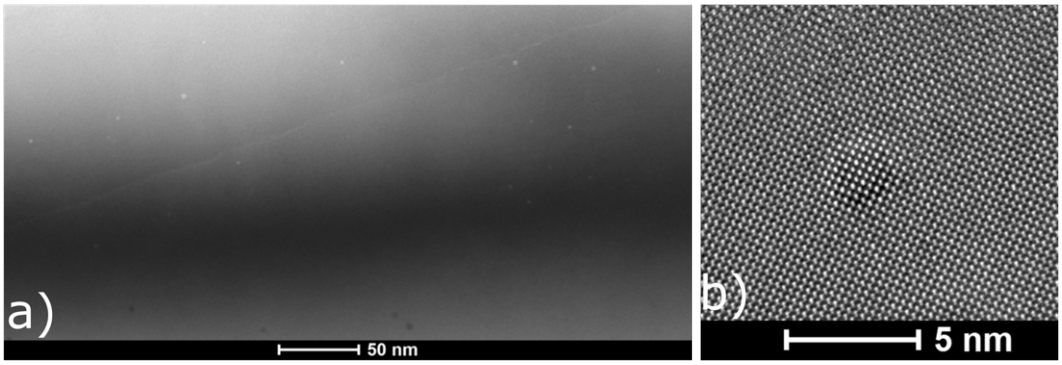

Figure 8.2.6.: a) TEM bright field overview of sample ST40. Almost all nano-voids are in the 1-5 nm size category with a typical diameter of 2 nm. b) detail of a typical nano-void. (Taken from Ref. [64])

8.3. Discussion

As mentioned above the low temperature optical absorption spectra showed little change down to 5 K besides the increase of the band gap energy. The broad low wavelength absorption does not change when the temperature is altered. This would be unusual for absorption by point defects or impurities. Also, the concentration of all impurities measured was below the detection limit.

The brown coloration discussed by Wild et al. [50] was observed in $SrTiO_3$ crystals doped with Fe. These crystals were initially clear and colorless at room temperature, but became brown after annealing in hydrogen gas or vacuum with rapid cooling. The effect could be reversed when the crystals were annealed, in both reducing and oxidizing atmospheres, and cooled slowly. When examining the spectra reported by Wild et al. [50], there is a clear difference between the effect reported there and the brown coloration observed here. The curve shape in the spectra is different for anneals above 1073 K. Also, the absorbance reported for the 2.9 eV peak in that publication converts to an absorption coefficient of about 25 to 42 cm^{-1} (for the temperatures where it is present). The crystal is reported to be doped with 650 wt ppm Fe. The crystals investigated here have $<$10 wt ppm Fe, which was the detection limit of the inductively coupled plasma optical emission spectroscopy method used. Since the absorption coefficient depends linearly on the dopant concentration, the iron concentration in our crystals would have had to have been at least ten times higher to cause the absorption observed. We therefore conclude that the two effects are distinct from each other and offer an explanation based on light scattering at the nano-voids.

8.3.1. Light scattering calculations

Gustav Mie described the scattering and absorption of electromagnetic radiation at a spherical particle in a continuous dielectric medium by applying the Maxwell equations [101]. The extinction, scattering and absorption cross sections, σ_{ext}, σ_{sca} and σ_{abs}, are calculated from the complex dielectric functions of the particles and the medium and a size parameter $x = 2\pi r/\lambda$ with r the particle radius and λ the wavelength. The formulas are discussed in section 2.7. The absorption coefficient of the medium and the particles combined, α_{tot}, is given by:

$$\alpha_{tot} = \alpha_{medium} + \int N(r)\sigma_{ext}(r)dr \tag{8.3.1}$$

with α_{medium} the absorption coefficient of the medium, $N(r)$ the density of particles with radius r, and $\sigma_{ext}(r)$ the extinction cross section of particles with radius r.

This approach can be problematic when it is applied to particles that have a smaller extinction coefficient than the matrix ($k_{matrix} > k_{particle}$) since σ_{ext} can become negative, which is unphysical [103, 104]. Because the "particles" in the present case are empty volumes (as discussed below), they should not cause any absorption and the problem of negative extinction is solved by ignoring the absorption component. The calculated absorption coefficient was taken to be determined by the scattering only:

$$\alpha_{tot} = \alpha_{medium} + \int N(r)\sigma_{sca}(r)dr. \tag{8.3.2}$$

This description assumes spherical particles or spherical nano-voids. The scattering center density is estimated from the TEM investigation. The complex refractive index of $SrTiO_3$ was taken from Ref. [1] and for the nano-voids the refractive index and the extinction coefficient are taken to be 1 and 0 for all wavelengths.

Figure 8.3.1 (a) and (b) show the calculated extinction coefficients for nano-voids in $SrTiO_3$ with sizes ranging from 1 to 50 nm, neglecting the absorption of the host material. If the extinction coefficients is normalized to 100 % (Fig. 8.3.1 (a)) it becomes evident that the slope becomes less steep as the size of the voids increases, while the extinction cross section increases at longer wavelengths. The scattering intensity does depend on the nano-void size, which can be seen in the logarithmic plot in figure 8.3.1 (b). No nano-void size dependent absorption maximum is found and the extinction coefficients are very similar qualitatively. This means the calculated spectrum depends only on the combination of the size and density of the nano-voids. A low concentration of large voids could result in almost the same spectrum as a high concentration of small voids.

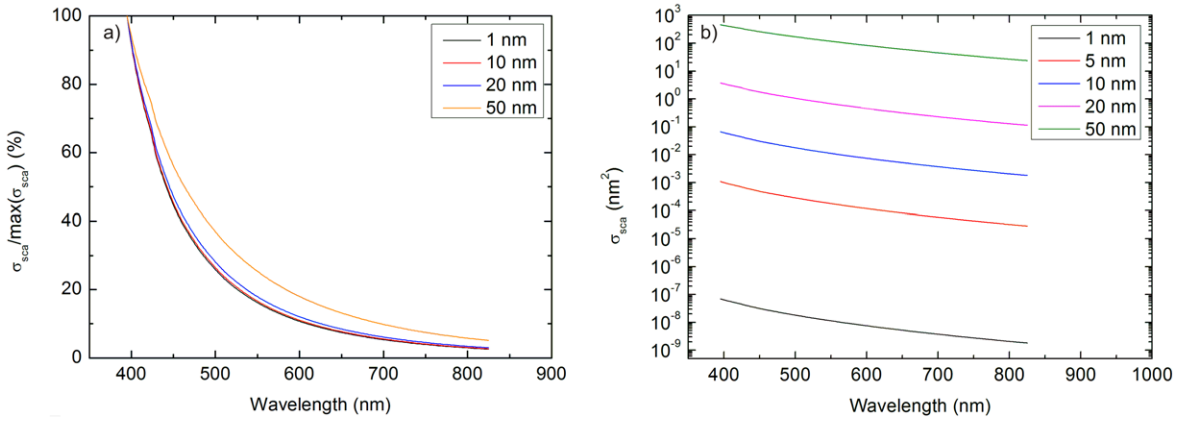

Figure 8.3.1.: Comparison of the calculated scattering spectrum of clustered vacancies with varying sizes. (a) The scattering cross sections are normalized to compare the curve shapes. (b) Logarithmic plot of the scattering cross sections. (Taken from Ref. [64])

To calculate the effect of nano-voids on the extinction coefficient of crystal C2 we use the void size density distribution estimated from our TEM investigation as an input (see Fig. 8.2.5). The size distribution is approximated by a lognormal distribution, as shown above. By iterative adjustment of the size distribution we were able to fit the experimentally measured extinction coefficient. For crystal C2 the best agreement was found for $\mu_{C2} = 0.7, \sigma_{C2} = 0.69$ and $A_{C2} = 2 \times 10^{16}$ cm^{-3}. The result can be seen in figure 8.2.1 (dashed black line). To match

the experimental extinction coefficient of crystal C1, a slightly different lognormal distribution with $\mu_{C1} = 0.7, \sigma_{C1} = 0.66$ and $A_{C1} = 2 \times 10^{16}$ cm^{-3} had to be assumed (see dashed red line in Fig. 8.2.1).

Both size distributions peak at 1.3 nm, which is close to the most common diameter found in our TEM observations. The calculated average porosity of the host material, i.e. the fraction of empty space given by the integrated volume of the vacancy clusters according to $\int f(s)\frac{4}{3}\pi\left(\frac{s}{2}\right)^2 ds$, is similar for both top-seeded solution grown crystals and amounts to about 0.06% (C1) and 0.07% (C2), respectively. However, crystal C1 has slightly more voids in the 0-5 nm range, while C2 has more voids of larger sizes (see Fig. 8.2.5). This difference in the nano-void size density distribution explains the difference in the absorption spectra.

Using the void sizes and densities found for the Verneuil grown crystal, the calculated Mie scattering curve shows no significant absorption in the wavelength range considered (see Fig. 8.2.1). This can be easily seen from equation 8.3.2: if the density drops by an order of magnitude, the total absorption will drop by an order of magnitude as well. Since the Verneuil crystal shows almost no nano-voids in size categories besides 10-30 nm, the scattering will be even smaller. Using a lognormal distribution with $\mu = 2.7, \sigma = 0.3$ and $A = 2 \times 10^{13}$ cm^{-3}, calculated for diameters of 10-30 nm, a spectrum was predicted which is shown in figure 8.2.1. From that spectrum, it is clear that the concentration of nano-voids is too small to cause detectable scattering.

For the LHPG sample ST40, almost no voids outside the 1-5 nm range were found, with a typical diameter of about 2 nm and an average density of $\approx 10^{15}$ cm^{-3}. This was represented with a lognormal distribution with $\mu = 1.175, \sigma = 0.69$ and $A = 1 \times 10^{15}$ cm^{-3}. As can be seen in figure 8.3.2 a), the nano-void size density cannot explain the measured optical absorption. The calculated scattering contribution is shown in figure 8.3.2 b). It is clearly so small that the total calculated spectrum is determined by the absorption of the STO matrix. The absorption is probably due to the significant non-stoichiometry of this sample (see table 8.2.1 and Fig. 6.2.10). The high Sr/Ti ratio should result in a large number of Sr''_{Ti} anti sites [95], which could cause such an absorption. This might be verified by low temperature spectroscopy, as an absorption by a charged defect should shift with temperature, or by time dependent density functional theory calculations (TDDFT). TDDFT is an extension of conventional DFT which is capable of predicting photoabsorption properties and other time dependent field interactions.

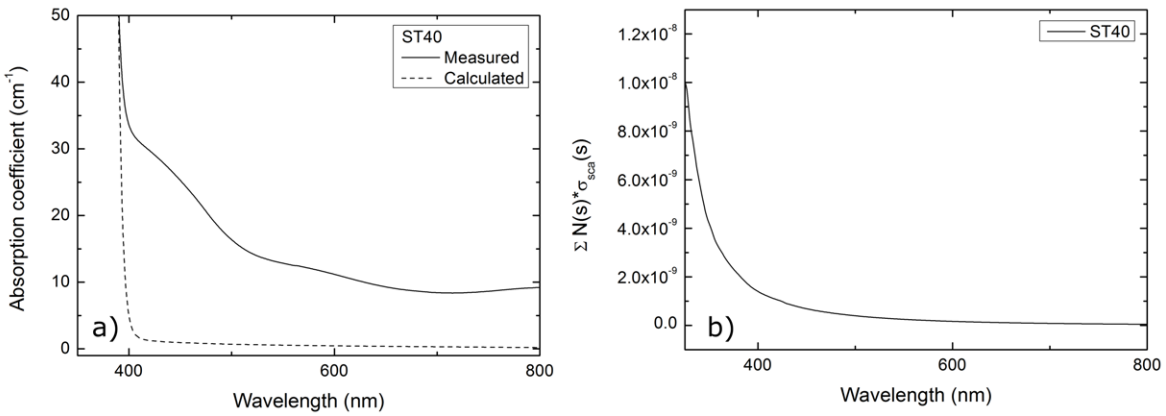

Figure 8.3.2.: a) Measured and calculated spectrum of LHPG crystal ST40. b) Calculated scattering for crystal ST40.

8.3.2. Formation of vacancy clusters

It is not entirely clear how the nanometer sized voids are formed. However, we will argue in the following that they are the result of a vacancy cluster mechanism. According to ab-initio calculations by Varley et al. [94] and Liu et al. [95], Sr and O vacancies are the dominating point defect species in $SrTiO_3$ crystals grown under TiO_2-rich conditions and moderate oxygen partial pressures, which corresponds to the crystals investigated here (see section 2.5). Under these conditions the formation energies of both vacancies are comparatively low ($\approx$1 eV, Ref. [94] and Ref. [95]) and will result in equilibrium concentrations of about 10^{18} to 10^{19} cm^{-3} in the crystal at the relevant growth temperature. Since Sr and O vacancies are shallow acceptors and shallow donors with a 2- and 2+ charge state compared to the occupied lattice position respectively, they will be Coulomb attractive and combine to form neutral di-vacancies. These di-vacancies serve as a nucleus for nano-voids and increase their size by continuous attachment of further vacancies. The size distribution and density of these clusters is then essentially governed by diffusion of the vacancies during growth and cool down. The lognormal distribution of nano-void diameters found here indicates a random nucleation growth mechanism [153, 154]. This growth mechanism assumes that there is no significant contribution of the dissolution and coarsening, which implies a high diffusion barrier for clustered vacancies in this system.

Considering this we may explain why crystal C2 has more vacancy clusters of larger size than crystal C1 and consequently appears darker: the lower temperature gradient and lower cooling rate of the growing crystal give more time for the vacancies to move through the crystal and to cluster before they are frozen in and thus result in larger clusters.

What is still unclear is the role of Ti in the formation of the clustered vacancies. The TEM measurements show that the voids are completely empty and no traces of Ti or TiO_2 are found. Whether the surplus Ti ions are incorporated onto interstitial sites or at anti-site after the V_{Sr}-V_O vacancy clusters have formed is not clear from the present data.

From the work of Guguschev et al. on the top-seeded solution growth of STO in different atmospheres, it is clear that the atmosphere plays an important role in the coloration of the crystals [30]. The crystals grown in an Ar or N_2 atmosphere with an oxygen concentration between 0.16 and 2.83 vol% were brown, while the crystals grown in pure N_2 have had a blue or black color due to free carrier absorption caused by oxygen vacancies. If the appropriate oxygen concentration in the gas phase is used, it is possible to grow colorless crystals. This is shown in Ref. [30]: A crystal, which was grown in a 5N Ar atmosphere that contained 2×10^{-6} bar residual oxygen was blue-black at the top of the crystal while the bottom was brown and the center was colorless. Based on our consideration, the relative concentrations of Sr and O vacancies influence the degree of brown coloration through vacancy cluster formation (if the cooling is slow enough for nano-voids to form) and the vacancy concentrations are strongly influenced by the growth atmosphere. According to Varley et al. the V''_{Sr} formation energy is lowest in Ti and oxygen rich environments [94]. In a reducing and Sr rich environment the Sr-vacancy formation energy is up to 4.6 eV higher. Accordingly, the brown coloration is weaker or absent for crystals grown in oxygen poor atmospheres.

Therefore, there are two main possibilities to reduce or prevent the brown coloration in the top-seeded solution growth of $SrTiO_3$. First, the temperature gradient can be increased; reducing the time the vacancies are mobile. This has to be balanced against the thermally induced strain on the crystal. Secondly, the oxygen content of the atmosphere can be lowered to increase the formation energy of Sr vacancies. Care has to be taken not to decrease it too far, since the free carriers from the oxygen vacancies will reduce the IR transmission of the crystal which can destabilize the growth [30].

8.4. Summary

The brown coloration of STO crystals grown by the TSSG method in an oxygen containing atmosphere from a TiO_2-rich solution is caused by Mie scattering at nano-voids in the crystal. These nanometer sized voids were observed and studied quantitatively by TEM measurements. Based on the experimentally determined void size distribution, theoretical absorption spectra were calculated and matched to measured spectra. The nano-voids are probably composed of combined Sr and O vacancies, which are oppositely charged, attract each other and combine into neutral vacancies. These combined vacancies serve as the nuclei for voids which can grow out to several nm in size during cooling, which results in a darker crystal coloration for crystals which were grown in lower temperature gradients (higher crystal temperature). In neutral and reducing atmospheres the V''_{Sr} formation energy is much higher [94], consequently, fewer vacancy clusters will be formed and no brown coloration occurs.

In non-stoichiometric crystals, there seems to be another mechanism at work. For the LHPG grown crystal ST40 the number and size of the nano-voids found in the TEM investigation is too small to explain the coloration by Mie scattering. The crystal shows a relatively large excess of Sr and is Ti deficient, which points to the formation of Sr''_{Ti} anti sites which could explain the measured absorption.

Acknowledgments

I am grateful to Dr. Toni Markurt and Dr. Mutong Niu for the TEM measurements, to Dr. Christo Guguschev for growing the TSSG crystals and to Franz Kamutzki for growing the LHPG fibers. I also want to thank Dr. Rainer Bertram for the ICP-OES measurements and Dr. Klaus Irmscher and Mike Pietsch for their support with the low temperature spectroscopy and Thomas Wurche for cutting the samples and Manuela Imming-Friedland and Viola Lange for the chemo-mechanical polishing.

9. Summary and conclusions

The investigations of the high temperature properties clearly show that both the radiative and conductive heat transport in $SrTiO_3$ are very low at high temperatures, but strongly depend on temperature. The large absorption of thermal radiation is caused by the high absorption of free carriers generated by excitation across the shrunken band gap and charged vacancies. It does not appear that the compensation doping decreased the infrared absorption, which indicates that the main source of the free carriers is excitation over the band gap which is to large to compensate for. Because the band gap decreases so strongly, it approaches the black body emissivity maximum and is only about 0.2 eV higher than the photon energy of maximum black body emission, which causes a large fundamental absorption of thermal radiation. These effects mean that STO has a very strong tendency to spiral formation when grown from a stoichiometric melt by the Czochralski method, even for small disturbances of the symmetry.

It is possible to grow spiral-free crystals with the EFG method since there the shape of the meniscus is stabilized by the die and, since the growth interface does not move relative to the set up during the growth, the thermal conditions of the growing crystal can be controlled more easily. Since the heat transport through $SrTiO_3$ improves with decreasing temperature, TSSG also avoids spiral formation and has produced crystals with very high quality. This does come at the price of low growth rates, but is very useful to provide seeds for EFG growth.

The optical properties of the crystals are largely controlled by the growth atmospheres and conditions. The LHPG experiments showed that a significant oxygen concentration ($\gtrsim 1$ vol%) resulted in crystals with a yellow to brown coloration which is characterized by a broad absorption band convoluted with the band gap. For low oxygen concentrations, like a 5N Ar atmosphere ($\sim 2\times10^{-4}$ vol% O_2), the LHPG crystals turn blue to black due to free carriers generated from oxygen vacancies. With the correct oxygen partial pressure (~ 1 vol%) and a slight SrO enrichment in the feed rod, colorless crystal fibers were grown.

The optical properties of the LHPG and top-seeded solution grown crystals show similar dependencies on oxygen partial pressure, but the transition from blue/black to colorless and from colorless to brown happen at different oxygen concentrations and temperatures. This is because the defect concentrations depend on the temperature and the atmosphere. The top of the TSSG crystals have the highest Sr concentrations which drop with crystal length. This is probably caused by reintegration of Sr from the gas phase which decreases as the temperature is lowered. Crystals grown below 2013 K show yellow to brown coloration for oxygen concentrations in the growth atmosphere above 0.16 vol% and a 5N Ar atmosphere resulted in a crystal which has blue/black reduced areas, colorless areas and a yellow/brown foot. A more reducing 5N N_2 atmosphere makes the crystals dark blue or black and conductive. The TSSG crystals grown below 1808 K in air showed only a light brown coloration and were closest to stoichiometric, while the LHPG crystals and the TSSG crystals grown below 2013 K showed deviations from cation stoichiometry of up to 0.5 at%. This is consistent with the phase width known to be possible in ceramics [90] and thin layers [91].

The brown coloration of the nearly stoichiometric TSSG crystals grown below 1808 K can be explained by Mie scattering at nanometer sized voids in stoichiometric top-seeded solution grown crystals. These nano-voids probably form through the combination of charged vacancies during the growth process. For some LHPG crystals, the nano-void densities determined in

TEM investigations cannot explain the absorption coefficients measured. These fibers show an excess of Sr and a deficiency in Ti, so Sr_{Ti} anti site defects are proposed to cause part of the brown coloration. The formation of these defects is predicted from simulations by Liu et al. [95].

$SrTiO_3$ crystals with significant free electron concentrations have a blue color and show an absorption peak around 2.4 eV. Rutile crystals show a similar coloration when they are *n*-type conductive and a similar peak, which is attributed to the splitting of Ti 3d orbitals which make up the bottom of the conduction band in TiO_2 and STO. The degeneracy of the Ti 3d orbitals is canceled by crystal field splitting in the octahedral complex formed with the oxygen ions. Inverse photo emission spectroscopy and X-ray absorption spectroscopy studies found that the splitting of the Ti 3d levels in $SrTiO_3$ is close to 2.4 eV, so the peak is assigned to this transition.

All in all, the growth of high quality $SrTiO_3$ crystals requires a growth method that either operates significantly below the melting point or a growth method that can improve the stability of the growth interface and that allows for very good control of the radial and axial thermal gradients. To achieve crystals that are colorless, the correct oxygen concentration in the growth atmosphere has to be found, which will differ with temperature and other growth conditions. Also, a slight Sr excess, to counter evaporation and increase the Sr vacancy formation energy, may be required.

Bibliography

[1] K. van Benthem, C. Elsässer, and R. H. French. Bulk electronic structure of $SrTiO_3$: Experiment and theory. *J. Appl. Phys.*, 90(12):6156, 2001.

[2] H.Y. Hwang. Perovskites: Oxygen vacancies shine blue. *Nat. Mater.*, 4(11):803–804, 2005.

[3] J. Son, P. Moetakef, B. Jalan, O. Bierwagen, N.J. Wright, R. Engel-Herbert, and S. Stemmer. Epitaxial $SrTiO_3$ films with electron mobilities exceeding 30,000 $cm^2V^{-1}s^{-1}$. *Nat. Mater.*, 9(6):482–484, 2010.

[4] Office of Technology Assessment. Power sources for remote arctic applications,. Technical report, U.S. Congress, 1994. OTA-BP-ETI 129.

[5] J. Roqueta, A. Pomar, L. Balcells, C. Frontera, S. Valencia, R. Abrudan, B. Bozzo, Z. Konstantinović, J. Santiso, and B. Martínez. Strain-Engineered Ferromagnetism in $LaMnO_3$ Thin Films. *Crystal Growth & Design*, 15(11):5332–5337, 2015.

[6] A. Vasudevarao, A. Kumar, L. Tian, J. H. Haeni, Y. L. Li, C.-J. Eklund, Q. X. Jia, R. Uecker, P. Reiche, K. M. Rabe, L. Q. Chen, D. G. Schlom, and V. Gopalan. Multiferroic domain dynamics in strained strontium titanate. *Phys. Rev. Lett.*, 97:257602, 2006.

[7] M. Kubo, Y. Oumi, R. Miura, A. Stirling, A. Miyamoto, M. Kawasaki, M. Yoshimoto, and H. Koinuma. Atomic control of layer-by-layer epitaxial growth on $SrTiO_3(001)$: Molecular-dynamics simulations. *Phys. Rev. B*, 56:13535–13542, 1997.

[8] Y. C. Liao, T. Kopp, C. Richter, A. Rosch, and J. Mannhart. Metal-insulator transition of the $LaAlO_3$-$SrTiO_3$ interface electron system. *Phys. Rev.*, 83:075402, 2011.

[9] Y. Hotta, T. Susaki, and H. Y. Hwang. Polar Discontinuity Doping of the $LaVO_3/SrTiO_3$ Interface. *Phys. Rev. Lett.*, 99:236805, 2007.

[10] H.Y. Hwang, A. Ohtomo, N. Nakagawa, D.A. Muller, and J.L. Grazul. High-mobility electrons in $SrTiO_3$ heterostructures . *Physica E*, 22:712, 2004.

[11] A. Ohtomo and H. Y. Hwang. A high-mobility electron gas at the $LaAlO_3/SrTiO_3$ heterointerface. *Nature*, 427:423, 2004.

[12] Kalabukhov, A. and Gunnarsson, R. and Börjesson, J. and Olsson, E. and Claeson, T. and Winkler, D. Effect of oxygen vacancies in the $SrTiO_3$ substrate on the electrical properties of the $LaAlO_3 - SrTiO_3$ interface. *Phys. Rev. B*, 75:121404, 2007.

[13] P. Moetakef, T.A. Cain, D.G. Ouellette, J.Y. Zhang, D.O. Klenov, A. Janotti, C.G. Van de Walle, S. Rajan, S.J. Allen, and S. Stemmer. Electrostatic carrier doping of $GdTiO_3/SrTiO_3$ interfaces. *Appl. Phys. Lett.*, 99:232116, 2011.

[14] A. Ohtomo, D. Muller, J. Gazul, and H. Hwang. Artificial charge-modulation in atomic scale perovskite titanate superlattices. *Nature*, 419:378, 2002.

[15] P. Perna, D. Maccariello, M. Radovic, U. S. di Uccio, I. Pallecchi, M. Codda, D. Marre, C. Cantoni, J. Gazquez, M. Varela, S. J. Pennycook, and F. M. Granozio. Conducting interfaces Between band insulating oxides: the $LaGaO_3/SrTiO_3$ heterostructure. *Appl. Phys. Lett.*, 97:152111, 2010.

[16] A. Brinkman, M. Huijben, M. van Zalk, J. Huijben, U. Zeitler, J. C. Maan, W. G. van der Wiel, G. Rijnders, D. H. A. Blank, and H. Hilgenkamp. Magnetic effects at the interface between nonmagnetic oxides. *Nat. Mater.*, 6(7):493–496, 2007.

[17] N. Reyren, S. Thiel, A. D. Caviglia, L. Fitting Kourkoutis, G. Hammerl, C. Richter, C. W. Schneider, T. Kopp, A.-S. Rüetschi, D. Jaccard, M. Gabay, D. A. Muller, J.-M. Triscone, and J. Mannhart. Superconducting interfaces between insulating oxides. *Science*, 317(5842):1196–1199, 2007.

[18] A.D. Caviglia, S. Gariglio, N. Reyren, D. Jaccard, T. Schneider, M. Gabay, S. Thiel, G. Hammerl, J. Mannhart, and J.-M. Triscone. Electric field control of the $LaAlO_3/SrTiO_3$ interface ground state. *Nature*, 456(7222):624–627, 2008.

[19] J.A. Bert, B. Kalisky, C. Bell, M. Kim, Y. Hikita, H.Y. Hwang, and K.A. Moler. Direct imaging of the coexistence of ferromagnetism and superconductivity at the $LaAlO_3/SrTiO_3$ interface. *Nature physics*, 7(10):767–771, 2011.

[20] L. Li, C. Richter, J. Mannhart, and R.C. Ashoori. Coexistence of magnetic order and two-dimensional superconductivity at $LaAlO_3/SrTiO_3$ interfaces. *Nature Physics*, 7(10): 762–766, 2011.

[21] D.A. Dikin, M. Mehta, C.W. Bark, C.M. Folkman, C.B. Eom, and V. Chandrasekhar. Coexistence of superconductivity and ferromagnetism in two dimensions. *Physical Review Letters*, 107(5):056802, 2011.

[22] S. Thiel, C. W. Schneider, L. Fitting Kourkoutis, D. A. Muller, N. Reyren, A. D. Caviglia, S. Gariglio, J. M. Triscone, and J. Mannhart. Electron scattering at dislocations in $LaAlO_3/SrTiO_3$ interfaces. *Phys. Rev. Lett.*, 102:046809, 2009.

[23] X. Liu, D. Choudhury, Y. Cao, M. Kareev, S. Middey, and J. Chakhalian. Metallic interface in non-$SrTiO_3$ based titanate superlattice. *Applied Physics Letters*, 107(19): 191602, 2015.

[24] K. Zou, S. Ismail-Beigi, K. Kisslinger, X. Shen, D. Su, F. J. Walker, and C. H. Ahn. $LaTiO_3/KTaO_3$ interfaces: A new two-dimensional electron gas system. *APL Mater.*, 3(3):036104, 2015.

[25] J.W. Park, D.F. Bogorin, C. Cen, D.A. Felker, Y. Zhang, C.T. Nelson, C.W. Bark, C.M. Folkman, X.Q. Pan, M.S. Rzchowski, J. Levy, and C.B. Eom. Creation of a two-dimensional electron gas at an oxide interface on silicon. *Nature communications*, 1:94, 2010.

[26] C. W. Bark, D. A. Felker, Y. Wang, Y. Zhang, H. W. Jang, C. M. Folkman, J. W. Park, S. H. Baek, H. Zhou, D. D. Fong, X. Q. Pan, E. Y. Tsymbal, M. S. Rzchowski, and C. B. Eom. Tailoring a two-dimensional electron gas at the $LaAlO_3/SrTiO_3$ (001) interface by epitaxial strain. *Proc. Natl. Acad. Sci. USA*, 108(12):4720–4724, 2011.

[27] K. Nassau and A.E. Miller. Strontium titanate: An index to the literature on properties and the growth of single crystals. *J. Cryst. Growth*, 91(3):373 – 381, 1988.

[28] P.I. Nabokin, D. Souptel, and A.M. Balbashov. Floating zone growth of high-quality $SrTiO_3$ single crystals. *J. Cryst. Growth*, 250:397, 2003.

[29] M. Schmidbauer, A. Kwasniewski, and J. Schwarzkopf. High-precision absolute lattice parameter determination of $SrTiO_3$, $DyScO_3$ and $NdGaO_3$ single crystals. *Acta Crystallogr. B*, 68:8–14, 2012.

[30] C. Guguschev, D.J. Kok, Z. Galazka, D. Klimm, R. Uecker, R. Bertram, M. Naumann, U. Juda, A. Kwasniewski, and M. Bickermann. Influence of oxygen partial pressure on $SrTiO_3$ bulk crystal growth from non-stoichiometric melts. *CrystEngComm*, 17(17): 3224–3234, 2015.

[31] C. Guguschev, D. Klimm, F. Langhans, Z. Galazka, D.J. Kok, U. Juda, and R. Uecker. Top-seeded solution growth of $SrTiO_3$ crystals and phase diagram studies in the SrO-TiO_2 system. *Cryst. Eng. Comm.*, 16(9):1735, 2014.

[32] S. Mochizuki, F. Fujishiro, K. Shibata, A. Ogi, T. Konya, and K. Inaba. Optical, electrical, and X-ray-structural studies on Verneuil-grown $SrTiO_3$ single crystal: Annealing study. *Physica B: Condensed Matter*, 401-402(0):433 – 436, 2007. Proceedings of the 24th International Conference on Defects in Semiconductors.

[33] K.H. Lee, S.W. Kim, H. Ohta, and K. Koumoto. Ruddlesden-Popper phases as thermoelectric oxides: Nb-doped $SrO(SrTiO_3)_n$ ($n = 1, 2$). *J. Appl. Phys.*, 100(6):063717, 2006.

[34] P. Paufler, B. Bergk, M. Reibold, A. Belger, N Pätzke, and D. C. Meyer. Why is $SrTiO_3$ much stronger at nanometer than at centimeter scale? *Solid State Sciences*, 8(7):782 – 792, 2006.

[35] V. Trepakov, A. Dejneka, B. Markovin, A. Lynnyk, and L. Jastrabik. A 'soft electronic band' and the negative thermooptic effect in strontium titanate. *New J. Phys.*, 11: 083024, 2009.

[36] A. H. Miklich, D. Koelle, E. Dantsker, D. T. Nemeth, J. J. Kingston, R. F. Kromann, and J. Clarke. Bicrystal YBCO DC SQUIDs with low noise. *IEEE Trans. Appl. Supercond.*, 3(1):2434–2437, 1993.

[37] G. Shirane and Y. Yamada. Lattice-Dynamical Study of the 110°K Phase Transition in $SrTiO_3$. *Phys. Rev.*, 177:858–863, 1969.

[38] R. Uecker, H. Wilke, D.G. Schlom, B. Velickov, P. Reiche, A. Polity, M. Bernhagen, and M. Rossberg. Spiral formation during czochralski growth of rare-earth scandates. *J. Cryst. Growth*, 295(1):84, 2006.

[39] P. Naumowicz, K. Wieteska, S. Szarras, and J. Cinak. Growth spirals of gadolinium gallium garnet (GGG) crystals. *Kristall und Technik*, 16(9):983–988, 1981.

[40] D. Schwabe, R. Uecker, M. Bernhagen, and Z. Galazka. An analysis of and a model for spiral growth of Czochralski-grown oxide crystals with high melting point. *J. Cryst. Growth*, 335(1):138, 2011.

[41] C. Derks, K. Kuepper, M. Raekers, A. V. Postnikov, R. Uecker, W. L. Yang, and M. Neumann. Band-gap variation in $R ScO_3$ (R = Pr, Nd, Sm, Eu, Gd, Tb, and Dy): X-ray absorption and O K-edge x-ray emission spectroscopies. *Phys. Rev. B*, 86:155124, 2012.

[42] A Verneuil. The artificial production of the ruby by fusion. *C. r. hebd. séances acad. sci.* , 135:791–794, 1902.

[43] H.J. Scheel. Historical aspects of crystal growth technology. *J. Cryst. Growth*, 211:1 – 12, 2000.

[44] J.G. Bednorz and H.J. Scheel. Flame-fusion growth of $SrTiO_3$. *J. Cryst. Growth*, 41:5, 1977.

[45] J. Bohm. *Kristalle: eine populärwissenschaftliche Darstellung.* Dt. Verl. d. Wiss., Berlin, 1975.

[46] L. Merk and L. E. Lynd. Method of pereparation of monocrystaline strontium titanate of high refractive index, 1954. US patent number 2684910.

[47] J. A. Adamski. New oxy-hydrogen burner for flame fusion. *J. Appl. Phys.*, 36(5): 1784–1786, 1965.

[48] S. Mochizuki, F. Fujishiro, K. Ishiwata, and K Shibata. Defect-induced optical absorption and photoluminescence of Verneuil-grown $SrTiO_3$ crystal . *Phys. B*, 376-377(0):816 – 819, 2006.

[49] K. P. Quinian, R. M. Hilton, and A. Adamski. Preparation of the superconductor substrate: Strontium titanate. Technical report, Rome Air Development Center, 1989.

[50] R. L. Wild, E. M. Rockar, and J. C. Smith. Thermochromism and Electrical Conductivity in Doped $SrTiO_3$. *Phys. Rev. B*, 8:3828–3835, 1973.

[51] H. J. Scheel, J. G. Bednorz, and P. Dill. Crystal growth of strontium titanate $SrTiO_3$. *Ferroelectrics*, 13(1):507–509, 1976.

[52] N. A. Kulagin, J Dojcilovic, and D. Popovic. *Physics of Laser Crystals*, chapter 13, pages 187–199. Number 126 in Nato Science Series II. Springer Netherlands, 1 edition, 2003.

[53] J. Czochralski. Ein neues verfahren zur messung der kristallisationsgeschwindigheit der metalle. *Z. phys. Chemie.*, 92:219–221, 1918.

[54] William C. Dash. Growth of silicon crystals free from dislocations. *Journal of Applied Physics*, 30(4):459–474, 1959.

[55] W. Zulehner and D. Huber. *Crystals*, volume 8. Springer Verlag, 1982.

[56] J. Friedrich, W. von Ammon, and G. Müller. *Handbook of crystal growth*, volume 2 A, chapter 2.2.3, page 52. Elsevier, 2nd edition, 2015.

[57] N. Miyazaki, A. Hattori, and H. Uchida. Thermal shock cracking of lithium niobate single crystal. *J. Mater. Sci. Mater. Electron.*, 8(3):133–138, 1997.

[58] Z. Galazka. Analysis of thermal shock during rapid crystal extraction from melts. *Cryst. Res. Technol.*, 34(5-6):635–640, 1999.

[59] C. Guguschev, Z. Galazka, D. J. Kok, U. Juda, A. Kwasniewski, and R. Uecker. Growth of $SrTiO_3$ bulk single crystals using edge-defined film-fed growth and the Czochralski methods. *CrystEngComm*, 17:4662–4668, 2015.

[60] M. Uwaha. *Handbook of crystal growth*, volume 1 B, chapter 8.3, pages 364–369. Elsevier, 2nd edition, 2015.

[61] D. Rytz, B.A. Wechsler, C.C. Nelson, and K.W. Kirby. Top-seeded solution growth of $BaTiO_3$, $KNbO_3$, $SrTiO_3$, $Bi_{12}TiO_{20}$ and $La_{2-x}Ba_xCuO_4$. *J. Cryst. Growth*, 99:864 – 868, 1990.

[62] H. J. Scheel and L. Lytvynov. *Crystal Growth Technology: From Fundamentals and Simulation to Large-scale Production*, chapter 16, pages 415–434. Wiley-VCH Verlag GmbH & Co. KGaA, 2008.

[63] C. Guguschev, D. J. Kok, U. Juda, R. Uecker, S. Sintonen, Z. Galazka, A. Kwasniewski, and M. Bickermann. Top-seeded solution growth of $SrTiO_3$ single crystals virtually free of mosaicity. *J. Cryst. Growth*, 2016. ICCGE-18 special volume, under review.

[64] D. J. Kok, C. Guguschev, T. Markurt, M. Niu, R. Bertram, M. Albrecht, and K. Irmscher. Origin of brown coloration in top-seeded solution grown SrTiO3 crystals. *CrystEngComm*, 2016. doi: 10.1039/C6CE00247A.

[65] H.E. LaBelle Jr. EFG, the invention and application to sapphire growth. *J. Cryst. Growth*, 50(1):8 – 17, 1980.

[66] Antonov and Kurlov. A review of developments in shaped crystal growth of sapphire by the stepanov and related techniques. *Prog. Cryst. Growth Charact. Mater.*, 44:63–122, 2002.

[67] C. Guguschev, G. Calvert, S. Podowitz, A. Vailionis, A. Yeckel, and R. S. Feigelson. The application of floating dies for high speed growth of CsI single crystals by edge-defined film-fed growth (EFG) . *J. Cryst. Growth*, 404:231 – 240, 2014.

[68] A. Yoshikawa and V. Chani. Growth of optical crystals by the micro pulling down method. *MRS Bulletin*, 34:266–270, 2009.

[69] A. Yoshikawa, M. Nikl, G. Boulon, and T. Fukuda. Challenge and study for developing of novel single crystalline optical materials using micro pulling down method. *Optical Materials*, 30(1):6 – 10, 2007.

[70] D. Klimm, S. Ganschow, D. Schulz, R. Bertram, R. Uecker, P. Reiche, and R. Fornari. Growth of oxide compounds under dynamic atmosphere composition. *J. Cryst. Growth*, 311(3):534 – 536, 2009. The Proceedings of the 4th International Asian Conference on Crystal Growth and Crystal Technology.

[71] T. Higuchi, T. Tsukamoto, N. Sata, M. Ishigame, Y. Tezuka, and S. Shin. Electronic structure of p-type $SrTiO_3$ by photoemission spectroscopy. *Phys. Rev. B*, 57:6978–6983, 1998.

[72] T. Higuchi, T. Tsukamoto, K. Kobayashi, S. Yamaguchi, Y. Ishiwata, N. Sata, K. Hiramoto, M. Ishigame, and S. Shin. Direct evidence of p -type $SrTiO_3$ by high-resolution x-ray absorption spectroscopy. *Phys. Rev. B*, 65:033201, 2001.

[73] W. Huang, R. Nechache, S. Li, M. Chaker, and F. Rosei. Electrical and Optical Properties of Transparent Conducting p-Type $SrTiO_3$ Thin Films. *Journal of the American Ceramic Society*, 99(1):226–233, 2016.

[74] L. Gil Escrig, M. Prades, H. Beltrán, E. Cordoncillo, N. Masó, and A. R. West. Voltage-Dependent Bulk Resistivity of $SrTiO_3$:Mg Ceramics. *J. Am. Ceram. Soc.*, 97(9):2815–2824, 2014.

[75] K. Lebbou and G. Boulon. *Fiber crystal growth from the melt*, volume 6 of *Advances in Materials Research*, chapter 7, pages 214–254. Springer-Verlag Berlin Heidelberg, 1 edition, 2004.

[76] C. Guguschev, J. Götze, and M. Göbbels. Cathodoluminescence microscopy and spectroscopy of synthetic ruby crystals grown by the optical floating zone technique. *American Mineralogist*, 95(4):449–455, 2010.

[77] F. Kamutzki, C. Guguschev, D.J. Kok, R. Bertram, U. Juda, and R. Uecker. The Influence of oxygen partial pressure in the growth atmosphere on the coloration of $SrTiO_3$ single Crystal fibers. *Cryst. Eng. Comm.*, (18):5658–5666, 2016.

[78] J. Philipen. *Fiber crystal growth of cerium doped calcium scandate, strontium yttrium oxide, and tristrontium silicate.* PhD thesis, Technical University of Berlin, 2013.

[79] M. M. Fejer, J. L. Nightingale, G. A. Magel, and R. L. Byer. Laser-heated miniature pedestal growth apparatus for single-crystal optical fibers. *Rev. Sci. Instrum.*, 55(11): 1791–1796, 1984.

[80] R.S. Feigelson. Proceedings of the eighth international conference on crystal growth pulling optical fibers. *J. Cryst. Growth*, 79(1):669 – 680, 1986.

[81] D. R. Ardila, M.R.B. Andreeta, S.L. Cuffini, A. C. Hernandes, J.P. Andreeta, and Y.P. Mascarenhas. Single-crystal $SrTiO_3$ fiber grown by laser heated pedestal growth method: influence of ceramic feed rod preparation in fiber quality. *Materials Research*, 1:11 – 17, 1998.

[82] J.-I. Yoshimura, T. Sakamoto, and J. Yamanaka. X-Ray Double-Crystal Diffractometry of Verneuil-Grown $SrTiO_3$ Crystals. *Jpn. J. Appl. Phys*, 40(11R):6536, 2001.

[83] K. Oka and H. Unoki. Crystal growth of $BaTiO_3$ and $SrTiO_3$ by the Top Seeded Solution Growth Method. *Bull. Electrotech. Lab. (Ministry of Intern. Trade and Industry, Tokyo)*, (39), 1975.

[84] Farrel W. Lytle. X-ray diffractometry of low-temperature phase transformations in strontium titanate. *J. Appl. Phys.*, 35(7):2212–2215, 1964.

[85] T. Hungria, I. MacLaren, H. Fuess, J. Galy, and A. Castro. HREM studies of intergrowths in $Sr_2[Sr_{n-1}Ti_nO_{3n+1}]$ Ruddlesden-Popper phases synthesized by mechanochemical activation. *Mater. Lett.*, 62:3095–3098, 2008.

[86] A. Chernatynskiy, R. W. Grimes, M. A. Zurbuchen, D. R. Clarke, and S. R. Phillpot. Crossover in thermal transport properties of natural, perovskite-structured superlattices. *Appl. Phys. Lett.*, 95:161906–1–3, 2009.

[87] J. Lee and T. A. Arias. Structural phase transitions in Ruddlesden-Popper phases of strontium titanate: Ab initio and modulated Ginzburg-Landau approaches. *Phys. Rev. B*, 82:180104 1–4, 2010.

[88] C.-H. Nien and H.-Y. Lu. Crystallographic Orientation Relationships Between $SrTiO_3$ and Ruddlesden-Popper Phase. *J. Am. Ceram. Soc.*, 95:1676–1681, 2012.

[89] G. J. McCarthy, W. B. White, and R. Roy. Phase Equilibria in the 1375°C Isotherm of the System Sr-Ti-O. *Journal of the American Ceramic Society*, 52(9):463–467, 1969.

[90] Z. Wang, M. Cao, Z. Yao, G. Li, Z. Song, W. Hu, H. Hao, H. Liu, and Z. Yu. Effects of Sr/Ti ratio on the microstructure and energy storage properties of nonstoichiometric $SrTiO_3$ ceramics. *Ceram. Int.*, 40(1, Part A):929 – 933, 2014.

[91] E. Breckenfeld, R. Wilson, J. Karthik, A. R. Damodaran, D. G. Cahill, and L. W. Martin. Effect of Growth Induced (Non)Stoichiometry on the Structure, Dielectric Response, and Thermal Conductivity of $SrTiO_3$ Thin Films. *Chemistry of Materials*, 24(2):331–337, 2012.

[92] M. Kestigian, J. G. Dickinson, and R. Ward. Ion-deficient Phases in Titanium and Vanadium Compounds of the Perovskite Type. *J. Am. Chem. Soc.*, 79(21):5598–5601, 1957.

[93] A. Köhl. *Micro-spectroscopic investigation of valence change processes in resistive switching $SrTiO_3$ thin films.* PhD thesis, RWTH Aachen, 2014.

[94] J. B. Varley, A. Janotti, and C. G. Van de Walle. Hydrogenated vacancies and hidden hydrogen in $SrTiO_3$. *Phys. Rev. B*, 89:075202, 2014.

[95] B. Liu, V. R. Cooper, H. Xu, H. Xiao, Y. Zhang, and W. J. Weber. Composition dependent intrinsic defect structures in $SrTiO_3$. *Phys. Chem. Chem. Phys.*, 16:15590–15596, 2014.

[96] M. C. Tarun and M. D. McCluskey. Infrared absorption of hydrogen-related defects in strontium titanate. *J. Appl. Phys.*, 109(6):063706, 2011.

[97] D. C. Harris. *Quantitative chemical analysis*, chapter 18, pages 407–432. W. H. Freeman and Company, New York, 6 edition, 2003.

[98] D. K. Schroder. *Semiconductor material and device characterization*, chapter 10.4.1. John Wiley & Sons, Inc., 3rd edition, 2006.

[99] D. Dragoman and M. Dragoman. *Optical characterizazion of solids*, chapter 2.3.5.2. Springer-Verlag, 2002.

[100] J. Tauc. Optical properties and electronic structure of amorphous Ge and Si. *Mat. Re. Bul.*, 3(1):37 – 46, 1968.

[101] G. Mie. Beiträge zur Optik trüber Medien, speziell kolloidaler Metallösungen. *Annalen der Physik*, 330(3):377–445, 1908.

[102] M. Albrecht, R. Schewski, K. Irmscher, Z. Galazka, T. Markurt, M. Naumann, T. Schulz, R. Uecker, R. Fornari, S. Meuret, and M. Kociak. Coloration and oxygen vacancies in wide band gap oxide semiconductors: Absorption at metallic nanoparticles induced by vacancy clustering- A case study on indium oxide. *J. Appl. Phys.*, 115(5):053504, 2014.

[103] J. Yin and L. Pilon. Efficiency factors and radiation characteristics of spherical scatterers in an absorbing medium. *J. Opt. Soc. Am. A*, 23(11):2784–2796, 2006.

[104] W. C. Mundy, J. A. Roux, and A. M. Smith. Mie scattering by spheres in an absorbing medium. *J. Opt. Soc. Am.*, 64(12):1593–1597, 1974.

[105] Chýlek, P. Light scattering by small particles in an absorbing medium. *J. Opt. Soc. Am.*, 67(4):561–563, 1977.

[106] C. F. Bohren and D. P. Gilra. Extinction by a spherical particle in an absorbing medium. *J. Colloid interface sci.*, 72:215–221, 1979.

[107] M. Quinten and J. Rostalski. Lorenz-mie theory for spheres immersed in an absorbing host medium. *Particle & Particle Systems Characterization*, 13(2):89–96, 1996.

[108] A.N. Lebedev, M. Gartz, U. Kreibig, and O. Stenzel. Optical extinction by spherical particles in an absorbing medium: Application to composite absorbing films. *Eur. Phys. J. D*, 6(3):365–373, 1999.

[109] Q. Fu and W. Sun. Mie theory for light scattering by a spherical particle in an absorbing medium. *Appl. Opt.*, 40(9):1354–1361, 2001.

[110] I. W. Sudiarta and P. Chylek. Mie scattering efficiency of a large spherical particle embedded in an absorbing medium. *J. Quant. Spectrosc. Radiat. Transf.*, 70:709–714, 2001.

[111] I. W. Sudiarta and P. Chylek. Mie-scattering formalism for spherical particles embedded in an absorbing medium. *J. Opt. Soc. Am. A*, 18(6):1275–1278, 2001.

[112] M. J. Dodge. *Handbook of Laser Science and Technology*, volume IV of *Optical Material: Part 2*. CRC Press, Boca Raton, 1986.

[113] D. Schwabe and A. Polity. Transmission spectra of crystals at elevated temperatures for the calculation of internal radiant heat transport during crystal growth part 1: The spectrometer and its performance. *Cryst. Res. Technol.*, 38:868, 2003.

[114] D.J. Kok, K. Irmscher, M. Naumann, C. Guguschev, Z. Galazka, and R. Uecker. Temperature-dependent optical absorption of $SrTiO_3$. *Phys. Status Solidi A*, 9(212): 1880–1887, 2015.

[115] F.P. Ottensmeyer, D.P. Bazett-Jones, H.P. Rust, K. Weiss, F. Zemlin, and A. Engel. Radiation exposure and recognition of electron microscopic images of protamine at high resolution. *Ultramicroscopy*, 3:191, 1978.

[116] C.-L. Jia, M. Lentzen, and K. Urban. High-resolution transmission electron microscopy using negative spherical aberration. *Microscopy and Microanalysis*, 10:174–184, 2004.

[117] C.L. Jia, L. Houben, A. Thust, and J. Barthel. On the benefit of the negative-spherical-aberration imaging technique for quantitative HRTEM. *Ultramicroscopy*, 110(5):500 – 505, 2010. Hannes Lichte 65th Birthday.

[118] P.M. Voyles, J.L. Grazul, and D.A. Muller. Imaging individual atoms inside crystals with ADF-STEM . *Ultramicroscopy*, 96(3-4):251 – 273, 2003. Proceedings of the International Workshop on Strategies and Advances in Atomic Level Spectroscopy and Analysis.

[119] C. Guguschev, R. Tagle, U. Juda, and A. Kwasniewski. Microstructural investigations of $SrTiO_3$ single crystals and polysilicon using a powerful new X-ray diffraction surface mapping technique. *J. Appl. Crystallogr.*, 48(6):1883–1888, 2015.

[120] W. H. Bragg and W. L. Bragg. The Reflection of X-rays by Crystals. *Proc. R. Soc. A*, 88(605):428–438, 1913.

[121] Z. Galazka, K. Irmscher, R. Uecker, R. Bertram, M. Pietsch, A. Kwasniewski, M. Naumann, T. Schulz, R. Schewski, D. Klimm, and M. Bickermann. On the bulk β-Ga_2O_3 single crystals grown by the Czochralski method. *J. Cryst. Growth*, 404:184–191, 2014.

[122] D. Goldschmidt and H. L. Tuller. Fundamental absorption edge of $SrTiO_3$ at high temperatures. *Phys. Rev. B*, 35:4360, 1987.

[123] T. Bieger, M. Maier, and R. Waser. Optical investigation of oxygen incorporation in $SrTiO_3$. *Solid State Ionics*, 53-56:578, 1992.

[124] R. Moos and K. H. Hardtl. Defect Chemistry of Donor-Doped and Undoped Strontium Titanate Ceramics between 1000°C and 1400°C. *J. Am. Ceram. Soc.*, 80(10):2549, 1997.

[125] K. P. O'Donnell and X. Chen. Temperature dependence of semiconductor band gaps. *Appl. Phys. Lett.*, 58:2924, 1991.

[126] R. Pässler. Temperature dependence of fundamental band gaps in group IV, III-V, and II-VI materials via a two-oscillator model. *J. Appl. Phys.*, 89:6235, 2001. The parameters used by this author (α, θ) are related to S and $\hbar\omega$ of Ref. [125] by $\alpha = 2kS$ and $\theta = \hbar\omega/k$ where k is the Boltzmann constant.

[127] U. Balachandran and N. G. Eror. Raman spectra of strontium titanate. *J. Am. Ceram. Soc.*, 65:54, 1982.

[128] K. Irmscher, M. Naumann, M. Pietsch, Z. Galazka, R. Uecker, T. Schulz, R. Schewski, M. Albrecht, and R. Fornari. On the nature and temperature dependence of the fundamental band gap of In_2O_3. *Phys. Status Solidi A*, 211:54, 2014.

[129] F. Urbach. The long-wavelength edge of photographic sensitivity and of the electronic absorption of solids. *Phys. Rev.*, 92:1324, 1953.

[130] V Sayakanit and H.R. Glyde. Urbach tails and disorder. *Condens. Matter. Phys.*, 13: 35, 1987.

[131] R. C. Rai. Analysis of the Urbach tails in absorption spectra of undoped ZnO thin films. *J. Appl. Phys.*, 113:153508, 2013.

[132] M. Planck. Über das gesetz der energieverteilung im normalspectrum. *Annalen der Physik*, 309(3):553–563, 1901.

[133] C. Kittel. *Introduction to Solid State physics*, chapter 8, pages 205–207. John Wiley & Sons, Inc., 8th edition, 2005.

[134] M. Marques, L. K. Teles, V. Anjos, L. M. R. Scolfaro, J. R. Leite, V. N. Freire, G. A. Farias, and Jr. E. F. da Silva. Full-relativistic calculations of the $SrTiO_3$ carrier effective masses and complex dielectric function. *Appl. Phys. Lett.*, 82:3074, 2003.

[135] C. Mitra, C. Lin, J. Robertson, and Alexander A. Demkov. Electronic structure of oxygen vacancies in $SrTiO_3$ and $LaAlO_3$. *Phys. Rev. B.*, 86, 2012.

[136] D. Gryaznov, E. Blokhin, A. Sorokine, E. A. Kotomin, R. A. Evarestov, A. Bussmann-Holder, and J. Maier. A Comparative Ab Initio Thermodynamic Study of Oxygen Vacancies in ZnO and $SrTiO_3$: Emphasis on Phonon Contribution. *J. Phys. Chem. C*, 117:13776, 2013.

[137] R. Moos, W. Menesklou, and K.H. Härdtl. Hall mobility of undoped n-type conducting strontium titanate single crystals between 19 K and 1373 K. *Appl. Phys. A*, 61:389, 1995.

[138] M. Fleischer, H. Meixner, and C. Tragut. Hole mobility in acceptor-doped, monocrystalline $SrTiO_3$. *J. Am. Ceram. Soc.*, 75:1666, 1992.

[139] H. P. R. Frederikse, W. R. Thurber, and W. R. Hosler. Electronic transport in strontium titanate. *Phys. Rev.*, 134:A442–A445, 1964.

[140] K. Shirai and K. Yamanaka. Mechanism behind the high thermoelectric power factor of $SrTiO_3$ by calculating the transport coefficients. *J. Appl. Phys.*, 113:053705, 2013.

[141] H. Y. Fan. Infra-red absorption in semiconductors. *Rep. Prog. Phys.*, 19(1):107, 1956.

[142] W. S. Baer. Free-Carrier Absorption in Reduced $SrTiO_3$. *Phys. Rev.*, 144:734, 1966.

[143] D. De Sousa Meneses, P. Melin, L. del Campo, L. Cosson, and P. Echegut. Apparatus for measuring the emittance of materials from far infrared to visible wavelengths in extreme conditions of temperature. *Infrared Physics & Technology*, 69:96 – 101, 2015.

[144] D. Ferry. *Semiconductor Transport*. Taylor & Francis, 2000.

[145] A. Walsh, C. R. A. Catlow, A. G. H. Smith, A. A. Sokol, and S. M. Woodley. Strontium migration assisted by oxygen vacancies in $SrTiO_3$ from classical and quantum mechanical simulations. *Phys. Rev. B*, 83:220301, 2011.

[146] N.A. Kulagin and E. Hieckmann. Spectra and color centers of strontium titanate crystals. *Optics and Spectroscopy*, 112(1):79–86, 2012.

[147] V. M. Khomenko, K. Langer, H. Rager, and A. Fett. Electronic absorption by Ti^{3+} ions and electron delocalization in synthetic blue rutile. *Phys. Chem. Miner.*, 25(5):338–346, 1998.

[148] D. Baba, T. Higuchi, H. Kakemoto, Y. Tokura, S. Shin, and T. Tsukamoto. Unoccupied Electronic State of Lightly La-Doped $SrTiO_3$ Observed by Inverse-Photoemission Spectroscopy. *JPN. J. Appl. Phys.*, 42(7B):L837, 2003.

[149] L. F. Mattheiss. Energy Bands for $KNiF_3$, $SrTiO_3$, $KMoO_3$, and $KTaO_3$. *Phys. Rev. B*, 6:4718–4740, 1972.

[150] J. Kawanabe, H. Minami, K. Oka, and H. Uwe. Floating zone growth of $SrTiO_3$ single crystals and characterization by electronic transport property. *Ferroelectrics*, 348:89–93, 2007.

[151] B. Jalan, R. Engel-Herbert, T. E. Mates, and S. Stemmer. Effects of hydrogen anneals on oxygen deficient $SrTiO_{3-x}$ single crystals. *Appl. Phys. Let.*, 93(5):052907, 2008.

[152] J. M. Cowley and A. F. Moodie. The scattering of electrons by atoms and crystals. I. A new theoretical approach. *Acta Crystallographica*, 10(10):609–619, 1957.

[153] R. B. Bergmann and A. Bill. On the origin of logarithmic-normal distributions: An analytical derivation, and its application to nucleation and growth processes. *J. Cryst. Growth*, 310(13):3135 – 3138, 2008.

[154] A. V. Teran, A. Bill, and R. B. Bergmann. Time-evolution of grain size distributions in random nucleation and growth crystallization processes. *Phys. Rev. B*, 81:075319, 2010.

Acknowledgments

First of all, I would like to thank Dr. Christo Guguschev for his invaluable support, the fruitful cooperation, the many discussions we had on all aspects of this project, growing many of the crystals investigated here and proofreading this thesis. Without him, this project would not have been possible. Furthermore, I want to thank Dr. Zbigniew Galazka and Franz Kamutzki who both grew crystals and participated in many productive discussions.

I am indebted to Dr. Reinhard Uecker for the opportunity to work in this institute and for leadership and support in many situations. I also want to thank Steffen Ganschow for teaching me how to perform MPD growth. Furthermore, this work would not have been possible without the other members of the oxides and fluorides group, Mario Brützam, Martina Rabe, Dr. Detlev Schulz, Isabelle-Mercedes Schulze-Jonack, Andreas Tauchert and Elvira Thiede who assisted in many ways and situations.

I am grateful for the support of Dr. Detlef Klimm, who performed the thermodynamical measurements and calculations, participated in many good discussions and proofread this thesis. I also want to thank Dr. Rainer Bertram for the ICP-OES measurements.

I want to give special thanks to Dr. Klaus Irmscher who taught me a lot about spectroscopic semi conductor analysis, helped me measure low and high temperature spectra and which whom I have had may fruitful discussions. Also, I want to thank Martin Naumann for measuring the high temperature spectra and helping me with the improvements to the setup and Mike Pietsch who performed the conductivity measurements and helped me measure the low temperature spectra. I am grateful to Robert Schewski, Dr. Mutong Niu and especially Toni Markurt for performing the TEM measurements and to Dr. Martin Albrecht for the fruitful discussions to interpret the results.

I would like to thank Albert Kwasniewski who performed the XRD measurements, Thomas Wurche for cutting the samples and Manuela Imming-Friedland and Viola Lange who performed the chemo-mechanical polishing.

Last but not least, I am very grateful to my friends and family who supported me through this project, especially my fiancée Silvia for sharing my life and giving me all the support I could want.

A. Scripts

A.1. High temperature data processing

The data from the high temperature spectral measurements, as discussed in section 3.1.2, has to be corrected to obtain transmission values and then it has to be converted to absorption coefficient values. For this, a python function was written for the calculations for one file (calculate.py) which was called by a script that handles the data loading and temperature averaging (for example bandgapT2.py).

bandgapT2.py

```
#Script to do background correction, averaging per
    temperature and calculation of the absorption coefficient
    and its square root. Requuires a few functions.

#importing erquired modules:
import os
import numpy
import math

#Requesting the imput and switches over which steps are
    required

#Path: folder with the raw data
path = 'Y:\private\LwD\Spektralkurven_STO\Temperaturabhaengig
    \V3_Crystec\T2\Raw_data'
#Target: parent folder for the result files
target ='Y:\private\LwD\Spektralkurven_STO\
    Temperaturabhaengig\V3_Crystec\T2'
#number of header lines in the raw data
nheader=6
#number of background pixels at the end
nbg=142

#thickness of the sample in cm
thickness=0.047

listing = os.listdir(path) #Makes a list of all files in this
     path. Subfolders discouraged


for infile in listing:
    FILE=os.path.join(path, infile)
    with open(FILE, newline=''):
        #Read the first column as the wave length and the
            second as T/T%/Absorbance
        wavelength, value = numpy.loadtxt(FILE,skiprows=
            nheader,unpack=True)
```

```
        value=numpy.array(value)
        wavelength=numpy.array(wavelength)



        #calculating the back ground level
        background= numpy.mean(value[-nbg:])
        #substracting background
        value=value-background
        #removing the negatives
        for v in value:
            value = [v if v>0 else 0 for v in value]

        #making a directory to store the results
        bgsubstracted=os.path.join(target, 'Background␣corrected'
           )
        os.makedirs(bgsubstracted,exist_ok=True)

        #save the back ground substracted spectra
        targetfile=os.path.join(bgsubstracted,infile)
        out=numpy.vstack([[wavelength],[value]])
        with open(targetfile, 'w', newline='') as t:
            numpy.savetxt(targetfile, out.T, delimiter="␣")


#averaging per temperature. Edit the calling file lists if
    you have different data.
temperature
    =[25,100,150,200,250,300,350,400,450,500,550,600,650,700,750,

    800,850,900,950,1000,1050,1100,1150,1200,1250,1300,1350,1400,1430]

heat=['T2_1.DAT','T2_2.DAT','T2_3.DAT','T2_4.DAT','T2_5.DAT',
    'T2_6.DAT','T2_7.DAT','T2_8.DAT','T2_9.DAT','T2_10.DAT','
    T2_11.DAT','T2_12.DAT','T2_13.DAT','T2_14.DAT','T2_15.DAT'
    ,'T2_16.DAT','T2_17.DAT','T2_18.DAT','T2_19.DAT','T2_20.
    DAT','T2_21.DAT','T2_22.DAT','T2_23.DAT','T2_24.DAT','
    T2_25.DAT','T2_26.DAT','T2_27.DAT','T2_28.DAT','T2_29.DAT'
    ]
cool=['T2_44.DAT','T2_43.DAT','T2_3.DAT','T2_42.DAT','T2_5.
    DAT','T2_41.DAT','T2_7.DAT','T2_40.DAT','T2_9.DAT','T2_39.
    DAT','T2_11.DAT','T2_38.DAT','T2_13.DAT','T2_37.DAT','
    T2_15.DAT','T2_36.DAT','T2_17.DAT','T2_35.DAT','T2_19.DAT'
    ,'T2_34.DAT','T2_21.DAT','T2_33.DAT','T2_23.DAT','T2_32.
    DAT','T2_25.DAT','T2_31.DAT','T2_27.DAT','T2_30.DAT','
    T2_29.DAT']


#createa folder for the averaged files
averaged=os.path.join(target, 'Averaged')
os.makedirs(averaged,exist_ok=True)

i=0
while i<len(temperature):
    FILE=os.path.join(bgsubstracted, heat[i])
    with open(FILE, newline='') as f:
```

```
            heat_wavelength, heat_value= numpy.loadtxt(FILE,
                unpack=True)

        FILE=os.path.join(bgsubstracted, cool[i])
        with open(FILE, newline='') as f:
            cool_wavelength, cool_value =  numpy.loadtxt(FILE,
                unpack=True)

        #Turn lists into arrays
        heat_value= numpy.array(heat_value)
        heat_wavelength =numpy.array(heat_wavelength)
        cool_wavelength = numpy.array(cool_wavelength)
        cool_value = numpy.array(cool_value)

        #calculate the averages
        average=(heat_value+cool_value)/2

        #save the data
        targetfile=os.path.join(target,'Averaged',str(temperature
            [i])+'.dat')
        out=numpy.vstack([[heat_wavelength],[average]])
        with open(targetfile, 'w', newline='') as t:
            numpy.savetxt(targetfile, out.T, delimiter="␣")

        i=i+1

#calculating the correctionss
corrected=os.path.join(target, 'Corrected')
os.makedirs(corrected,exist_ok=True)
listing = os.listdir(averaged)

for infile in listing:
        #print('Current file is:'+infile)
        with open(FILE, 'r', newline=''):
            FILE=os.path.join(averaged, infile)
                    #Read the first column as the wave length and
                        the second as T(AU)
            wavelength, value = numpy.loadtxt(FILE,unpack=True)
        value=value[180:1057]
        calculate(value, thickness, target, corrected, infile)
```

calculate.py

```
"""function to correct the spectra by dividing by the RT
    spectrum and multiplying with the L19 spectrum"""
import os
import numpy
import math
import operator

def calculate(value, thickness, source, target, name):


        #Get the room temperature and L19(RT) files to correct
            for the lamp spectrum and get an absolute transmission
        #Room temperature file from regular spectrometer
        FILE=os.path.join(source,'l19.txt')
```

```
with open(FILE, newline='') as f:
    L19= numpy.loadtxt(FILE,unpack=True)
L19=L19[180:1057]+10**-6

#Room temperature file from high temperature setup
FILE=FILE=os.path.join(source,'RT.dat')
with open(FILE, newline='') as f:
    wavelength, RT= numpy.loadtxt(FILE,unpack=True) #Read
        the first column as the wave length and the
       second as T/T%/Absorbance
wavelength=wavelength[180:1057]
RT=RT[180:1057]

#converting all values into arrays
wavelength=numpy.array(wavelength)
value=numpy.array(value)
RT=numpy.array(RT)
L19=numpy.array(L19)

#correcting for the lamp spectrum (/RT) and then
   generating absolute Tr's (*L19)

value=value*(L19/RT)

#calculate the energy
energy=1239.491/wavelength

#Calculate the reflectance, R, fitted from literature
   data
i=0
R=numpy.zeros(len(value))

for r in R:
    if  energy[i]<=3.52807796:
        a=0.13605+0.00187*math.exp(energy[i]/0.92488)
        R[i]=a
    else:
        R[i]=0.22055


    i=i+1

Emis=1-value-R
R=list(R)
value=list(value)


#calculate the absorption coefficient alpha and its
   square root
i=0
alpha=list(numpy.zeros(len(value)))
sqrtalpha=list(numpy.zeros(len(value)))

for v in value:
    if value[i] ==0:
        a=0
```

```
        else:
            a=-1*numpy.log((math.sqrt((1-R[i])**4+4*value[i
               ]**2*R[i]**2)-(1-R[i])**2)/(2*value[i]*R[i
               ]**2))/thickness

        alpha[i]=a
        #sqrtalpha[i]=numpy.sqrt(alpha[i])

        i=i+1

    alpha=numpy.array(alpha)
    sqrtalpha=numpy.array(sqrtalpha)
    sqrtalpha=numpy.sqrt(alpha)
    value=numpy.array(value)

    #output the data into a file with the same name
    targetfile=os.path.join(target,name)
    out=numpy.vstack([[wavelength],[energy],[R],[value], [
       alpha],[sqrtalpha],[Emis]])
    with open(targetfile, 'w', newline='') as t:
        numpy.savetxt(targetfile, out.T, delimiter="␣")
```

A.2. Mie scattering

The Mie scattering spectra for the nano-voids in $SrTiO_3$ were calculated using the following script written in GNU Octave. The function performing the basic calculation is `miecalc.m` which is called by, for example, `Mie_dist_por_C2.m`.

`miecalc.m`

```
%Function for Mie coefficient calculations

%Inputs:
%wavelength: vector with the wavelengths of interest
%epsmedium: the complex dieelectric function of the medium,
   vector, same length as wavelength
%epsmetal: the complex dieelectric function of the metal,
   vector, same length as wavelength
%pdiameter: the particle diameter, positive number
%multipole_order: the multipole order, positive integer which
    sets the order to which the calculation should run

function [CSCA, CABS, CEXT] = mie_calc (wavelength, epsmedium
   , epsmetal, pdiameter,multipole_order)
if (length(wavelength)!=length(epsmedium) || length(
   wavelength)!=length(epsmetal))
  error("The input vectors have to be the same length!")
elseif (pdiameter <= 0)
        error("The diameter has to be positive!")
elseif (multipole_order != floor(multipole_order) ||
   multipole_order <= 0)
        error("The multipole oder has to be a positive
           integer!")
endif
```

```
%frontal area of a particle
A=pi*(pdiameter/2)^2;

%size parameter: |wave vector|* sphere radius
kr=2*pi*(sqrt(epsmedium)./wavelength)*(pdiameter/2);

%calculate relative dielectric function:
eps=epsmetal./epsmedium;
m=sqrt(eps);

%create empty vectors to receive output:
CSCA= zeros(1,length(wavelength));
CABS = zeros(1,length(wavelength));
CEXT = zeros(1,length(wavelength));

for n=1:multipole_order

%calculating the ricatti-bessel functions and the derivatives
    :
psi=kr.*sqrt(pi./(2.*kr)).*besselj(n+1/2,kr);
dpsi=diff(psi)./diff(kr);
%this adds the last value of dpsi onto the end since it
    otherwise is 1 element short
dpsi=[dpsi dpsi(length(dpsi))];

psim=m.*kr.*sqrt(pi./(2.*m.*kr)).*besselj(n+1/2,m.*kr);
dpsim=diff(psim)./diff(m.*kr);
dpsim=[dpsim dpsim(length(dpsim))];

xi=kr.*sqrt(pi./(2.*kr)).*besselh(n+1/2,1,kr);
dxi=diff(xi)./diff(kr);
dxi=[dxi dxi(length(dxi))];

xim=m.*kr.*sqrt(pi./(2.*m.*kr)).*besselh(n+1/2,1,m.*kr);
dxim=diff(xim)./diff(m.*kr);
dxim=[dxim dxim(length(dxim))];

%Mie coefficients:
an=(m.*psim.*dpsi-psi.*dpsim)./(m.*psim.*dxi-xi.*dpsim);
bn=(psim.*dpsi-m.*psi.*dpsim)./(psim.*dxi-m.*xi.*dpsim);


%scattering and extinction cross sections:
Csca=A*2*(2*n+1)*(abs(an).^2+abs(bn).^2)./kr.^2;
Cext=A*2*(2*n+1)*real(an+bn)./kr.^2;

Cabs=Cext-Csca;

%add this iteration to totals:
CSCA= CSCA + Csca;
CABS = CABS + Cabs;
CEXT = CEXT + Cext;

endfor
endfunction
```

Mie_dist_por_C2.m

```
%Script to run Mie calculations for voids in SrTiO3. The
    dielectric functions for STO are fitted from the
    literature
%The script uses a size distribution and also returns the
    porosity in percent
clear all
close all
clc

%Set the wavelength range to that of the fit
wavelength=300:1:825;

%Set the other parameters needed
multipole_order=8; %multi pole order, the number of summation
     steps to be taken into account

%loading the STO data
n=load("nSTO.txt");
nSTO=interp1(n(:,1),n(:,2), wavelength,"spline");

k=load("kSTO.txt");
kSTO=interp1(k(:,1),k(:,2), wavelength,"spline");

%Data measured for colorless STO
Verneuil=load('Verneuil_matched1.txt');
Verneuil=interp1(Verneuil(:,1), Verneuil(:,2), wavelength, "
    spline");

%Load the spectrum to compare to
meas= load('C2.txt');

%Void data
nVoid=ones(size(wavelength));
kVoid=zeros(size(wavelength));

%Turn n and k values into complex dielectric functions
epsmedium=(nSTO+j*kSTO).^2;
epsMet=(nVoid+j*kVoid).^2;

%Set the maximum particle size to be considered
size_limit=100;

%Set a lognormal distribution for the particle radius giving
    approximately the distribution found in TEM with a peak
    for 1.3 nm
sizes=1:size_limit;
A=2E16;
s=0.69;
m=0.7;
concentration=A*lognpdf(sizes,m,s);

CscaT=zeros(length(wavelength), 1);
```

```
%Loop through the calculation for eacht size, add it to the
    total scattering and multiply by the concentration
for s=1:size_limit

Csca=zeros(length(wavelength),1);
Cabs=zeros(length(wavelength),1);
Cext=zeros(length(wavelength),1);

[Csca, Cabs, Cext]=mie_calc(wavelength, epsmedium, epsMet, s,
    multipole_order);
CscaT=CscaT+Csca'*1E-14*concentration(s);
end

%Total theoretical spectrum
Ext=CscaT+Verneuil';

%calculate the porosity factor in percent
x=1:size_limit;
porosity=(x/2).^3.*1E-21.*concentration;
porosity_percent=100*sum(porosity)

figure
plot(meas(:,1), meas(:,2), wavelength, CscaT, wavelength, Ext
    )
legend("Measured", "Calculated Scattering", "Scat+Verneuil")
axis([390, 800, -2, 15]);
title(num2str(size_limit))

figure
semilogy(x, concentration)
axis([1,50, 1E10,1E17])
```

Publications

- Guguschev, C., Kok, D.J., Juda, U., Uecker, R., Sintonen, S., Galazka, Z., Kwasniewski, A. & Bickermann, M. (2016). Top-seeded solution growth of $SrTiO_3$ single crystals virtually free of mosaicity. *J. Cryst. Growth,* ICCGE-18 special volume, under review.

- Kamutzki, F., Guguschev, C., Kok, D. J., Bertram, R., Juda, U. & Uecker, R. (2016). The influence of oxygen partial pressure in the growth atmosphere on the coloration of $SrTiO_3$ single crystal fibers. *CrystEngComm*, 18, 5658-5666.

- Kok, D. J., Guguschev, C., Markurt, T., Niu, M., Bertram, R., Albrecht, M., & Irmscher, K. (2016). Origin of brown coloration in top-seeded solution grown $SrTiO_3$ crystals. *CrystEngComm*, 18, 4580-4586.

- Guguschev, C., Galazka, Z., Kok, D. J., Juda, U., Kwasniewski, A. & Uecker, R. (2015). Growth of $SrTiO_3$ bulk single crystals using edge-defined film-fed growth and the Czochralski methods. *CrystEngComm,* 17(25), 4662-4668.

- Kok, D. J., Irmscher, K., Naumann, M., Guguschev, C., Galazka, Z. & Uecker, R. (2015). Temperature-dependent optical absorption of $SrTiO_3$. *Phys. Status Solidi A*, 212(9), 1880-1887.

- Guguschev, C., Kok, D. J., Galazka, Z., Klimm, D., Uecker, R., Bertram, R., Naumann, M., Juda, M., Kwasniewski, A. & Bickermann, M. (2015). Influence of oxygen partial pressure on $SrTiO_3$ bulk crystal growth from non-stoichiometric melts. *CrystEngComm*, 17(17), 3224-3234.

- Guguschev, C., Klimm, D., Langhans, F., Galazka, Z., Kok, D.J., Juda, U., & Uecker, R. (2014). Top-seeded solution growth of $SrTiO_3$ crystals and phase diagram studies in the SrO–TiO_2 system. *CrystEngComm*, 16(9), 1735-1740.

Selbständigkeitserklärung

Ich erkläre, dass ich die Dissertation selbständig und nur unter Verwendung der von mir gemäß § 7 Abs. 3 der Promotionsordnung der Mathematisch-Naturwissenschaftlichen Fakultät, veröffentlicht im Amtlichen Mitteilungsblatt der Humboldt-Universität zu Berlin Nr. 126/2014 am 18.11.2014 angegebenen Hilfsmittel angefertigt habe.

Berlin, den

Dirk Johannes Kok